

Mössbauer-Effect Investigation Of (i) Antipathetic
Relation Between Garnet And Clinopyroxene In Terms
Of Iron Content And (ii) Fe³⁺-Doped Single Crystal
Of Guanidinium Aluminum Sulfate Hexahydrate

Mehran Sabbaghian

A Thesis
in
The Department
of
Physics

Presented in Partial Fulfillment of the Requirements
for the Degree of Master of Science at
Concordia University
Montréal, Québec, Canada

March 1985

© Mehran-Sabbaghian, 1985.

ABSTRACT

Mössbauer-Effect Investigation of (i) Antipathetic Relation Between Garnet And Clinopyroxene In Terms of Iron Content And (ii) Fe³⁺-Doped Single Crystal of Guanidinium Aluminum Sulfate Hexahydrate

Mehran Sabbaghian

(i) Garnets and Pyroxenes in the Skarns of the Sullipek Copper deposit, Gaspé North, Québec, show relationships in colour between them such that the darker is the colour of the garnet the lighter is the colour of the associated pyroxene and vice versa. It has been suggested that this relationship may reflect an antipathetic relation in the iron contents of these two minerals. In order to test this hypothesis, the Fe²⁺ and Fe³⁺ contents of the minerals were determined from their Mössbauer spectra. The spectra were computer-fitted to Lorentzian line shapes, and the various peaks were assigned to iron in Fe²⁺ and Fe³⁺ states. A plot of the area of Fe³⁺ peaks in garnet versus that of the Fe²⁺ peaks in pyroxene shows a considerable scatter, but outlines a trend coarsely consistent with the antipathetic relationship. However, a correlation between the colour of the minerals and their iron content was not always confirmed, the darker colour does not necessarily indicate a higher iron content. Presence of impurities such as Ti⁴⁺ and Mn²⁺, and charge-transfer phenomenon may also be contributory factors.

(ii) The spectra of Fe^{3+} in GASH (Guanidinium Aluminum Sulfate Hexahydrate) were obtained at room temperature in the 2 mm/sec velocity range. Rigorous computer-fitting of the data to two and four (1 and 2 doublets) peaks were carried out and the realistic result was chosen. The components were then derived and assigned to Fe^{3+} in octahedral position. The quadrupole coupling constant e^2qQ/h of Fe^{3+} in GASH (for the first excited state) was calculated. Further, the ratios of $|(A-B)/A|$ (as found by ENDOR measurements) to e^2qQ/h in GASH were estimated to be 0.0028 and 0.0034 for the sites I and II, respectively. These values are consistent with those found for the hosts rutile (TiO_2) and octaethylhemine. This supports the analysis of Schlaak²⁸ predicting a linear dependence of crystalline field amplitude $A_2^0 (= |(A-B)/A|)$ on quadrupole coupling constant (e^2qQ/h).

ACKNOWLEDGEMENTS

The author is indebted to Prof. S.K.Misra and to Dr.S.Kumarapell for proposing these studies and for their continued interest, help and advice. He also wishes to express deep gratitude to Dr. N.Eddy for his assistance during the whole experimental work. Grateful acknowledgement is due to E.Eladas, B.Landry and J.Scodnick for their help during the early stages of this work. The author also appreciates the supply of samples and many helpful discussions received from R. Wares.

TABLE OF CONTENTS

		<u>PAGES</u>
	ABSTRACT	iii
	ACKNOWLEDGEMENTS	v
	LIST OF TABLES	viii
	LIST OF FIGURES	ix
CHAPTER I	INTRODUCTION	1
CHAPTER II	THEORY	4
2.1	"RECOIL-FREE" GAMMA-RAY RESONANCE	4
2.2	HYPERFINE STRUCTURE	7
2.2a	ISOMER SHIFT	8
2.2b	QUADRUPOLE SPLITTING	13
2.2c	MAGNETIC SPLITTING	18
CHAPTER III	EXPERIMENTAL TECHNIQUE	21
3.1	METHOD	21
3.2	SOURCE	23
3.3	DRIVE SYSTEM	25
3.4	DETECTOR	26
3.5	AMPLIFICATION SYSTEM	26
3.6	MULTI-CHANNEL ANALYZER	28
3.7	CALIBRATION	29
3.8	DATA TRANSFER	32
CHAPTER IV	ANALYSIS OF SPECTRA	33
4.1	COMPUTATIONAL METHOD	33
4.2	LINE WIDTH, SHAPE, AREA	34
CHAPTER V	MÖSS. SPECTROSCOPY IN MINERALOGY	38
5.1	INTRODUCTION	38

	PAGES
5.2 PYROXENES	41
5.3 GARNETS	46
CHAPTER VI THE SULLIPEK SKARNS	50
6.1 INRODUCTION	50
6.2 GEOLOGICAL SETTING	50
CHAPTER VII SAMPLES AND ABSORBER PREPARATION	55
7.1 ABSORBER PREPARATION	56
CHAPTER VIII RESULTS AND INTERPRETATIONS	59
8.1 COLOUR DEPENDENCE TO THE IRON CONTENT.	93
8.2 CONTRIBUTARY FACTORS TO THE COLOURING.....	96
8.3 SUMMARY AND CONCLUSIONS.....	97
CHAPTER IX Fe ³⁺ IN GASH	99
CHAPTER X CONCLUSION	106
APPENDIX A Programme MOSSBR	110
APPENDIX B MICOM- Programmes	125
APPENDIX C Description of samples	129
APPENDIX D Isomer Shift Scale	130
List of References	108

LIST OF TABLES

	<u>PAGES</u>
1. Components Of EFG Tensor	16
2. Isomer Shift Scales	24
3. Compositions Of Pyroxene Minerals	42
4. Compositions of Garnet Minerals	47
5. Location Of Samples	55
6. Alphabetical Labels of Samples	57
7. Calculated Parameters, And Initial % Of Pyroxene and Garnet in mixed absorbers	88
8. Numerical designations of iron content	89
9. Colour of samples	95

LIST OF FIGURES

	<u>PAGES</u>
1. Emission of gamma rays from a free atom	5
2. Nuclear energy levels and Isomer Shift	10
3. Nuclear energy levels and Quadrupole Splitting	14
4. Magnetic Splitting in ^{57}Fe ; (a) Energy level diagram, (b) The resultant Mössbauer spectrum	19
5. Block diagram of the Mössbauer experiment	22
6. Decay Scheme of ^{57}Co .	24
7. Drive velocity wave form, the corresponding channel advance and an absorption spectrum	27
8. The spectra of an Iron foil, obtained at 10mm/sec	30
9. The spectra of an Iron foil, obtained at 4mm/sec	31
10. ^{57}Fe Centre shifts and Quadrupole splitting variations versus coordination number	39
11. Composition of important pyroxenes in the system Diopside-Enstatite-Hedenbergite-Ferrosilite	42
12. Idealized illustration of a single pyroxene chain	44
13. Idealized crystal structure of diopside	44
14. Crystal structure of garnet	48
15. Geographical location of the Sullipék deposit	51
16. Horizontal cross-section of the Sullipék deposit	54
17. Möss. spectra of sample S24-793 garnet/clinopyroxene	60
18. Möss. spectra of sample S24-793 garnet	61
19. Möss. spectra of sample S24-558 garnet/clinopyroxene	62
20. Möss. spectra of sample S24-558 garnet	63
21. Möss. spectra of sample S42-520 garnet/clinopyroxene	64
22. Möss. spectra of sample S42-520 garnet	65

	<u>PAGES</u>
23. Möss. spectra of sample S42-534 garnet/clinopyroxene	66
24. Möss. spectra of sample S42-534 garnet	67
25. Möss. spectra of sample P31-455 garnet/clinopyroxene	68
26. Möss. spectra of sample P31-455 garnet	69
27. Möss. spectra of sample P72-254 garnet/clinopyroxene	70
28. Möss. spectra of sample P72-254 garnet	71
29. Möss. spectra of sample S38-251 garnet/clinopyroxene	72
30. Möss. spectra of sample S38-251 garnet	73
31. Möss. spectra of sample SH-14 garnet/clinopyroxene	74
32. Möss. spectra of sample SH-14 garnet	75
33. Möss. spectra of sample S104-200 garnet/clinopyroxene	76
34. Möss. spectra of sample S104-200 garnet	77
35. Möss. spectra of sample T-16 garnet/clinopyroxene	78
36. Möss. spectra of sample T-16 garnet	79
37. Möss. spectra of sample T-24 garnet/clinopyroxene	80
38. Möss. spectra of sample T-24 garnet	81
39. Möss. spectra of sample T-45 garnet/clinopyroxene	82
40. Möss. spectra of sample T-45 garnet	83
41. Möss. spectra of sample T-50 garnet/clinopyroxene	84
42. Möss. spectra of sample T-50 garnet	85
43. Möss. spectra of sample T-62 garnet/clinopyroxene	86
44. Möss. spectra of sample T-62 garnet	87
45. Numerical designations of Iron content of Fe ³⁺ and Fe ²⁺ , plotted versus each other	90
46. Dimensions of the color solid	96
47. Crystal growing habit of GASH	101

48. Schematic of a unit cell of GASH

PAGES
102

49. Mössbauer Spectra of GASH

103

CHAPTER I

INTRODUCTION

The Mössbauer effect, known as recoil-free nuclear resonance was discovered in 1958 by the German physicist R.L.Mössbauer. Mössbauer effect began to be widely applied to chemical problems, after it was shown (1960) that ^{57}Fe exhibited this resonant phenomenon. The aims in the early period were primarily directed towards the properties of the nuclear states (low energy nuclear physics). General interest in its applications to mineralogy, geology and crystallography developed a few years later, where attention was focussed on ^{57}Fe resonance in minerals.

Investigation on the Skarn-related Cu-Mo mineralization at the Sullipék deposit, Gaspé north, Québec, have suggested that the skarns are zoned with garnet/clinopyroxene and the pyroxene and garnet vary antipathetically in Fe content. The idea was merely based on colour variation of the garnet and pyroxene with respect to one another, such that the lighter the pyroxene, the darker is the associated garnet and vice versa. Darker colour was assumed to correspond to samples with more iron content, and lighter colour to the samples with less iron content. The main objective behind this work is to investigate the proposed "antipathetic relation", and its correlation to the colour of the minerals, quantitatively. This is done in

two steps:

A- To investigate the existence of the antipathetic relation, quantitatively, by using the area method in Mössbauer technique, regardless of the colour of minerals.

B- To investigate the colour dependence on the iron content and its correlation to the antipathetic relation. The investigation was carried out on the Sullipék deposit, Gaspé, Québec, by studying samples selected from drill cores and from tailing piles (Fig.16, table 5).

Investigations on the crystal structure of GASH (Guanidinium Aluminum Sulfate Hexahydrate) has shown that, two of the three Al^{3+} (Fe^{3+}) ions per unit cell of this crystal are equivalent to each other and belong to site II, whereas the other belongs to site I. In Mössbauer spectra this is equivalent to having two doublets, one corresponding to Fe^{3+} in site II and the other to Fe^{3+} in site I.

Present investigation on GASH is carried out in order to measure the quadrupole coupling constant e^2qQ/\hbar for the sites I and II. One can use these measurements to examine the linear relationship between quadrupole coupling constant and the axial crystaline field amplitude $A_2^0 = |(A-B) / A|$, as derived by Schlaak²⁸ in context with Mn^{2+} -doped crystals.

The theory of the Mössbauer effect, the experimental technique, calibration, and data transfer procedure and the

computational method are described in chapters 2, 3 and 4 respectively. This is followed by the application of the Mössbauer spectroscopy to geology and mineralogy in chapter 5. A brief presentation of the crystal structure of garnets and pyroxenes is given in chapter 5. Geology of the Sullipek skarns, and description of the samples and absorbers are presented in chapters 7 and 8 respectively. The various spectra obtained, are illustrated in chapter 8, along with the calculated results, and interpretations in terms of the main objectives.

The details of the crystal structure of GASH (Guanidinium Aluminium Sulfate Hexahydrate) and the analysis of its Mössbauer spectra are discussed in chapter 9. The results are used to examine if the quadropole moment e^2Qq/h of Fe^{3+} is consistent with the relationship to the value $|(A-B) / A|$ in GASH. Concluding remarks are made in chapter 10.

CHAPTER II

THEORY

A convenient starting point for a discussion of the theory of the Mössbauer effect is the concept of resonance absorption. We speak of resonance absorption if a system absorbs a quantum of energy equal to the difference between two of its energy states. Resonance absorption has long been known in connection with electronic transitions. As the energy states of the atomic nucleus are similarly quantized discrete values, it was to be expected that, if the ground state isobar of a gamma radiating radio active source decomposing by isomer transition is used as an absorbent, it will absorb the gamma-radiation with a large cross-section.

2.1.

"RECOIL-FREE" Gamma Ray Resonance: (emission and absorption)

Before 1958, it was realized that the process of resonance absorption would be hindered by the "recoil energy loss". This recoil energy loss follows from the conservation of momentum. The gamma ray emitted by the nucleus has a certain momentum approximately $P=E_0/C$, and to conserve the original momentum of the system, the nucleus emitting the ray must acquire E_0/C in the opposite direction. However, this implies that a kinetic energy $P^2/2M = E_0^2/2MC$ (M is the mass of the recoiling nucleus) has been given to the nucleus (see Fig.1.). This energy came

from the original excitation energy of the nucleus, E_0 . From the conservation of energy, therefore, the gamma ray does not have the full transition energy E_0 , but (approximately) $E_0 - E_0^2/2MC^2$.

Initial state:

nucleus with energy E_0 and momentum 0

After emission:

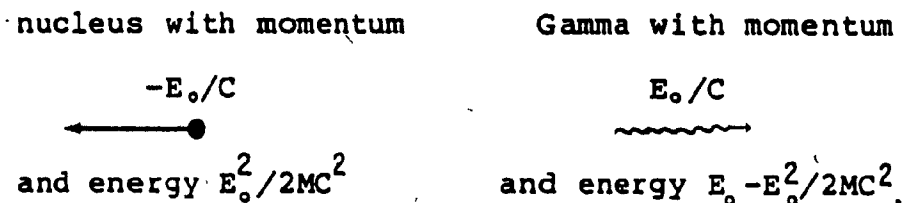


Fig.1. Emission of gamma rays from a free atom.

This recoil energy loss is very small, typically only about a millionth of E_0 , but the nuclear resonance is so sharply tuned that it can be destroyed by a change of the source frequency of only one part in ten billion. Thus, it was not expected to observe the resonance absorption, since the energy lost to recoil was some 100.000 times the resonance width. Mössbauer had the insight to realize that the simple "isolated atom" picture might not be valid in a solid, and was able to show that when the bonds between atoms were considered, a quantum mechanical analysis of the process led to a different result.

A realistic analysis, considering the character of the forces between the atoms in the solid, shows that the crystal vibration energies, like atomic energy levels, are quantized. Thus only certain amounts of energy can be given to the crystal lattice, i.e., it can accept 0,1,2,... quanta of vibrational energy called "Phonons", but not a fraction of a phonon. If we choose a situation in which the free-atom recoil energy is much smaller than the energy required to give one phonon to the lattice, most of the gamma ray emissions will be "no-phonon" processes, i.e., no phonons, and therefore no energy, will be given to the lattice, and gamma ray will have the full energy corresponding to the nuclear resonance.

The percentage of no-phonon gamma-ray emissions, known as the "recoil-free fraction", can be almost 100% for some isotopes, but is usually much less. It decreases very rapidly as E_0 increases, since the free-atom recoil energy becomes comparable to energies that can be given to the lattice.

Recoil energy loss in emission has as a counterpart recoil energy loss in absorption. The nucleus absorbing the gamma ray must acquire some kinetic energy. To be resonantly absorbed by a freely recoiling nucleus the gamma ray must have the transition energy E_0 plus the recoil energy. However, no-phonon processes as outlined above also occur

in absorption, thus the gamma rays can be both emitted and absorbed in no phonon events. This process of "recoil-free" gamma ray resonance emission and absorption is the heart of the Mössbauer effect.

The percentage of no-phonon gamma ray emission, known as the "Recoil-Free Fraction" or "Mössbauer Fraction" is given by equation (1):

$$f = \text{Exp}[-4\pi^2 \langle \chi^2 \rangle / \lambda^2] \quad (1)$$

where λ is the wavelength of the gamma quanta and $\langle \chi^2 \rangle$ is the component of the mean square vibrational amplitude of the emitting nucleus in the direction of the gamma ray.

2.2. HYPERFINE STRUCTURE OF MÖSSBAUER SPECTRA

As the half widths of the lines of Mössbauer spectra are fairly small (e.g., 4.9×10^{-9} ev for iron), the probability of the effect (absorption) is very sensitive to even quite small energy changes. Such small changes occur about in the energy state of the nucleus as a result of interaction with the external environment (the electron shell and the other atoms of the crystal). For this reason, if the source and the absorbent do not have identical compositions, the energy states of the atomic nuclei are also different and the possibility of resonance absorption does not exist. If the source is moved at various rates, however, the resonance state can be created with the aid of the Doppler energy and, with knowledge of the rate of movement, conclusions can be

drawn about the energy differences, i.e., on the effect of the environment.

The peak positions in a Mössbauer spectrum are sensitive to the extranuclear environment, such that different compounds give different spectra. The differences in spectra can be attributed to the so called Hyperfine Interactions, the interactions between the nuclear charge distribution and the extranuclear electric and magnetic fields. These hyperfine interactions give rise to the Isomer Shift (I.S), the Quadrupole Splitting (Q.S) and the magnetic Zeeman splitting.

In the case of minerals, we are concerned mainly with the first two parameters, and how they can be related to the electronic and ligand structure of minerals.

In addition, other spectral parameters such as peak shapes, width, and areas are of special importance for the detailed interpretation of the mineral spectra.

2.2(a). THE ISOMER SHIFT

The isomer shift arises from the coulombic interaction of the nuclear charge and the electron charge. The most effective part of this interaction is the result of the electron charge density at the nucleus (S electrons). The above interaction does not lead to a splitting of the nuclear energy levels, but rather results in a slight shift

of the Mössbauer energy levels in a compound relative to those in the free atom. The shift will in general be different in source and absorber (Fig. 2a.), and thus the energy of the source gamma ray ${}^sE_\gamma$, and the energy required for resonant absorption, ${}^aE_\gamma$, will be different by $\sim 10^{-9}$ ev. A Doppler velocity will have to be supplied to the source or absorber to observe resonance: ${}^sE_\gamma \pm (v/c) {}^sE_\gamma = {}^aE_\gamma$. In this case one line spectrum of the type shown in Fig. 2b. results.

It is important to realize that such a shift of energy levels can also arise from the second order Doppler (S.O.D) shift, also known as "temperature shift" which arises from the thermal motion of the Mössbauer atoms. The centre or chemical shift (C.S) observed in a Mössbauer spectrum is a resultant of both the isomer shift and second order Doppler shift, but the second order Doppler shift is usually much smaller than the isomer shift, and the variations in the second order Doppler shift from compound to compound are very small. The isomer shift can be computed classically by considering the effect of the overlap of s-electron density with the nuclear charge density. Only s electrons of the hydrogen like orbitals have a finite probability of overlapping with the nuclear charge density, and thus of interacting with it, however, the s-electron density at the nucleus is often sensitive to the p or d electron density.

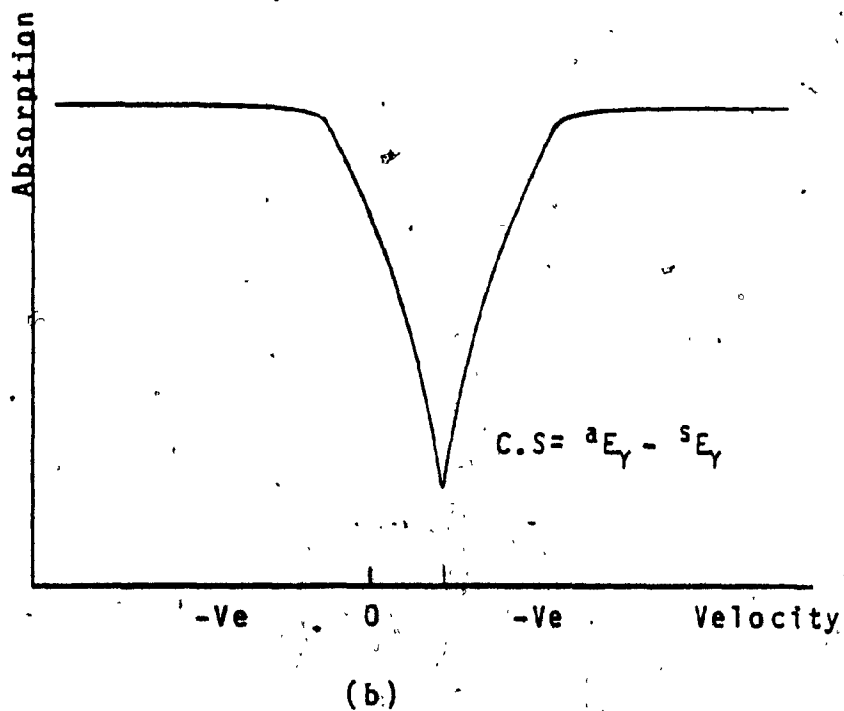
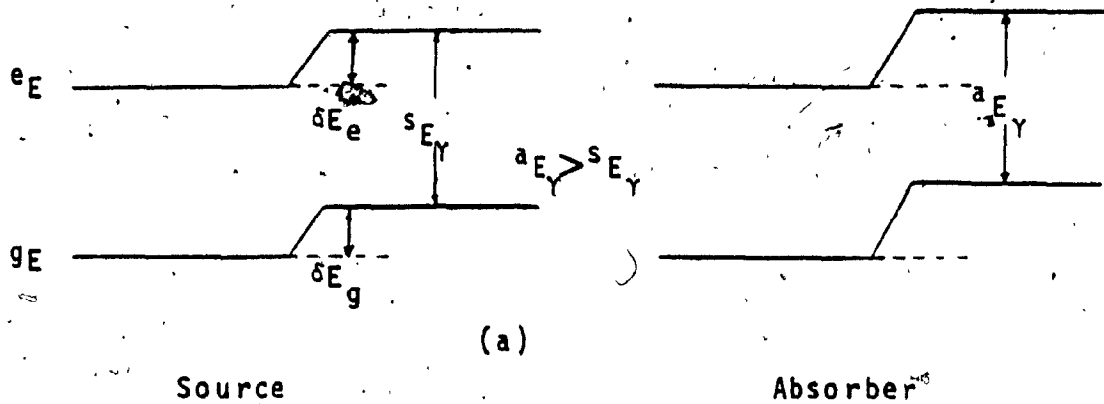


Fig.2. Nuclear energy levels and the isomer shift.

(a) Source and absorber nuclear energy levels.

(b) Resultant Mössbauer spectrum.

The nucleus is assumed to be a uniformly charged sphere of radius R , and that the charge Ze within it is distributed homogeneously. At a distance r from the centre of the atomic nucleus, the electrostatic potentials is given by:³

$$V = \frac{Ze}{R} \left(\frac{3}{2} - \frac{r^2}{2R^2} \right) \quad \text{where } r < R \quad (2a)$$

$$V = \frac{Ze}{r} \quad \text{where } r > R \quad (2b)$$

As mentioned above, the S electrons with subordinate quantum number $L=0$ have a finite density within the atomic nucleus, the energy states of the nuclide is affected by the charge originating from the electrons in the sphere of radius R . On this basis, the energy shift can be given as:³

$$\delta E = \int_0^R \rho (V' - V) 4r^2 \pi dr = \frac{4\pi \rho Ze}{R} \int_0^R \left(\frac{3}{2} \frac{r^2}{2R^2} - \frac{R}{r} \right) r^2 dr \quad (3)$$

or as:

$$\delta E = -\frac{2\pi}{5} Z e \rho R^2 = \frac{2\pi}{5} Z e^2 |\psi(0)|^2 R^2 \quad (4)$$

where $\rho = -e |\psi(0)|^2$ is the charge density originating from the S electrons in the atomic nucleus.

The atomic nuclei have different radii in the excited and ground states ($R_e \neq R_g$), and therefore δE will also have different values in these states.

$$\delta E_e - \delta E_g = \frac{2\pi}{5} Z e^2 |\psi(0)|^2 (R_e^2 - R_g^2) \quad (5)$$

The Mössbauer atoms in the radiation source and in the absorbent may have different chemical environments (types of chemical bands, oxidation states, etc.), from which it follows that $|\psi_a(0)|^2 \neq |\psi_s(0)|^2$. Hence, the E_0 values

relating to emission and absorption also differ. E_0 is the isomer shift, symbolized by δ :

$$\delta = \frac{2\pi}{5} Z e^2 (R_e^2 - R_g^2) \{ |\psi_s(0)|^2 - |\psi_g(0)|^2 \} \quad (6)$$

Now, taking $\Delta R = R_e - R_g$, $R_e^2 - R_g^2 = 2R \cdot \Delta R = 2R^2 \frac{\Delta R}{R}$, where

$R = (R_e + R_g)/2$, δ can be written as:

$$\delta = \frac{4\pi}{5} Z e^2 R^2 \frac{\Delta R}{R} \{ |\psi_s(0)|^2 - |\psi_g(0)|^2 \} \quad (7)$$

Thus the isomer shift depends on a nuclear factor ΔR and an extranuclear factor $|\psi(0)|^2$. For a given nucleus, ΔR is a constant, so that the isomer shift is directly proportional to the S electron density at the nucleus. When ΔR is positive (as for ^{119}Sn), an increase in S electron density at the absorber nucleus results in a more positive isomer shift, when ΔR is negative (as for ^{57}Fe), an increase in S electron density at the absorber nucleus results in a more negative isomer shift. The density of the S electrons at the position of the nucleus can be estimated from the Fermi-Segre equation:³

$$|\psi_s(0)|^2 = \frac{Z \cdot Z_{\text{eff}}^2}{\pi a_0^3 n_{\text{eff}}^3} \left(1 - \frac{d\sigma}{dn} \right) \quad (8)$$

where Z is the nuclear charge, Z_{eff} is the effective nuclear charge, taking into account the shielding effect of the electrons, a_0 is the Bohr radius of the ground-state atom, n is the real and n_{eff} the effective principal quantum number, and $\sigma = n - n_{\text{eff}}$ is the quantum deficiency.

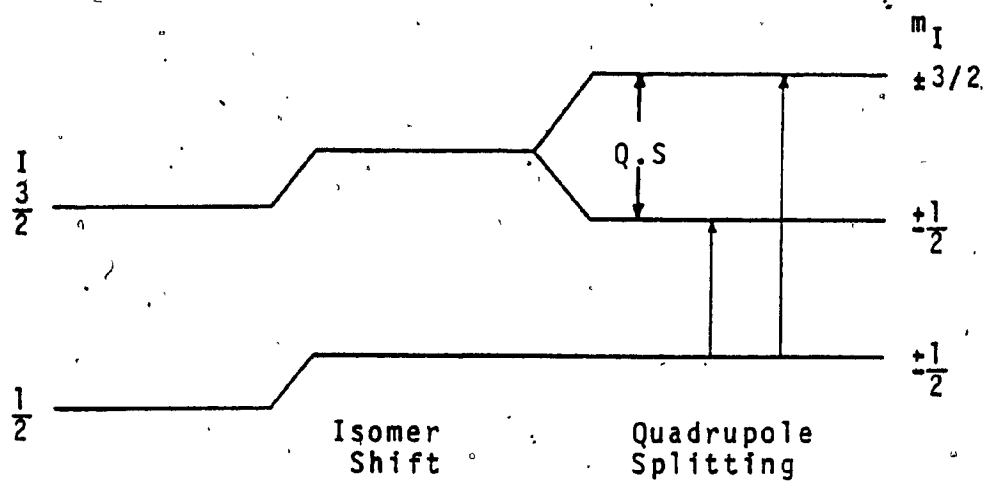
Another expression has been derived for isomer shift by eliminating the approximations made above, using a multiple expansion for the coulomb interaction between the electronic

and nuclear charges. (Shenoy and Wagner, 478)

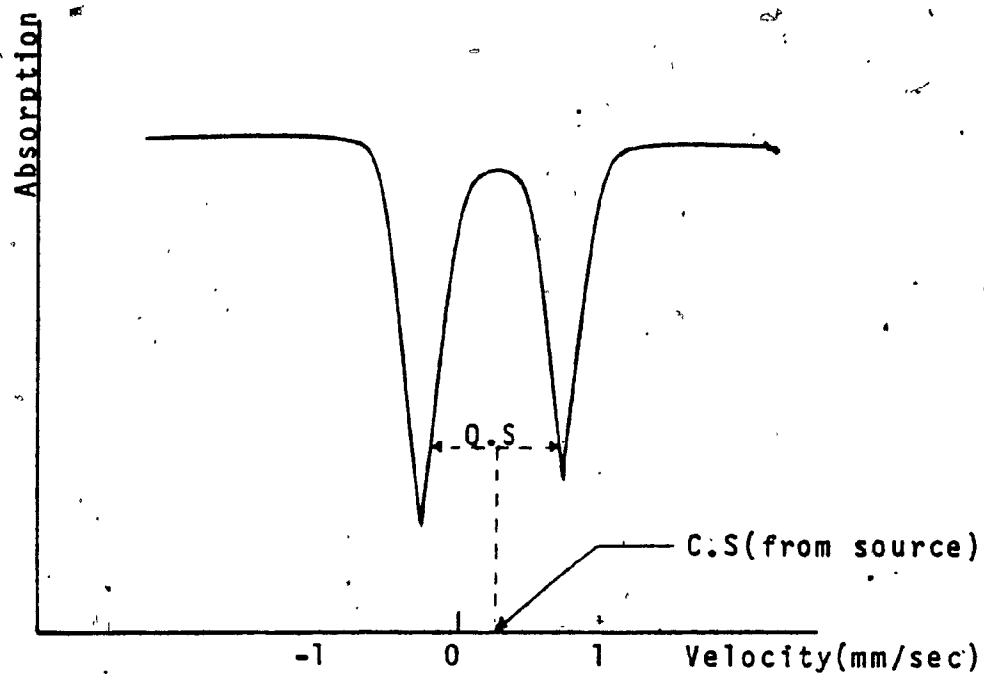
2.2(b). QUADRUPOLE SPLITTING

To derive the expression for isomer shift, it was assumed that the nucleus is a uniformly charged sphere. If these conditions are relaxed, and if $I > 1/2$, the nuclear charge density interacts with the electric field gradient which is caused by the charge distributed asymmetrically around the atomic nucleus (electrons, ions and dipoles). This interaction results in a splitting of the nuclear energy levels. For example, for ^{57}Fe and ^{119}Sn , $I_e = 3/2$ and $I_g = 1/2$, and the $I = 3/2$ level split into two ($m_I = \pm 3/2, \pm 1/2$) while the $I = 1/2$ levels remain degenerate (Fig. 3a.). Both the possible transitions are allowed, and a characteristic two line spectrum is obtained (Fig. 3b.). The separation of the peaks is the quadrupole splitting (Q.S) and the centroid of the two peaks relative to the source is the centre shift (C.S).

Nuclei whose spin is 0 or $1/2$ are spherically symmetric and have a zero quadrupole moment, thus the ground state of ^{57}Fe , with $I = 1/2$, can not exhibit quadrupole splitting. The field gradient is obtained by applying the gradient operator to the three components of the electric field, which is itself a vector. The field gradient is consequently a 3×3 tensor called electric field gradient (EFG) tensor. This tensor has nine components which rise in the following way.



(a)



(b)

Fig.3. Nuclear energy levels and quadrupole splitting.

(a) Absorber energy levels.

(b) Resultant Mössbauer spectrum.

The electric field at the Mössbauer nucleus is the negative gradient of the potential, V :

$$\vec{E} = -\vec{\nabla}V = -(\hat{i}V_x + \hat{j}V_y + \hat{k}V_z) \quad (9)$$

where:

$$V_x = \frac{\partial V}{\partial x}, \quad V_y = \frac{\partial V}{\partial y}, \quad V_z = \frac{\partial V}{\partial z} \quad (10)$$

The EFG tensor is the gradient of the electric field:

$$\text{EFG} = \nabla\vec{E} = - \begin{vmatrix} V_{xx} & V_{xy} & V_{xz} \\ V_{yx} & V_{yy} & V_{yz} \\ V_{zx} & V_{zy} & V_{zz} \end{vmatrix} \quad (11)$$

which can, however, be reduced to diagonal form in the proper coordinate system so that it can be completely specified by three components d^2V/dx^2 , d^2V/dy^2 , d^2V/dz^2 (generally abbreviated V_{xx} , V_{yy} , V_{zz}). These three components are not independent, however, since they must obey the Laplace equation in a region where the charge density vanishes:

$$V_{xx} + V_{yy} + V_{zz} = 0 \quad (12)$$

As a result, there remain only two independent components, usually chosen as V_{zz} , often denoted eq , and η , the asymmetry parameter, defined by:

$$\eta = \frac{V_{xx} - V_{yy}}{V_{zz}} \quad (13)$$

The components are usually chosen so that $|V_{zz}| \geq |V_{yy}| \geq |V_{xx}|$, which constrains η to have values between 0 and 1.

If we assume that the EFG is set up by point charges Z_i , the contribution of one point charge to each component

of the EFG tensor is given by the expressions in table.1.

Table 1. Components of the EFG Tensor.

$V_{xx} = Z e r^{-3} (3 \sin^2 \theta \cos^2 \phi - 1)$	$V_{xy} = V_{yx} = Z e r^{-3} (3 \sin^2 \theta \sin \phi \cos \phi)$
$V_{yy} = Z e r^{-3} (3 \sin^2 \theta \sin^2 \phi - 1)$	$V_{xz} = V_{zx} = Z e r^{-3} (3 \sin \theta \cos \theta \cos \phi)$
$V_{zz} = Z e r^{-3} (3 \cos^2 \theta - 1)$	$V_{yz} = V_{zy} = Z e r^{-3} (3 \sin \theta \cos \theta \sin \phi)$

The interaction between the nuclear electric quadrupole moment Q , and the electric field gradient can be described by the Hamiltonian:³

$$H = \frac{e^2 q Q}{4I(2I-1)} [3I_z^2 - I(I+1) + \frac{\eta}{2} (I_+^2 + I_-^2)] \quad (14)$$

This Hamiltonian has the eigenvalues:

$$E_Q = \frac{e^2 q Q}{4I(2I-1)} [3m_I^2 - I(I+1)] (1 + \frac{\eta^2}{3})^{1/2}; m_I = I, I-1, \dots, -I \quad (15)$$

The magnitude of the quadrupole splitting is proportional to the z component of the electric field gradient (EFG) tensor which interacts with the quadrupole moment of the nucleus,⁷ and is illustrated in the above expression for Hamiltonian.

For the $I=3/2$ case, using the expression for E_Q , the quadrupole splitting can be expressed as:

$$Q \cdot S_o = 1/2 e^2 q Q (1 + \frac{\eta^2}{3})^{1/2} \quad (16)$$

$eq = V_{zz}$ is the Z component of the EFG.

Ideally, we would like to obtain three pieces of information from a measurement of the quadrupole splitting: the magnitude of q and η , and the sign of the quadrupole splitting. If the $+3/2$ state is at high energy, the sign of the quadrupole splitting is positive. For Mössbauer nuclei such as ^{57}Fe and ^{119}Sn having spins $1/2$ and $3/2$, a two line spectrum is observed and the quadrupole splitting is easily measured. But, by the nature of equation 16, it is obvious that both q and η can not be calculated from a measurement of the quadrupole splitting. Also, the sign of the quadrupole splitting can not be determined generally from a powder spectrum since the $+3/2$ and $+1/2$ lines are very similar intensity and can not be distinguished. For more information about the techniques for measuring the sign of Q.S and estimating η , see Bancroft.¹

The EFG tensor components were discussed just considering point charge contributions. However if the electronic configuration has a symmetry lower than cubic, also contribute to EFG tensor. Usually it serves to amplify the EFG due to the distant charges, a phenomenon which carries the name Antishielding. With regard to this, it is convenient to divide the field gradient into two contributions:¹

$$q = (1 - \alpha)q_{\text{lattice}} + (1 - R)q_{\text{valence}} \quad (17)$$

where η assumed to be zero, R and α are the Sternheimer antishielding factors, and q_{lattice} is the contribution from external ligand charges, whereas q_{valence} is the contribution from the valence electrons.

2.2(c). MAGNETIC SPLITTING

The interaction of the magnetic moment of the nucleus with local or applied magnetic fields at the nucleus, results in a degeneracy of the nuclear energy levels. The Hamiltonian of the interaction is:³

$$H_m = -\vec{\mu} \cdot \vec{H} = -g\mu_n \vec{I} \cdot \vec{H} \quad (18)$$

Where g is the gyromagnetic factor and μ_n is the nuclear magneton. The energy levels which are obtained are

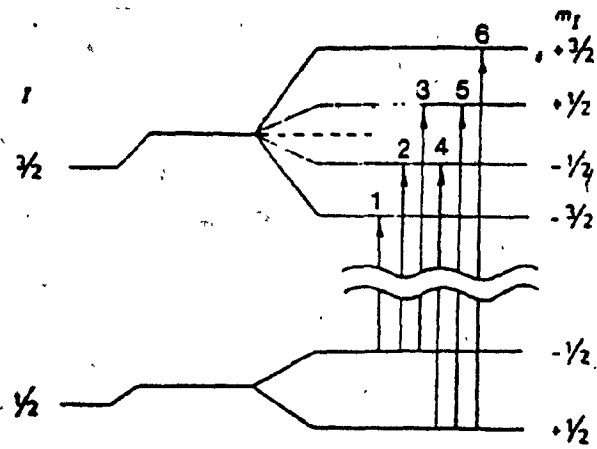
$$E_m = -\mu_n H m_I / I = -g\mu_n H m_I ;$$

$$m_I = I, I-1, \dots, -I \quad (19)$$

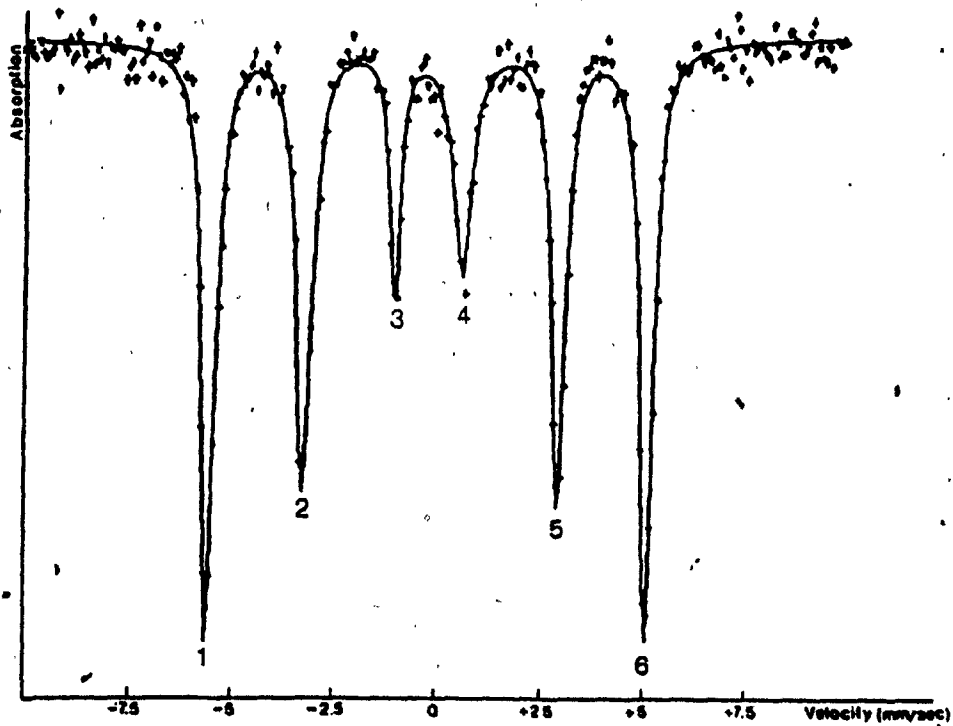
For ^{57}Fe , the g values of ground and excited states have different signs, and the selection rules $\Delta I = 1; \Delta M = 0, +1$ give rise to a symmetric six-line spectrum (Fig. 4b.). The centre shift is given by the centre of gravity of the six peaks.

The line widths of the six peaks are in general equal, but the intensities are very different. The intensities are given by:¹

$$I_1 = I_6 = 3(1 + \cos^2 \theta) \quad (20.a)$$



(a)



(b)

Fig.4. Magnetic splitting in ^{57}Fe . (a) Energy level diagram; (b) The resultant Mössbauer spectrum.

$$I_2 = I_5 = 4\sin^2\theta \quad (20.b)$$

$$I_3 = I_4 = 1 + \cos^2\theta \quad (20.c)$$

Where θ is the angle between the effective $\{H$ and the direction of propagation of the radiation.

CHAPTER III
EXPERIMENTAL TECHNIQUE

3.1. METHOD

The radiation source is attached on a transducer driven by a velocity drive (Fig.5). This motion applies a Doppler velocity V to the source and shifts the energy of the gamma ray emitted from the source by a value ΔE , such that the nuclear transitions in source and absorber can be accurately matched and resonance occurs. The absorber is placed in between the source and the detector. The gamma rays which are transmitted through the absorber are transformed into pulses proportional to their energies by a detector and an amplification system which consists of a pre-amplifier and a amplifier. The pulses which have been produced by the 14.4 Kev gamma rays are selected by the single channel analyzer and fed into the 512 Multi-Channel analyzer (MCA). A time-base generator opens one channel after the other with constant intervals of time, each channel corresponds to a certain velocity of the source. The cathod ray oscilloscope displays the data stored by the memory unit of MCA, and Microprocessor unit (6809) is used to store the data and later on transfer it to the university main computer (CDC), where it is analyzed. The transfer procedure and the system of operation is described later in this chapter, while description of the computer programme and analysis is discussed in section(3.8).

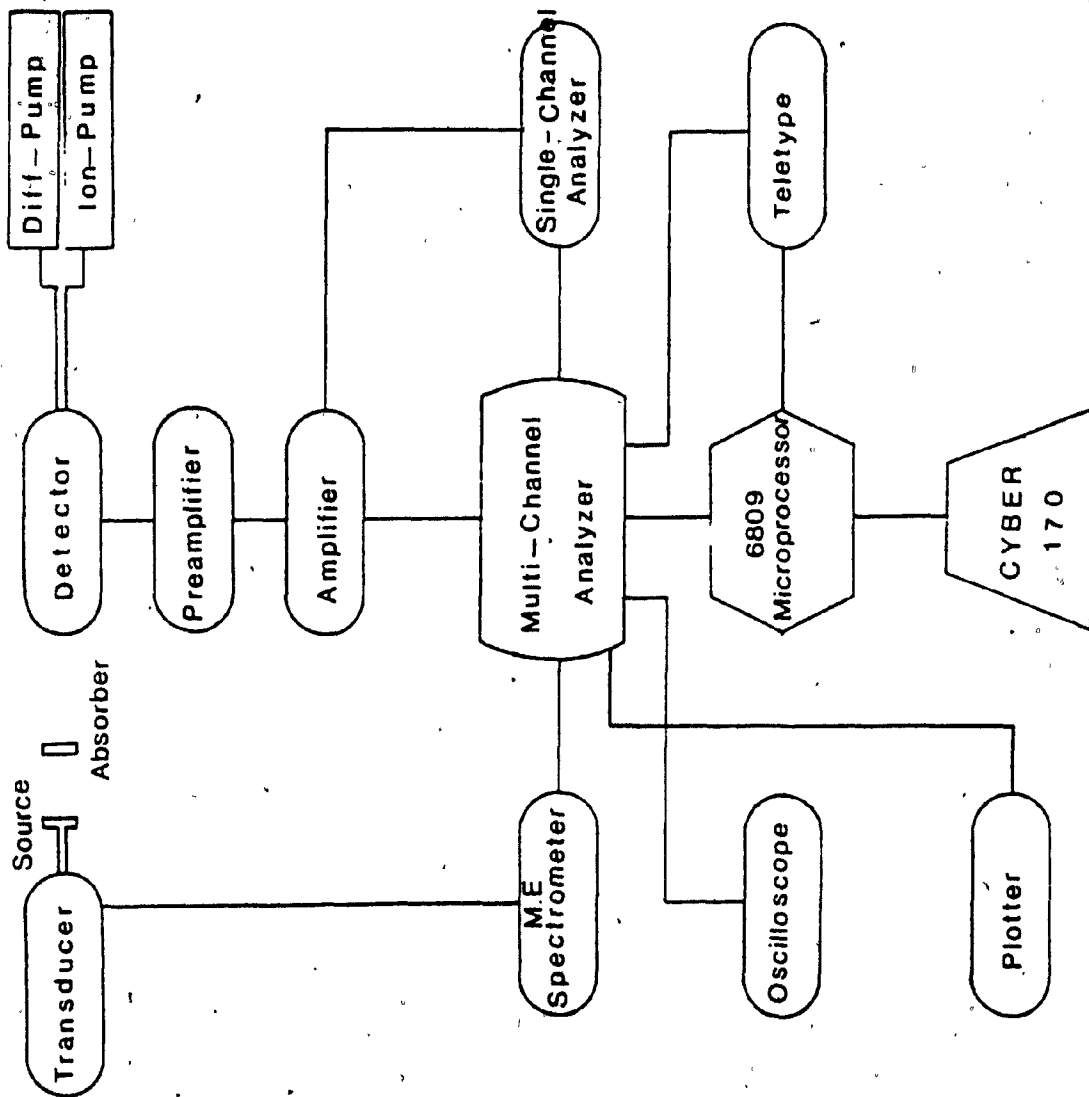


Fig. 5 . Block diagram of the Mössbauer experiment

A block diagram of the experiment is shown in Fig.5. and in the remaining of this chapter each important unit in the diagram is described seperately. The calibration procedure is also included.

3.2. SOURCE

The source used, ^{57}Co , was of about 40 millicurie strength, with specific activity about 8.0×10^3 mci/mg manufactured by NEN Co. A 40 mci portion of ^{57}Co was electrodeposited onto a 6mm diameter area of a 12.5 mm overall diameter Palladium foil of 0.025 mm thickness, and then it was sprayed with an acrylic coating to retard oxidation and to minimize contamination problems. The decay scheme of ^{57}Co is illustrated in Fig.6.

There are a number of criteria which are important in choosing a host matrix. First, the source should give the narrowest possible Lorentzian line to ensure the best resolution. It is essential that each source atom is present in precisely equivalent lattice position having cubic symmetry. Second, the source should have as large an f factor as possible so that good absorption is obtained. Third, the host matrix should not give rise to X-rays, and Compton scattering and photoelectric processes should be minimized. The source lattice should have a high Debye temperature. When Mössbauer nucleus is introduced as an impurity in the source lattice the effective Debye

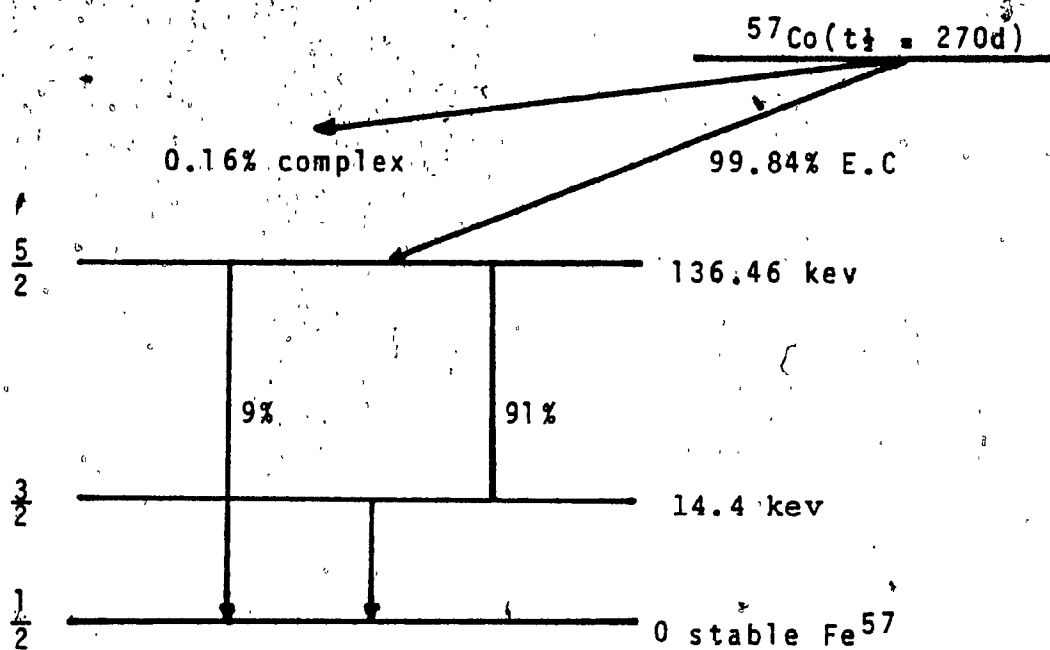


Fig.6. Decay Scheme of ⁵⁷Co.

Table 2. Isomer shift scale; relative to sodium nitro prusside at 300°K.

Material	I.S (mm/sec)
Na ₂ Fe(CN) ₅ NO.H ₂ O	0.
Cr	0.106±0.009
Stainless Steel	0.17±0.02
α-Iron	0.260±0.002
Pd	0.437±0.002
Cu	0.485±0.002
Pt	0.609±0.006

temperature is given by:²

$$\theta_{\text{eff}} = \theta_D \left[\frac{m_{\text{host}}}{m_{\text{imp}}} \right]^{1/2} \quad (21)$$

where m_{host} and m_{imp} are the masses of the host and impurity atoms respectively, and θ_D is the Debye temperature of the lattice.

Palladium source is one of the most suitable one, since it satisfies all the above conditions.

3.3 DRIVE SYSTEM

As mentioned in the previous chapters, a Mössbauer spectrum consists of a plot of the number of gamma ray photons transmitted through an absorber as a function of the instantaneous relative velocity of the source with respect to an absorber. The Mössbauer spectrometer is an apparatus which imparts the velocity to the source (or absorber). It also coordinates the counting rate at the detector so that the spectrum channel number will be a function of the source velocity.

The spectrometer used is the model AM-1, manufactured by Nuclear Science and engineering Corporation. It consists of three parts:

- i- The Base Plate- a solid aluminum plate on which the transducer, the source and the absorber holder are mounted.
- ii- The Transducer- a precision electromechanical unit which provides a forward and retrograde motion to the source with

constant acceleration. The operating frequency range is 15-50 CPS and the velocity range is 0-60 cm/sec.

iii- The Control Unit- a solid state electronic unit which accepts a square wave signal from the address register of a multi-channel analyzer.

In Fig.7. the drive velocity wave form, the corresponding channel advance, and an absorption spectrum for a single line source and absorber, are displayed.

3.4. DETECTOR

The detector used is a Si(Li) drift solid-state detector, with an area of 50 mm² and the beryllium oxide window of 250 μ thickness, manufactured by Simtec Ltd. model K-036.

3.5. AMPLIFICATION SYSTEM

The system consists of a pre-amplifier and a linear amplifier models P-11 HR/CN and M-31 manufactured by Simtec Ltd. The pre-amplifier is a cooled N-channel FET optimized for Simtec ultra high resolution silicon and germanium photon spectrometer elements with capacity less than 10 picofarads. The detector and the FET pre-amplifier are kept at temperature of liquid nitrogen. This requires low pressure in the Cryostat, which is attained by a mechanical diffusion pump and monitored by an ion appendage pump control. The 14.4 Kev gamma rays are selected by a

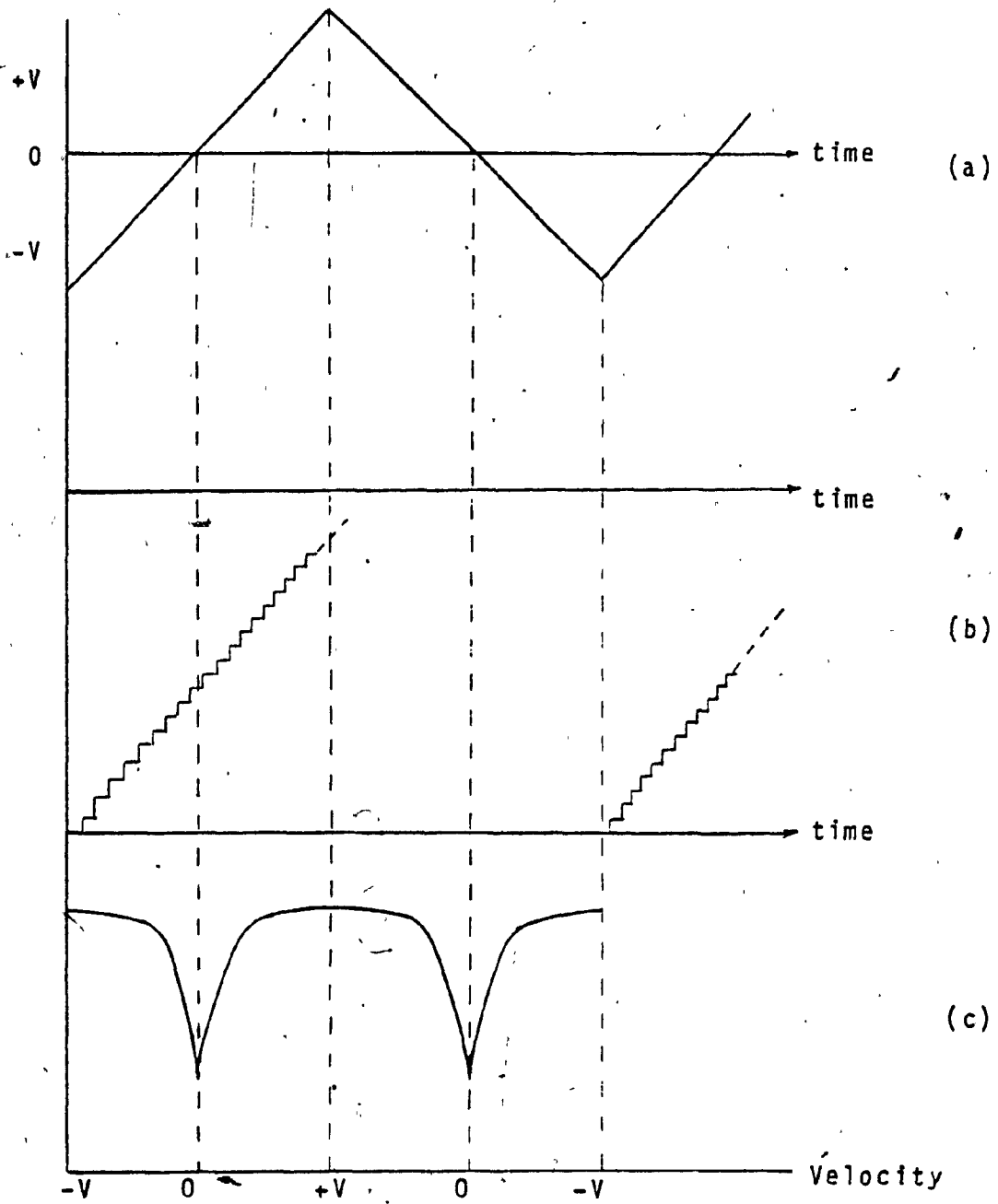


Fig.7. (a) Drive velocity wave form.
 (b) Corresponding channel advance.
 (c) An absorption spectrum.

Hewlett-Packard 5583 A single channel analyzer.

3.6. MULTI CHANNEL ANALYZER (MCA)

The MCA used is the series 2200 Nuclear Data system analyzer. The versatility of this system is exemplified in that analog to Digital Converter, Master Control, Read-In/Out Display, and system memory.

i- The analog to Digital Converter (ADC)- is designed primarily for the processing of amplitude modulated signal pulses such as encountered in pulse height analysis. Data acquisition efficiency is enhanced by a 50 megahertz digitizing rate.

ii- Master Control- it contains facilities for establishing the primary operating modes (data acquisition, display, read-in and out) and all the data handling functions of the system.

iii- Read In/Out Display- it incorporates those features necessary for selection of a particular type of read out or control of the appropriate device. This unit is capable of driving high speed digital printers and X-Y plotters.

iv- System Memory- it is divided into three modules: The Memory Scalar Module- contains the memory address scalar and register which allows the content of a single channel to be transferred back into the identical channel location of the memory.

The Memory Drivers Module- consists of all the driving and sensing circuits for the Memory Array Module which permits

proper handling of the data being stored.

The Memory Array Module- is designed in a manner that allows expansion up to a maximum size of 24-bit, 4096 channels.

The Series 2200 System Analyzer can be constructed in sizes of 512, 1024, 2048 and 4096 channels. 512 channels was used in our experiments.

3.7. CALIBRATION

It is essential to have a method of accurately measuring the total energy scan of the source radiation, and also to have a standard reference line position against which other positions may be quoted. The latter point is especially important, since the different sources used (e.g, ⁵⁷Co. in Pd, Cr, Cu) all emit gamma rays of slightly different energy.

The inner four lines of the six lines spectrum of a natural iron foil is used for calibration. This is justified by the velocity ranges during the experiment (4-->10mm/sec) . The assignment of the velocities for the peaks obtained in our experiment, ensure the elimination of any error in position and the parameters derived, such as the isomer shift and quadrupole splitting.

The centroid of the two line Sodium Nitroprusside (SNP) spectrum is now widely used as a reference velocity in

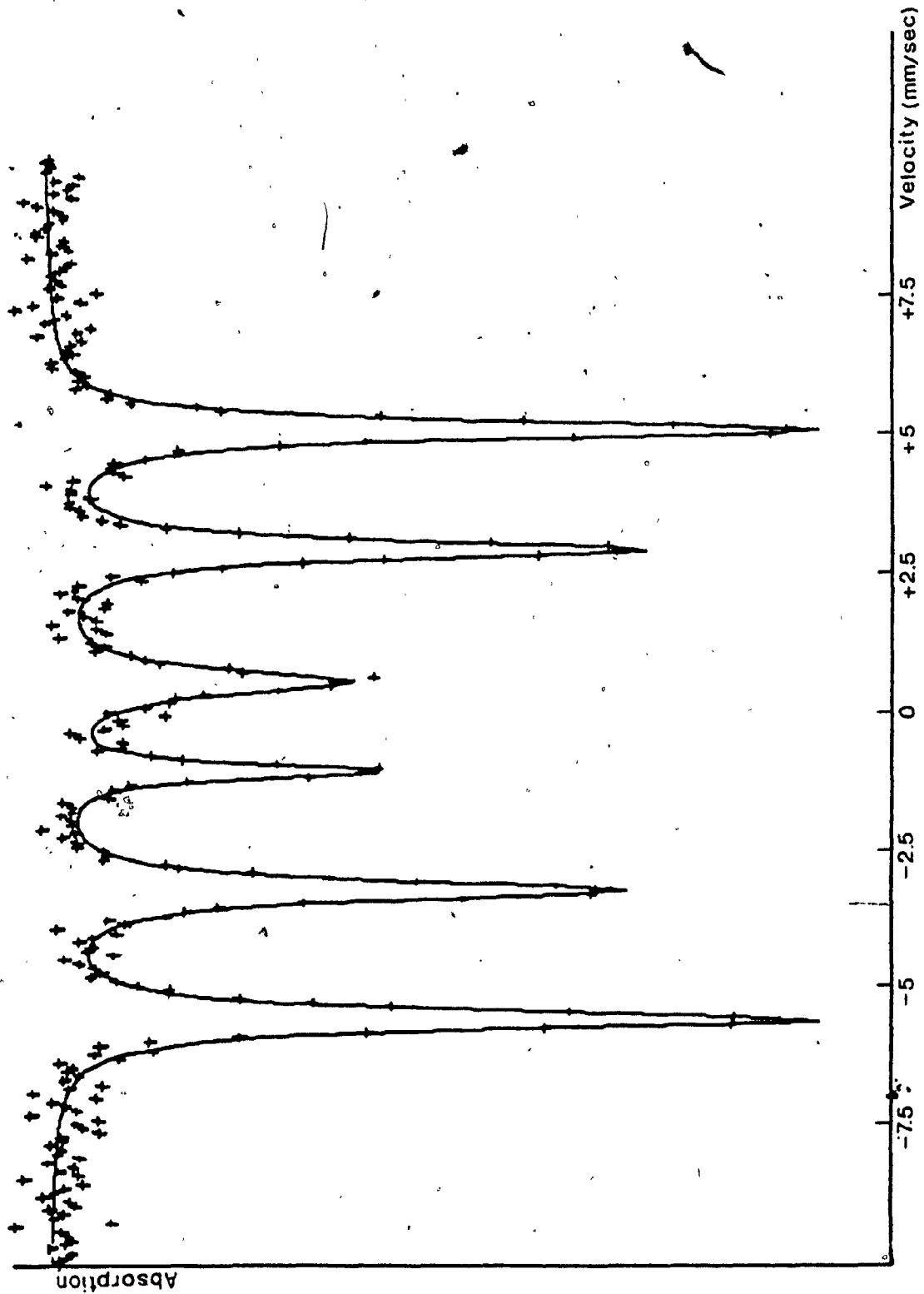


Fig. 8 . Computer plot of the Mössbauer spectra of an Iron foil (10 mm/sec)

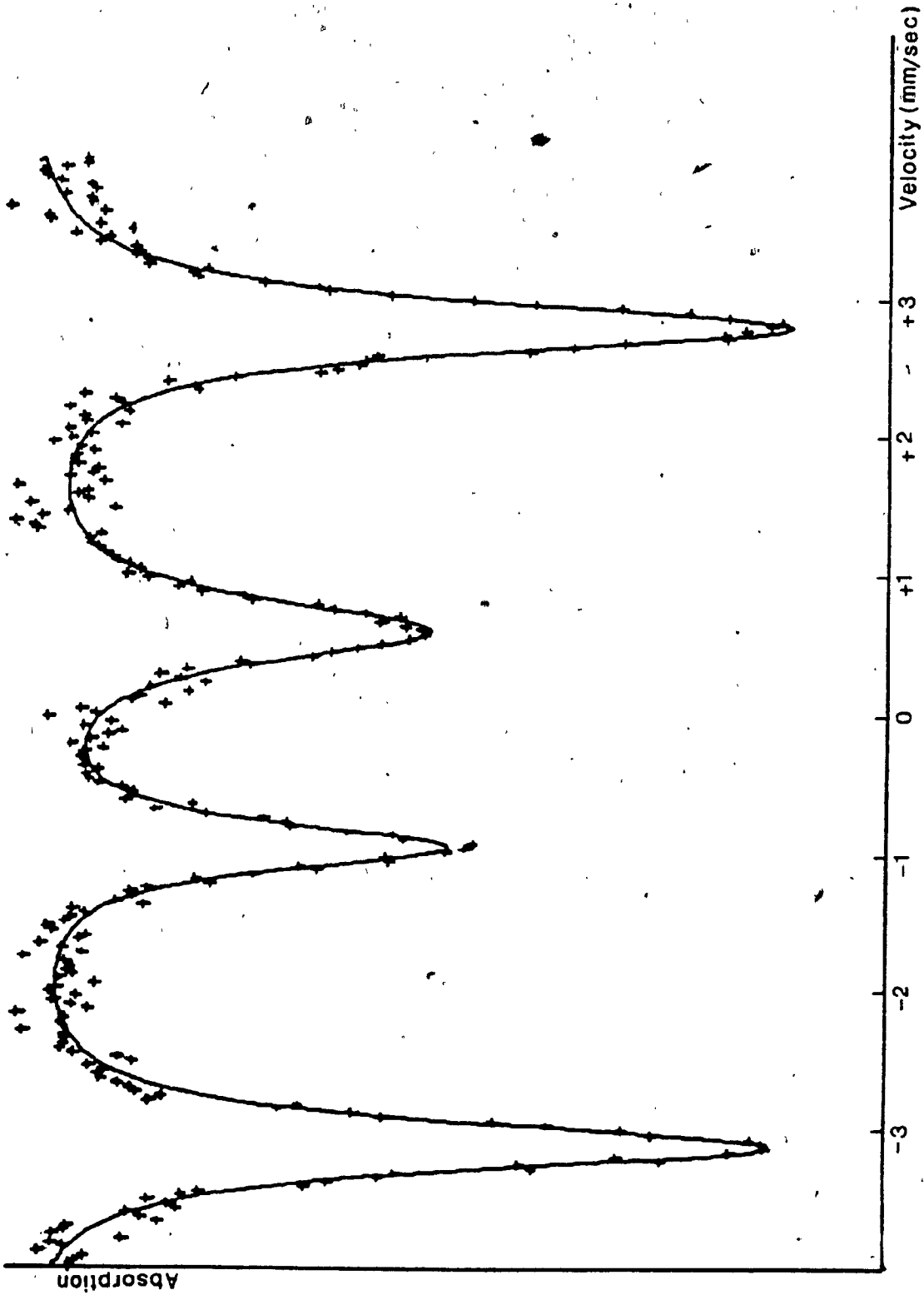


Fig. 9. Computer plot of the Mössbauer spectra of an Iron foil (4 mm/sec)

isomer shift scale. Table.2. shows the isomer shift of different source materials relative to (SNP). (also, see App.D) All isomer shift values reported in this work are relative to (SNP). Figures 8 and 9 show the iron spectra obtained at 10 and 4 mm/sec respectively.

In order to obtain the spectra of Fe^{3+} in GASH in 2mm/sec velocity range, the spectrometer was calibrated by adjusting the velocity drive control. This was done by using the known positions (channel numbers) of the peaks corresponding to 4-peak resolution of an iron foil. The velocity increment per channel was calculated to be 0.0186 mm/sec.

3.8. DATA TRANSFER

Transfer of data from the memory unit of the Multi channel analyzer to the university main computer (CDC), was carried out through the Microcomputer 6809. The 6809 is linked to the MCA, Teletype and CYBER by an MP-LA parallel interface board and two MP-S serial interface board respectively (Fig.5). The commands that drive the system are given through the teletype. The data are read to the memory of the 6809 from the MCA by the programme MCA READ (Appendix B), and then are transferred to the CYBER by the programme 6809 READ (Appendix B), where from they can be used for analysis.

CHAPTER IV
ANALYSIS OF SPECTRA

4.1. COMPUTATIONAL METHOD

The line shape of a peak in Mössbauer spectra is essentially an ideal Lorentzian. In order to obtain the most precise estimates of peak parameters, it is essential to compute the spectra. If 256 channel multi-channel analyzer^v is used, the observed spectrum consists of 256 numbers defining an envelope. The problem thus consists of finding the positions, widths and intensities of a number of Lorentzian lines which, when superimposed, give the best fit to the observed envelope. The line shape, $I(v)$, of the envelope for a Lorentzian line is given by:^{1,3,17}

$$I(v) = b + I(0)/[1 + (\frac{v - v(0)}{\Gamma/2})^2] \quad (22)$$

where $I(0)$ is the intensity at the resonance velocity $v(0)$, Γ is the width at half height, and b is the baseline intensity. For n lines, the above equation becomes:

$$I(v) = b + \sum_{i=1}^n \frac{I(0)}{1 + [(v - v(0))_i / (\Gamma/2)]^2} \quad (23)$$

For an n line spectrum, $I(v)$ is a function of $3n+2$ parameters, position, width, and intensity of each line, plus the baseline and the slope of the baseline. The best fit ideally should correspond to the minimum weighted sum of squares χ^2 , as given by:^{1,3,17}

$$\chi^2 = \sum_{r=1}^{256} W_r [(I_r - I(v_r/q_i))]^2 \quad (24)$$

where I_r is the observed count at channel r , $I(v_r/q_i)$ is the

transmission function, q_i denotes the $3n+2$ parameters, and W_r is the inverse of the variance for channel r . Initial estimates are chosen for the $3n+2$ parameters q_i , and using

$$d\chi^2/dq_i = 0 \quad (25)$$

for each q_i , corrections are determined for each q_i such that χ^2 is minimized. This constitutes one iteration. The procedure is then repeated using the corrected estimates from the previous iteration, until the value of χ^2 obtained reaches a minimum.

In our experiment this fitting is carried through the programme Mössbauer (Appendix A). Mössbauer consists of a main block and several subroutines. The main block reads in the data, applies corrections to it and prints the results. Subroutine FUNC calculates the function derivatives, Subroutine CURFIT carries the least square fitting, subroutine MATINEV is for matrix inversion and accompanying solution of linear equations, subroutine JACOBI is for matrix diagonalization through successive rotations, subroutine EXAM applies corrections to the eigenvalues if any is zero or negative otherwise the fitting will diverge, while subroutine PLOTB plots the raw and calculated spectra.)

4.2. LINE WIDTH, SHAPE, AREA

According to the Heisenberg uncertainty principle $(\Delta E)(\Delta t) \geq \hbar$, no measurement or observation of the two conjugate variables can be made simultaneously with higher

accuracy than stated in the above formula. It can also be expressed for momentum and position or other conjugate variables. Δ indicates the uncertainties in the properties (E and t).

Applying this principle to Mössbauer transitions, we recall that in a recoil-free transition from an excited nuclear state to the ground state no energy is lost to the system, and the gamma-ray carries the total energy of this transition. The excited state has a mean lifetime τ or half lifetime $t_{1/2} = \tau \ln 2$. The ground state is stable, or has a long lifetime, and its energy level is well defined. Therefore, the uncertainty relation for this case is given from resonance theory as:

$$\Gamma = \Delta E = \hbar/\tau = \frac{0.693\hbar}{t_{1/2}} \quad (26)$$

where Γ is called the natural line width of the source emission or the absorption line. The line width is defined as the full width at half maximum. The first excited state of ^{57}Fe (14.4 Kev) has a value of $t_{1/2} = 10^{-7}$ sec. Thus, the natural line width is $\Gamma = 5 \times 10^{-9}$ ev.

In the experiment, the line broadened by several effects, one of which is so called Thickness Broadening. The experimental full width at half height can be expressed as:

$$\Gamma_{\text{ex}} = \Gamma_a + \Gamma_s + 0.27 \Gamma_X \quad (27)$$

where: $\Gamma_a + \Gamma_s$ is the width of Γ_{ex} extrapolated to $X=0$.

Γ is the natural line width and $X = n f_a \sigma$. where: n is the number of atoms of the Mössbauer isotope per cm^2 , f_a is the recoil free fraction of the absorber and σ is the maximum cross section at resonance, given by:^{1,3,17}

$$\sigma = 2\pi\lambda^2 (2I_e + 1) / [(2I_g + 1)(\alpha_t + 1)] \quad (28)$$

For iron this is $2.569 \times 10^{-18} \text{ cm}^2$. I_e and I_g are the nuclear spins of the excited and ground state respectively, and $\lambda = 2\pi\lambda$ is the wavelength of the gamma-ray. α_t is the total internal conversion coefficient and takes into account the competing mode of the transition. For ^{57}Fe , α_t is in the order of 10.

Resonance absorption shows a characteristic energy dependence of the form:^{1,3,17}

$$I(E) = \Gamma_{\text{ex}} / 2\pi \left[1 / ((E - E_t)^2 + (1/2 \Gamma_{\text{ex}})^2) \right] \quad (29)$$

where E_t is the nuclear transition energy. For ^{57}Fe , this equals 14.4 Kev. This distribution is said to show a Breit-Wigner, or Lorentzian shape.

The area A under a peak for a "thin" Lorentzian one line absorber and a single-line source of arbitrary width may be expressed as:¹

$$A = 1/2 \pi f_s f_a \sigma \Gamma_{\text{ex}} G(X) n \quad (30)$$

where f_s is the recoil free fraction of the source and $G(X)$ approaches one as X approaches zero, i.e. as $n f_a \sigma \rightarrow 0$. As X increases, $G(X)$ decreases. The ratio of the number of iron atoms in two different sites can be determined from the

ratio of areas i.e. $A_2/A_1 \propto n_2/n_1$. The use of area ratios is discussed in detail in chapter 5.

Computer programme, as developed by Dr. S. K. Misra, for the 'least-squares curve fitting' is given in Appendix A.

CHAPTER V
MÖSSBAUER SPECTROSCOPY IN
GEOLOGY AND MINERALOGY

5.1. INTRODUCTION

The mineralogical and geochemical application of Mössbauer spectroscopy have developed rapidly over the last decade. A large number of investigations were subsequently carried out with a considerable divergence of interests to collect data of geological significance. In view of the great importance of iron in the earth's crust and the widespread occurrence of this element in rock-forming minerals, earth scientists naturally focussed their attention on application of ^{57}Fe resonance.

Typical applications of Mössbauer spectroscopy to mineralogy and geology have been the analysis of the oxidation state of iron at iron sites in minerals. In certain crystal structures, e.g. chain silicates, lattice positions may be occupied by ferric and ferrous iron in various proportions. The assignment of distinct hyperfine patterns in a Mössbauer spectrum to non-equivalent lattice positions has allowed site preference of Fe^{2+} or Fe^{3+} ions in minerals to be determined. The assignment may be deduced from the observed isomer shifts, and quadrupole splittings. Figures 10a and b show Fe centre shifts and quadrupole splitting plotted versus coordination number for "ionic" high spin and low

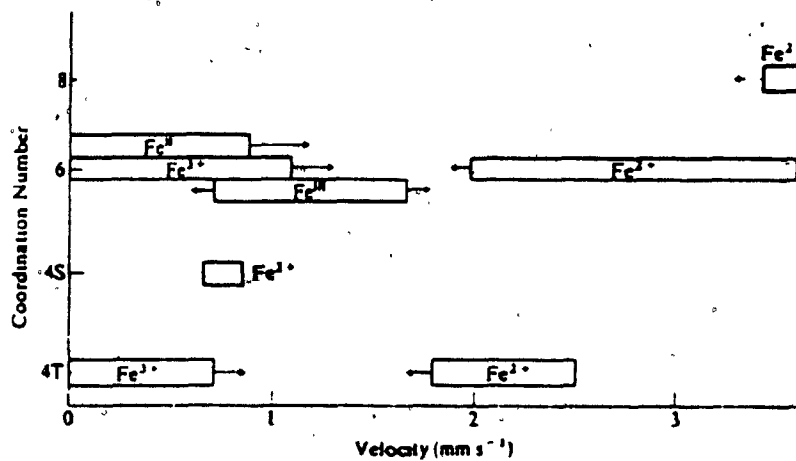
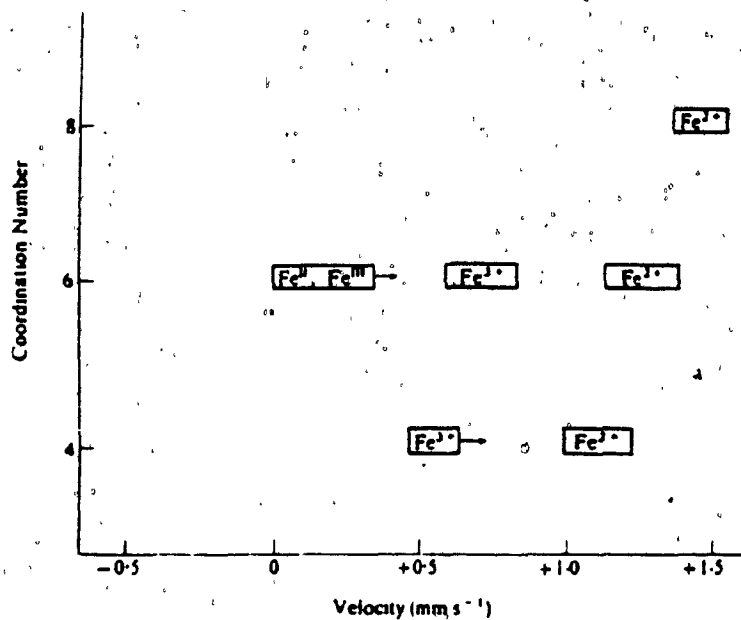


Fig.10. ^{57}Fe Centre shift (top), and Quadrupole splitting (bottom) plotted versus coordination number for "ionic" high spin and low spin compounds and minerals. Arrows indicate that values outside the boxed areas have been observed.¹

spin compounds and minerals.

The study of area ratios of distinct hyperfine patterns has led to thermodynamical analysis of order-disorder phenomena in minerals. Chemical analyses together with optical and density measurements may suggest ordering, but site populations can not be estimated. If a mineral contains two different types of iron atoms A and B which give rise to non overlapping Mössbauer spectra, the area ratio for a thin absorber can be expressed as:

$$A_A/A_B = C N_A/N_B \quad (31)$$

Where the constant C is given by:

$$C = [\Gamma_A G(X_A) f_A] / [\Gamma_B G(X_B) f_B] \quad (32)$$

A_A and A_B are the areas of lines A and B respectively and N_A and N_B are the numbers of iron atoms at sites A and B respectively. In equation 32, Γ is the line width, $G(x)$ represents saturation correction given by equation 30 where for very thin absorbers $G(x)$ approaches unity. f_a and f_b are the recoil free fractions for A and B.

The areas can be determined directly from the spectra. The usual error associated with measuring areas-background is minimized in the area ratio, since the background corrections for the two iron atoms are similar. If C can be determined or estimated, the ratio of iron atoms in the two different sites can be determined. Unfortunately, for most silicates it is difficult to obtain an accurate

estimate of C. For most silicates, C is assumed to be 1.¹

The widths of most mineral peaks have been found to be closely equal if the same source is used.

In the remainder of this chapter some of the mineralogical and geochemical properties of pyroxenes and garnets are presented.

5.2. PYROXENES ¹³

Pyroxenes are the most important group of rock-forming ferromagnesian silicates, and occur as stable phases in almost every type of igneous rock. They are found also in many rocks of widely different compositions formed under conditions of both regional and thermal metamorphism.

The pyroxenes include varieties which have orthorhombic symmetry (orthopyroxene), and monoclinic symmetry (clinopyroxene). The orthopyroxenes consist essentially of a simple chemical series of $(\text{Mg}, \text{Fe})\text{SiO}_3$ minerals, in contrast with the larger sub-group of monoclinic pyroxenes which have a very wide range of chemical compositions. The compositions of the pyroxene minerals are given in Table.3.

The majority of pyroxenes which are present in both igneous and metamorphic rocks can be considered, as a first approximation, to be members of the four component system

Table 3. Compositions of the Pyroxene minerals.

Monoclinic Pyroxenes:

Diopside-Hedenbergite	$\text{Ca}(\text{Mg}, \text{Fe}^{2+})\text{Si}_2\text{O}_6$
Augite	$(\text{Ca}, \text{Mg}, \text{Fe}^{2+}, \text{Fe}^{3+}, \text{Ti}, \text{Al})_2(\text{Si}, \text{Al})_2\text{O}_6$
Aegirine	$\text{NaFe}^{3+}(\text{Si}_2\text{O}_6)$
Aegirine-Augite	$(\text{Na}, \text{Ca})(\text{Fe}^{3+}, \text{Fe}^{2+}, \text{Mg}, \text{Al})(\text{Si}_2\text{O}_6)$
Johannsenite	$\text{CaMnSi}_2\text{O}_6$
Spodumene	$\text{LiAlSi}_2\text{O}_6$
Jadeite	$\text{NaAlSi}_2\text{O}_6$
Pigeonite	$(\text{Mg}, \text{Fe}^{2+}, \text{Ca})(\text{Mg}, \text{Fe}^{2+})(\text{Si}_2\text{O}_6)$
Omphacite	$(\text{Ca}, \text{Na})(\text{Mg}, \text{Fe}^{2+}, \text{Fe}^{3+}, \text{Al})(\text{Si}_2\text{O}_6)$
Fassite	$\text{Ca}(\text{Mg}, \text{Fe}^{2+}, \text{Fe}^{3+}, \text{Al})(\text{Si}, \text{Al})_2\text{O}_6$

Orthorhombic Pyroxenes:

Enstatite-Orthoferrosilite	$(\text{Mg}, \text{Fe}^{2+})_2\text{Si}_2\text{O}_6$
----------------------------	------------------------------------------------------

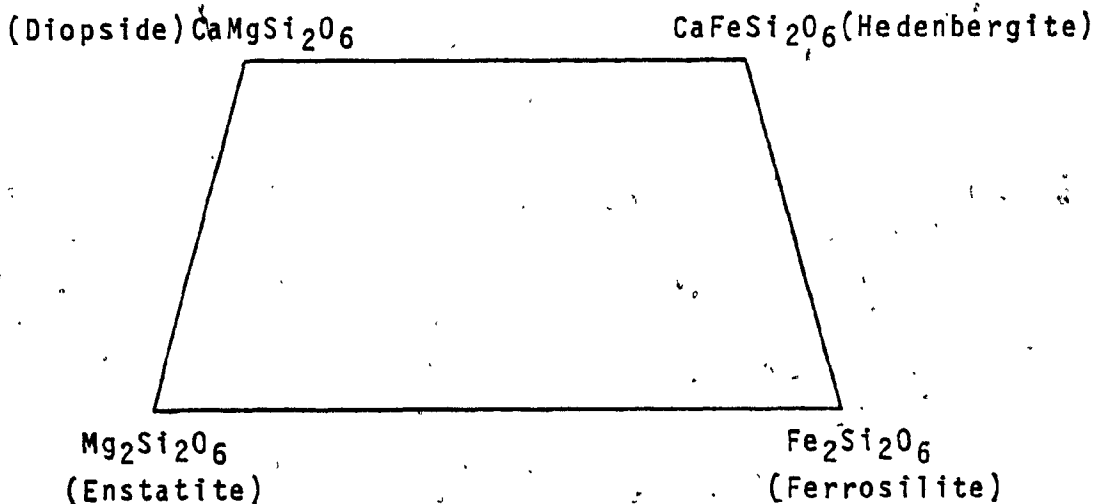
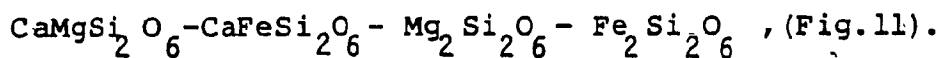


Fig. 11. Composition of important pyroxenes in the system Diopside-Hedenbergite-Enstatite-Ferrosilite.



¹³
 The general chemical formula for pyroxenes proposed by Berman (1937) and later slightly modified by Hess (1949) can be expressed as $(\text{W})_{1-p}(\text{X},\text{Y})_{1-p}\text{Z}_2\text{O}_6$, where $\text{W}=\text{Ca},\text{Na}$, $\text{X}=\text{Mg}, \text{Fe}^{2+}, \text{Mn}, \text{Ni}, \text{Li}$, $\text{Y}=\text{Al}, \text{Fe}^{3+}, \text{Cr}, \text{Ti}$, and $\text{Z}=\text{Si}, \text{Al}$. The value of P varies from zero to 1 for monoclinic pyroxenes. In the orthopyroxene series $P=1$ and the content of Y ions is small. The wide range of replacements in the (X,Y) group commonly involving substitution of ions of different charge necessitates compensatory replacements in either the W or Z groups and the replacements must be such that the sum of the charges in the $\text{W},\text{X},\text{Y}$ and Z group is 12.

STRUCTURE¹³

The essential feature of all pyroxene structures is the linkage of SiO_4 tetrahedra by sharing two out of four corners to form continuous chains of compositions $(\text{SiO}_3)_n$ (Fig. 12). The chains are linked laterally by cations ($\text{Ca}, \text{Na}, \text{Mg}, \text{Fe}^{2+}$, etc.), but may have various dispositions relative to one another.

There are two crystallographically distinct cation positions labelled M_1 and M_2 (Fig. 13.). The cations in the smaller M_1 positions are coordinated to six oxygen atoms in a nearly regular octahedron, while the cations in the larger M_2 positions are coordinated to a varying number of oxygens in

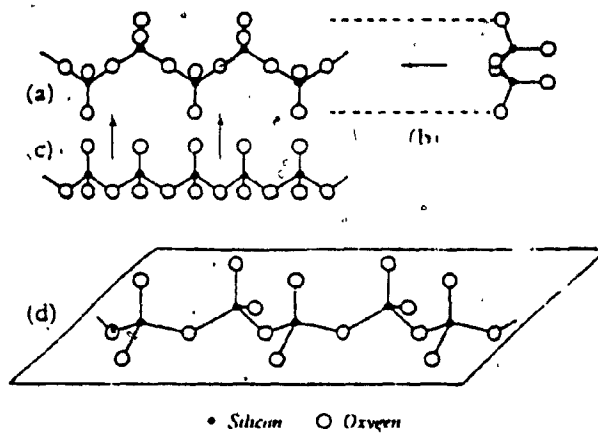


Fig.12. Idealized illustration of a single pyroxene chain.
 (a) Projected on (100); (b) Along the Z direction;
 (c) Along the Y direction; (d) In perspective!³

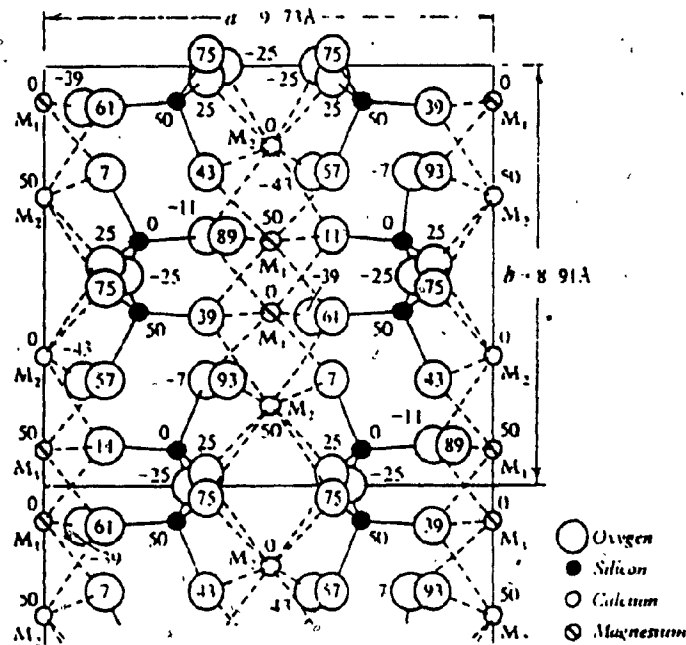


Fig.13. Idealized structure of diopside; viewed along the Z direction. The numbers indicate the relative position of each atom.¹³

a very distorted environment. For example, the coordination number for the M_1 position varies from six to seven to eight in hypersthene, pigeonite and diopside respectively. In diopside structure (Fig.13.) the Mg ions are in octahedral coordination by oxygens which themselves are linked to only one silicon, while the larger Ca ions are surrounded by eight oxygens, two of which are shared by neighbouring tetrahedra in the chains.

Pyroxenes in the field $CaMgSi_2O_6 - CaFeSi_2O_6 - MgSiO_3 - FeSiO_3$ (Fig.11) can be divided into two structural groups. One is near $CaMgSi_2O_6 - CaFeSi_2O_6$, these exist only in the monoclinic form, have the space group C2/c and are structurally similar to diopside. The other group lies near $MgSiO_3 - FeSiO_3$ join and have the monoclinic and orthorhombic forms, depending on the temperature and the percentage of $FeSiO_3$ content.

¹³Pyroxenes with compositions outside the field diopside - hedenbergite - ferrosilite - enstatite all have a clinopyroxene structure. Before the structure of diopside had been determined by Warren and Bragg, (1928), Wyckoff et al. (1925) had shown that X-ray powder patterns of aegirine, jadeite, diopside, hedenbergite and augite were all similar. Single - crystal investigations by Warren and Bischof (1931) confirmed this result for these minerals.

5.3. GARNETS⁷

The garnets are a widespread group of minerals that occur in a variety of geological environments. They are found in igneous rocks, as detrital grains in clastic sedimentary rocks, and most commonly in the metamorphic environment, in both regionally and in contact metamorphosed areas. They are also widespread in the metasomatic environment, particularly where calcium-rich alkaline fluids are involved. Garnets exhibit a wide range of chemical compositions but similar structural properties. Because of the interest of the electronics and communication industries to the magnetic and electrical properties of some natural and synthetic garnets, they have been extensively studied as a group, in recent years. The compositions of the most common garnet minerals are given in Table.4.

The garnets are all transparent, dense (S.G. 3.8-4.5), refractory minerals, characterized by cubic symmetry (space group $Ia\bar{3}d$, $a=11.5-12.5 \text{ \AA}$), high refractive index ($n=1.7-1.94$), and isotropism. Some display anomalous anisotropy. Hardness ranges from 6.5 to 7.5. Garnets display all colours of the visible spectrum except blue. They do not possess cleavage.

The general formula of garnets can be expressed as $X_3 Y_2 (SiO_4)_3$, in which X is usually a divalent cation, and includes $Ca^{2+}, Mg^{2+}, Fe^{2+}, Mn^{2+}, Y^{3+}$. Y is usually trivalent, and includes $Al^{3+}, Cr^{3+}, Fe^{3+}, Mn^{3+}, Ti^{3+}, Ti^{4+}, V^{3+}$ and Zr^{4+} .

Table 4. Compositions of the most common garnet minerals.

	Pyrope	$Mg_3Al_2(SiO_4)_3$
	Almandine	$Fe_3Al_2(SiO_4)_3$
	Spessartite	$Mn_3Al_2(SiO_4)_3$
	Grossularite	$Ca_3Al_2(SiO_4)_3$
	Uvarovite	$Ca_3Cr_2(SiO_4)_3$
	Andradite	$Ca_3Fe_2(SiO_4)_3$
	Goldmanite	$Ca_3V_2(SiO_4)_3$
Rare-	Yamatoite	$Mn_3V_2(SiO_4)_3$
Earth	Kimzeyite	$Ca_3Zr_2(Al_2Si)O_{12}$
Group	Ferrikimzeyite	$Ca_3Zr_2(Fe_2Si)O_{12}$
	Yttrogarnet	$Y_3Al_2(Al)_3O_{12}$
	Calderite	$Mn_3Fe_2(SiO_4)_3$
	Hydrogarnet	$Ca_3 X_2(SiO_4)_{3-X}(OH)_{4X}$

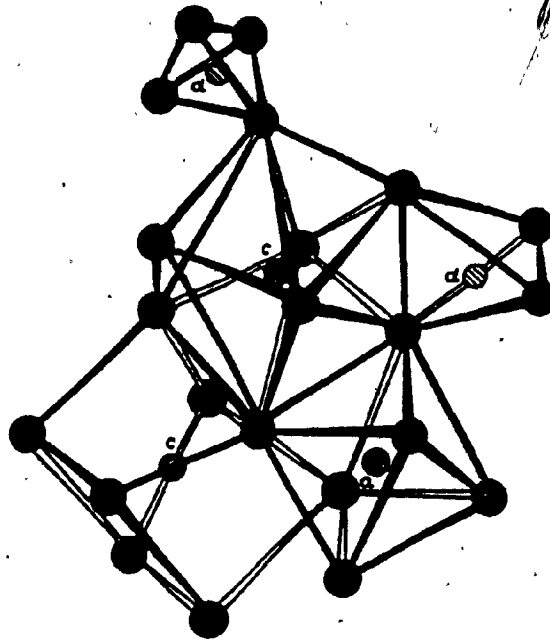


Fig.14. A portion of the garnet structure with cation and oxygen atoms labeled as:

a : Y (trivalent cation) Octahedral site

c : X (divalent cation) Dodecahedral site

d : Si Tetrahedral site

STRUCTURE⁷

The structure of garnets consist of three-dimensional link-up of chains of alternating octahedra and tetrahedra. Included in this array are eight-fold dodecahedral sites (Fig.14). In this structure , X(divalent cation) enters the dodecahedral site, Y(trivalent cation) enters the octahedral site, whereas Si enters the tetrahedral site.

CHAPTER VI

THE SULLIPEK SKARNS

6.1. INTRODUCTION

The samples investigated are skarns from the Sullipek deposit (copper-molybdenum), located in Lesseps county, Gaspé, Quebec and were collected and made available to the writer by Mr. Robert Wares of McGill University. The following description of Sullipek skarns and their geological setting are also taken from Wares.⁷

6.2. GEOLOGICAL SETTING

The skarns occur in the upper-Silurian to lower Devonian West Point formation located in the Connecticut Valley Synclinorium in the Appalachian foldbelt. The sequence containing the West Point formation starts with a quartz arenite (Val-Brillant) which is overlain by dominantly carbonate formations (Sayabec, Gascons, West Point) of shallow water origin, deposited in an area of active block faulting. The overlying siltstones of the Indian Point formation indicates deposition in deeper water.

The West Point formation consists of reefal limestones and limestone conglomerate. Fragments in the conglomerate are 2.5 to 50 cm across and contain stromatoporoids, echinoderms and corals. In the conglomerates are interbeds of black and grey micrite and calcareous siltstone. It

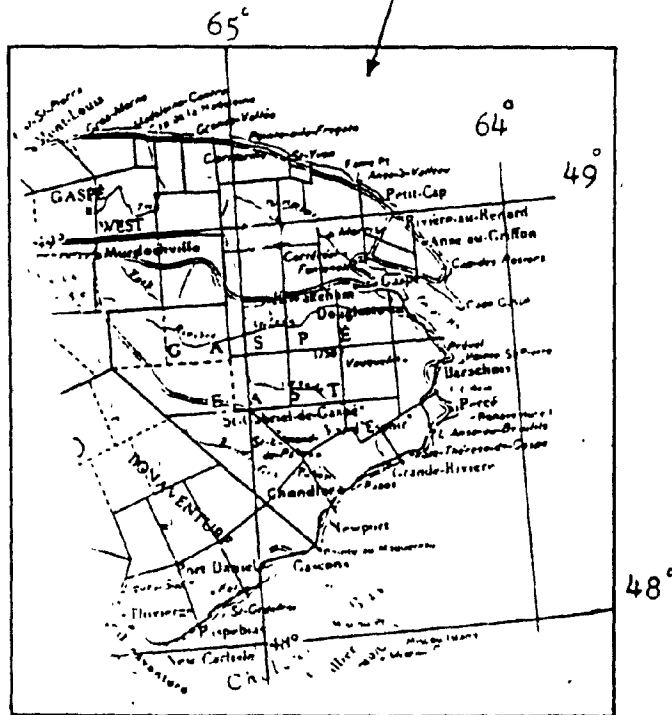
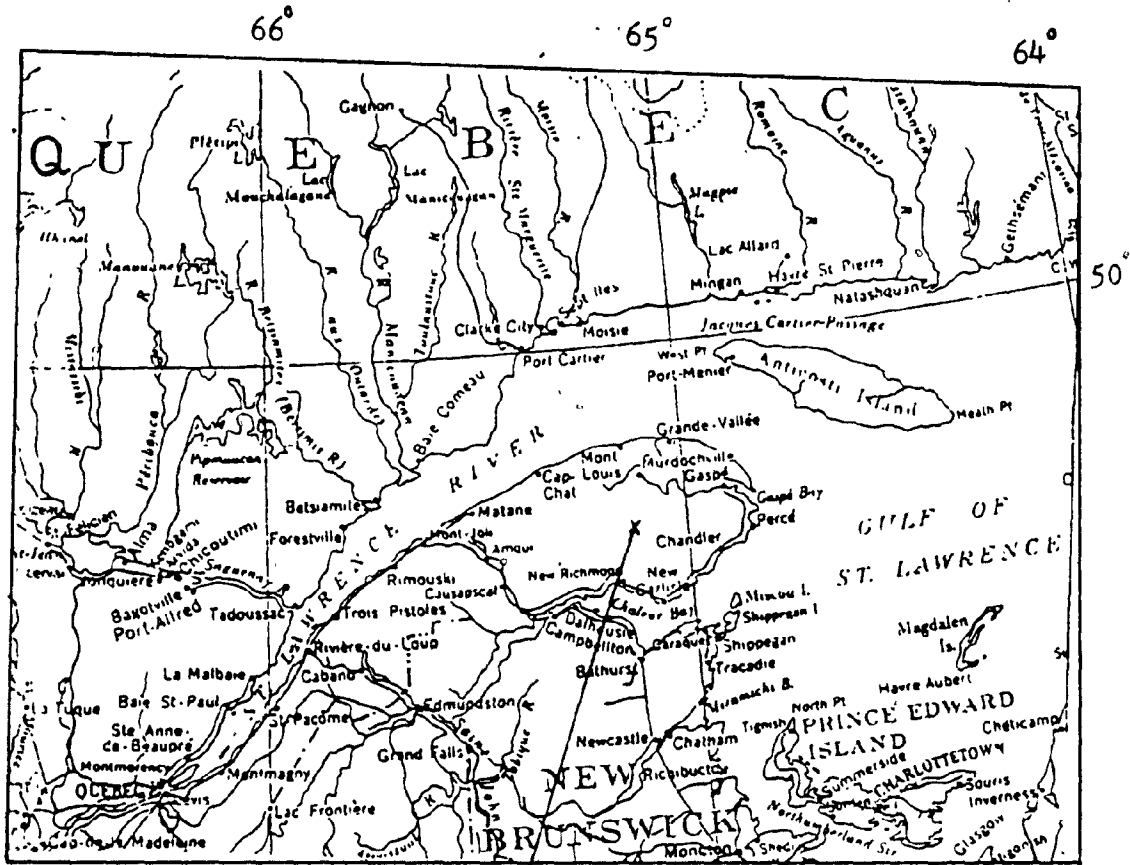


Fig.15. The Geographical location of the deposit.

appears that the reefs grew on the tops of the horsts while the adjacent garbens were periodically filled with conglomerate resulting from mass-flow off the reef front. The West Point formation can therefore vary substantially in thickness.

The Sullipek deposit lies on the north limb of the Lesseps syncline, a major regional fold of Acadian origin. Its axis lies approximately (520 m) to the south of the deposit and trends 245°.

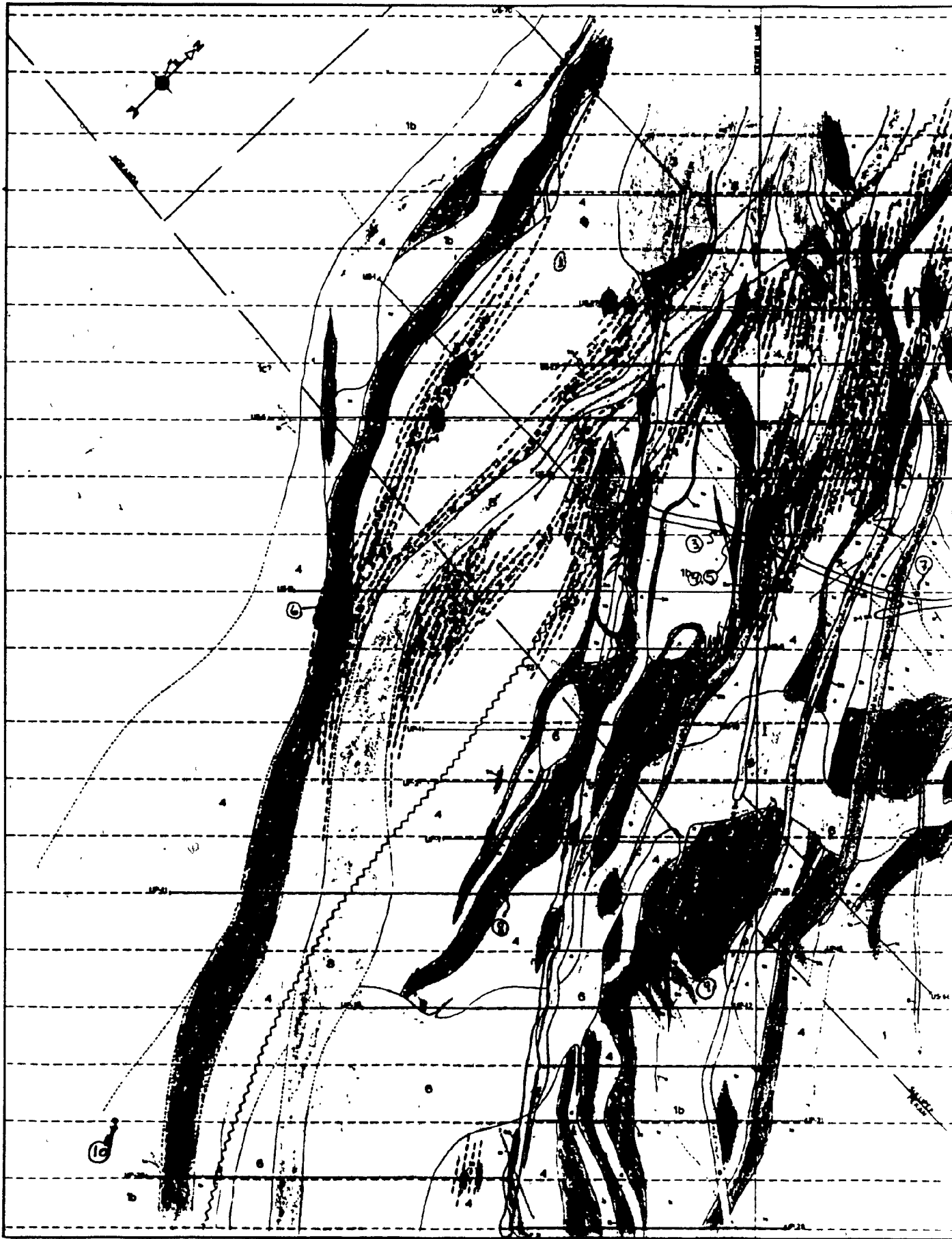
The region as a whole is intruded by Devonian plutons and related dykes and sills of dominantly silicic composition. In the Sullipek area five distinct episodes with characteristic, but locally variable, intrusive rocks have been recognized. The sequence of emplacement of these intrusions is as follows: diabase porphyry, quartz, monzonite porphyry, dacite porphyry, granodiorite and rhyolite porphyry. Fluids associated with the dacite porphyry were wholly responsible for the formation of skarns in the West Point formation. The skarns are zoned with garnet/clinopyroxene near the intrusion and magnetite adjacent to the limestone. The bulk of the skarns consists of a coarse grained garnet- clinopyroxene- magnetite- calcite assemblage. This assemblage constitute high grade skarn, having formed at temperature of approximately 500 C° ,and it has been subdivided into SK1 and SK2 types: SK1

consists of the magnetite-rich skarn and commonly consists of a magnetite-clinopyroxene assemblage. SK2 consists of a calc-silicate assemblage, namely andradite garnet-clinopyroxene (hedenbergite)- calcite and subordinate magnetite, actinolite and chlorite. All the samples investigated in this work are SK2 type.

In addition to the mineralization and skarn formation in the calcareous rocks of the West Point formation, the other sedimentary rocks in the immediate vicinity of the Sullipek deposit are affected by thermal metamorphism. The effects include recrystallisation of pure limestone to form marble and sandstone to form quartzite and the development of hornfels from calcareous siltstone.








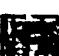

Figure 16, shows the horizontal section at the adit level. The location of each sample used in the present investigation is specified by circled numbers on the section and is given in table 5. The T series (T16, T24, T45, T50, T62) were collected from the tailings. Detailed informations of the samples are given in Appendix C.

1 of






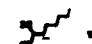

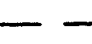




LITHOLOGY

- 
RHYOLITE PORPHYRY
 QRTZ, BFT, HBL, CILLS, PLAG-GRAN, GRANITE, SPHENITE, CHRYSOPTILE, BIRTITE, PHS AND ALKALI FICHERITE
- 
GRANODIORITE
 QRTZ, PLAG-GRAN, GRANITE, BIRITE TO PHS, MICROGRANITE, QUARTZDIAZONITE, BIRTITE
- 
QUARTZ DIORITE PORPHYRY
 QRTZ, BFT, GRAN-GRAN, PLAGIOLITE, SPHENITE, CHRYSOPTILE, BIRTITE, PHS
- 
QUARTZ STOCKWORK
 QRTZ, BFT, GRAN-GRAN, PLAGIOLITE, SPHENITE, CHRYSOPTILE, BIRTITE, PHS
- 
SKARN
 QRTZ, BFT, GRAN-GRAN, PLAGIOLITE, SPHENITE, CHRYSOPTILE, BIRTITE, PHS, AND ALKALI FICHERITE, AND ACCESSORY QUARTZ, BIRTITE, PHS AND ALKALI FICHERITE, AND ACCESSORY QUARTZ, BIRTITE, PHS AND ALKALI FICHERITE, AND ACCESSORY QUARTZ, BIRTITE, PHS AND ALKALI FICHERITE
- 
DACITE PORPHYRY
 QRTZ, BFT, GRAN-GRAN, PLAGIOLITE, SPHENITE, CHRYSOPTILE, BIRTITE, PHS, AND ALKALI FICHERITE, AND ACCESSORY QUARTZ, BIRTITE, PHS AND ALKALI FICHERITE
- 
QUARTZ MONZONITE PORPHYRY
 QRTZ, BFT, GRAN-GRAN, PLAGIOLITE, SPHENITE, CHRYSOPTILE, BIRTITE, PHS
- 
DIABASE PORPHYRY
 QRTZ, BFT, GRAN-GRAN, PLAGIOLITE, SPHENITE, CHRYSOPTILE, BIRTITE, PHS
- 
WEST POINT FORMATION
 QRTZ, BFT, GRAN-GRAN, PLAGIOLITE, SPHENITE, CHRYSOPTILE, BIRTITE, PHS, AND ALKALI FICHERITE, AND ACCESSORY QUARTZ, BIRTITE, PHS AND ALKALI FICHERITE

2 of 2

LEGEND

- 
 GEOLOGICAL CONTACT
 1) UNCONFORMITY 2) DISCONFORMITY 3) FAULT
- 
 FAULT
 1) NORMAL 2) REVERSE 3) THRUST
- 
 MAGNETIC FIELD AXIS, PLUMBAGE
- 
 WELL
 1) OPEN 2) ABANDONED
- 
 ROAD
 1) ASPHALT 2) GRAVEL 3) DIRT
- 
 US-31
- 
 CLEAR BOUNDARY
- 
 STRUCTURE

SULLIPEK DEPOSIT HORIZONTAL CROSSSECTION GEOLOGY

2070 LEVEL (ADIT)

McGILL UNIVERSITY / AMTHER-PRICE MIN. RES.
 SCALE 1:4850
 DATE: NOVEMBER, 1981
 DRAWN BY R. WALES GEOLOGY BY R. WALES

SECTION 24

Table 5. The location of the samples. Numbers in the parenthesis indicate the vertical position (feet) with respect to dit level.

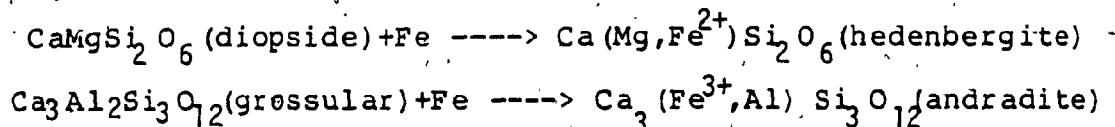
<u>Circled No.</u>	<u>Field No.</u>	<u>Distance</u>
1	S42 - 520	(-137)
2	S42 - 534	(-175)
3	SH - 14	(0)
	S24 - 558	(-139)
5	S24 - 793	(-374)
6	P3T - 455	(+ 8)
7	S38 - 251	(+131)
8	S104-200	(+372)
9	P72 - 254	(+334)

The samples T16, T24, T45, T50, and T62 were collected from the tailings.

CHAPTER VII

SAMPLES AND ABSORBERS PREPARATION

The samples consists mainly of a calcic-silicate assemblage, namely garnet-clinopyroxene-calcite-magnetite. The garnets and pyroxenes are mostly andradite ($\text{Ca}_3\text{Fe}_2\text{Si}_3\text{O}_{12}$), and hedenbergite $\text{Ca}(\text{Mg},\text{Fe}^{2+})\text{Si}_2\text{O}_6$, respectively, and were formed by iron metasomatism. Introduction of iron to diopside and grossular, the main constituent of the calcic-silicate zone formed hedenbergite and andradite as follows:



7.1. ABSORBERS PREPARATION

A careful study of the rocks was done both in hand specimen and thin section, in order to help identifying the minerals present and their proportions. (Descriptions are given in Appendix C). Each sample was crushed to a coarse grain for future separation of individual minerals. The garnets were easily separated from the pyroxenes, since they are porphyroblastic in texture (grain sizes = 2 to 5mm in diameter). The pyroxene is invariably intergrown with garnet and our main problem was to free the pyroxene.

Table 6. Alphabetical tables of the samples.

A	S24-793	H	SH14
B	S24-558	I	S104-200
C	S42-520	J	T-16
D	S42-534	K	T-24
E	P31-455	L	T-45
F	P72-254	M	T-50
G	S38-251	N	T-62

Effort was done to separate the pyroxene grains from the garnet by employing the methods such as magnetic and density separation techniques. Neither of these methods were successful because of the close magnetic susceptibilities and densities of garnet and pyroxene, and the small size of the grains of pyroxene. Thereafter, each sample was separated in two portions, one consisting of garnet, and the other a mixture of garnet and pyroxene. An assessment of the use of a mixture of garnet and pyroxene is given in chapter 8. The grains were then powdered and freed from magnetite by use a weak hand magnet and then freed from pyrite by using the magnetic separator (pyrite showed a weak presence in some of the samples). Each powder was examined under a polarizing microscope. The garnets showed the purity of 95 to 99 percent. In order to specify the percentage of pyroxene and garnet in the mixture, some portions were randomly chosen and counted under the polarizing microscope. The results are given in table.7 (chapter VIII) along with the other parameters obtained from

the spectra. Absorbers were then made by enclosing about 120(+3)mg of powder between two thin circular plastic disk of 2.2cm diameter. The thickness of absorbers was about 0.2mm.

For the sake of simplicity, the samples are specified by alphabetical letters as given in table 6.

CHAPTER VIII

RESULTS AND INTERPRETATION

The spectra of the absorbers obtained in 4 mm/sec velocity range are shown in figures 17 to 44 . As mentioned earlier, the garnets are mainly andradite with the chemical formula $\text{Ca}_3\text{Fe}_2\text{Si}_3\text{O}_{12}$, indicating the existence of iron at Fe^{3+} state. The spectra of the garnets except those of samples E and F in which Fe^{2+} peaks are present confirm this, and show the peak positions and the parameters which correspond to Fe^{3+} in octahedral position. These spectra also indicate to a good degree the purity of their structure with no detectable Fe^{2+} . Samples E and F, in which some portion of Ca^{2+} are probably replaced by Fe^{2+} in their structure, are not considered in our investigation of the antipathetic relation, because the Fe^{2+} peaks strongly overlap with the peaks resulting from the Fe^{2+} in hedenbergite.

The spectra of mixed (garnet and pyroxene) absorbers show well-defined, non-overlapping peaks from Fe^{3+} (22') and Fe^{2+} (11'). The Fe^{3+} (22') peaks are similar in all respects to those obtained from andradite absorbers and are therefore assigned to Fe^{3+} in andradite of the mixed absorbers. In view of the fact that andradite absorbers used in this work did not yield detectable Fe^{2+} peaks, the peaks (Fe^{2+}) in the mixed spectra were assigned entirely to Fe^{2+} in the pyroxene (hedenbergite).

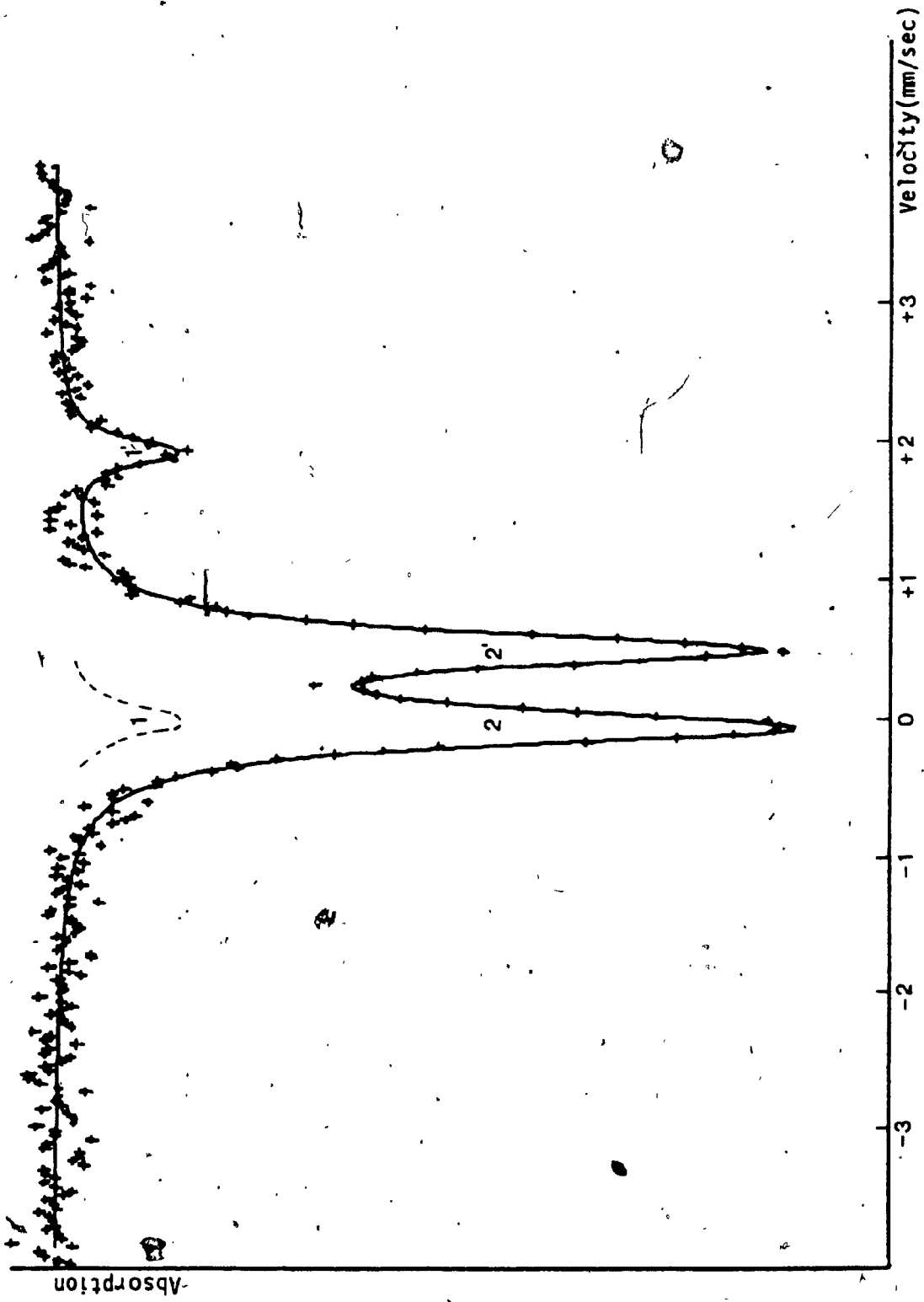


Fig. 17. Computer plot of the Mössbauer spectra of sample A (S24-793 Pyroxene and Garnet)

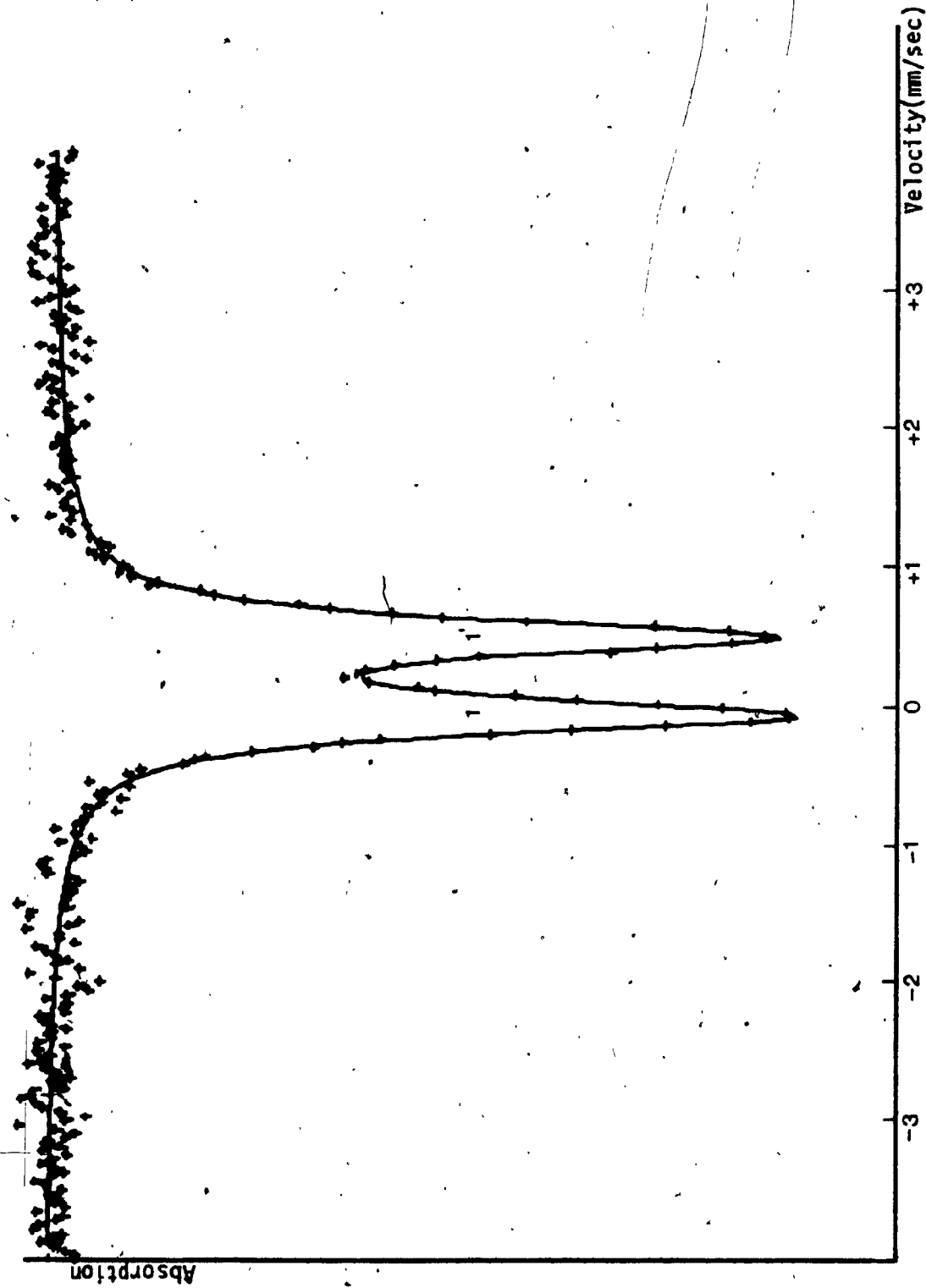


Fig. 18. Computer plot of the Mössbauer spectra of sample A(S24-793 Garnet)

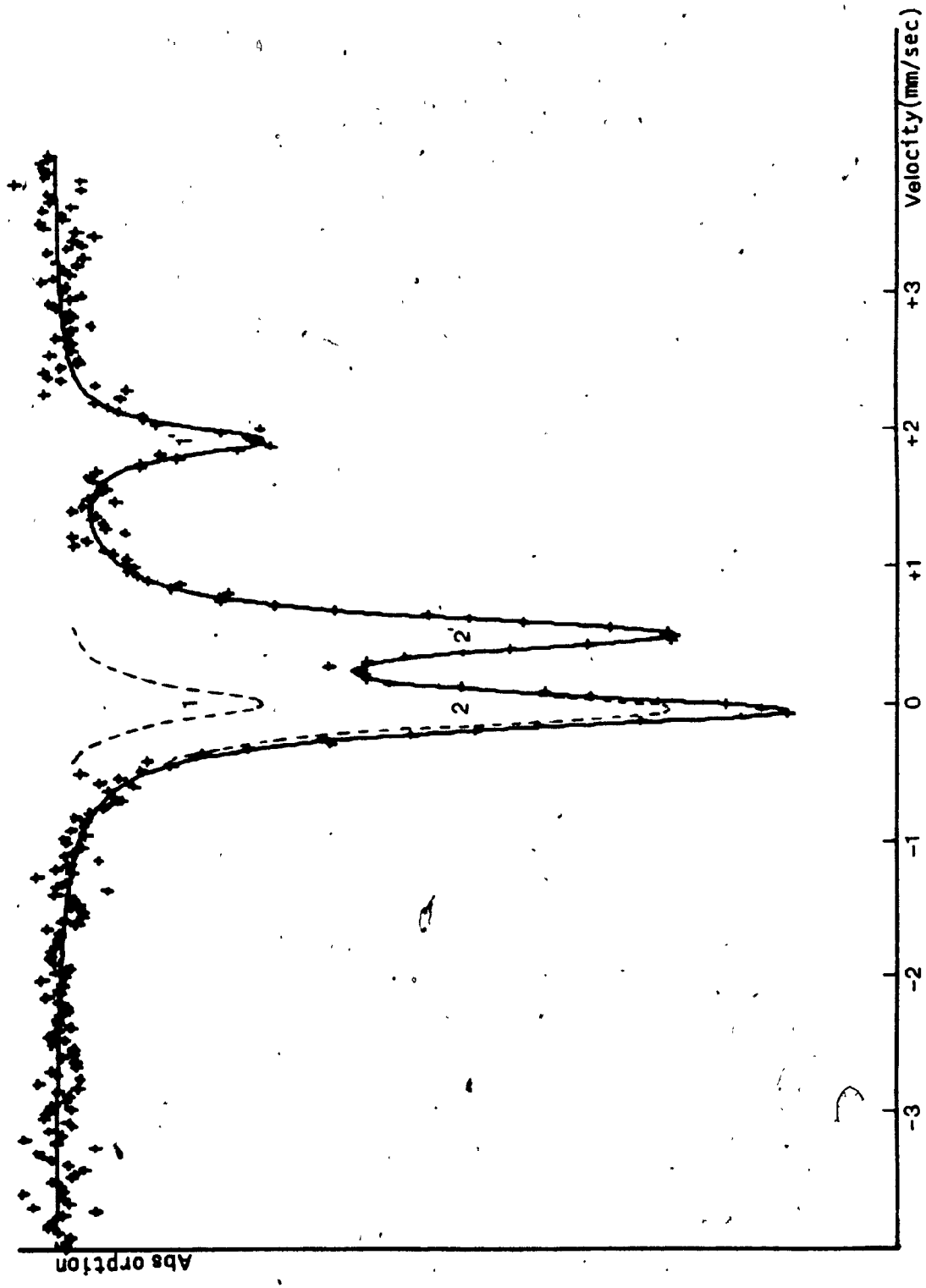


Fig. 19. Computer plot of the Mossbauer spectra of sample B(S24-558 Pyroxene and Garnet)

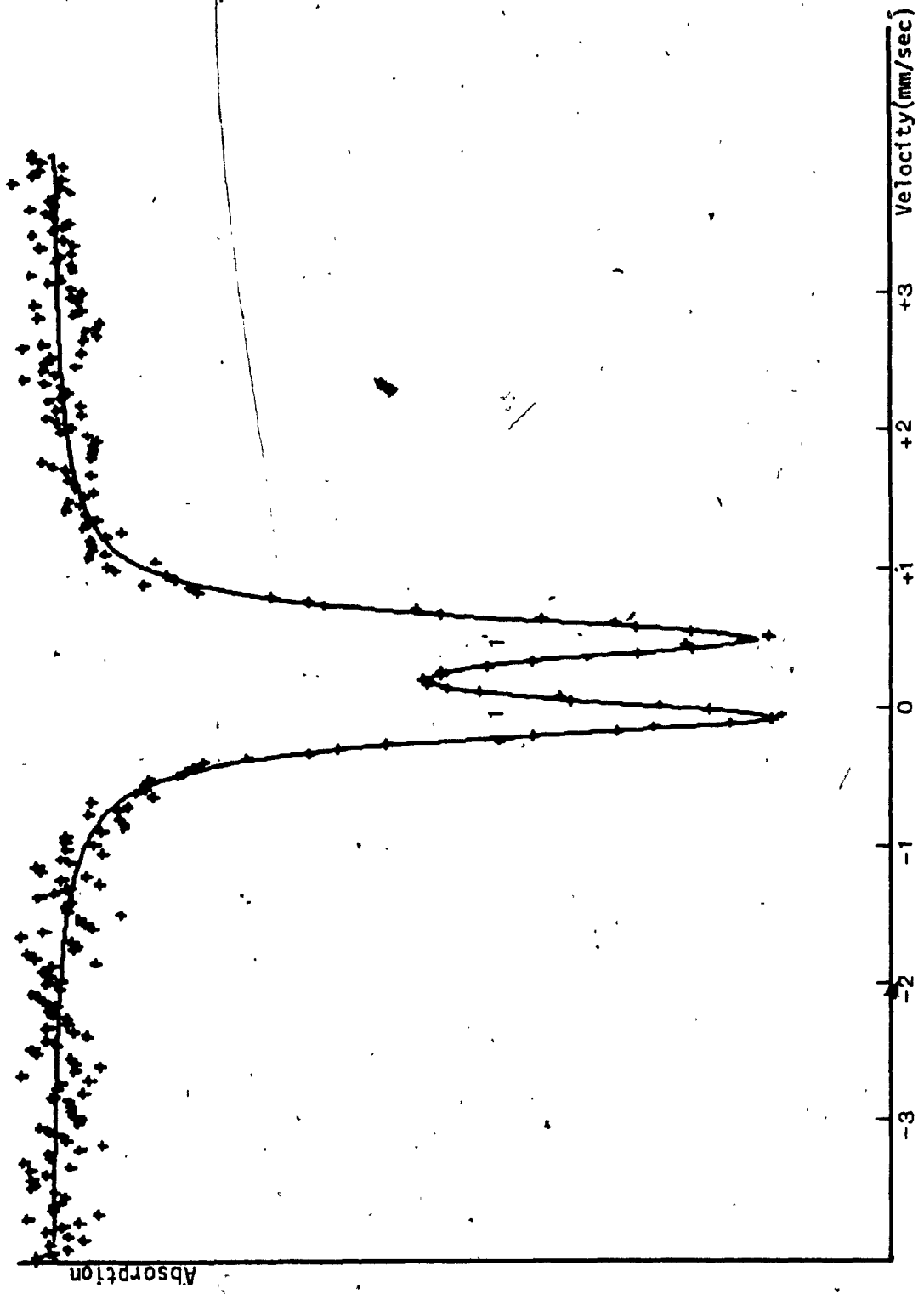


Fig. 20. Computer plot of the Mössbauer spectra of sample B(S24-558 Garnet)

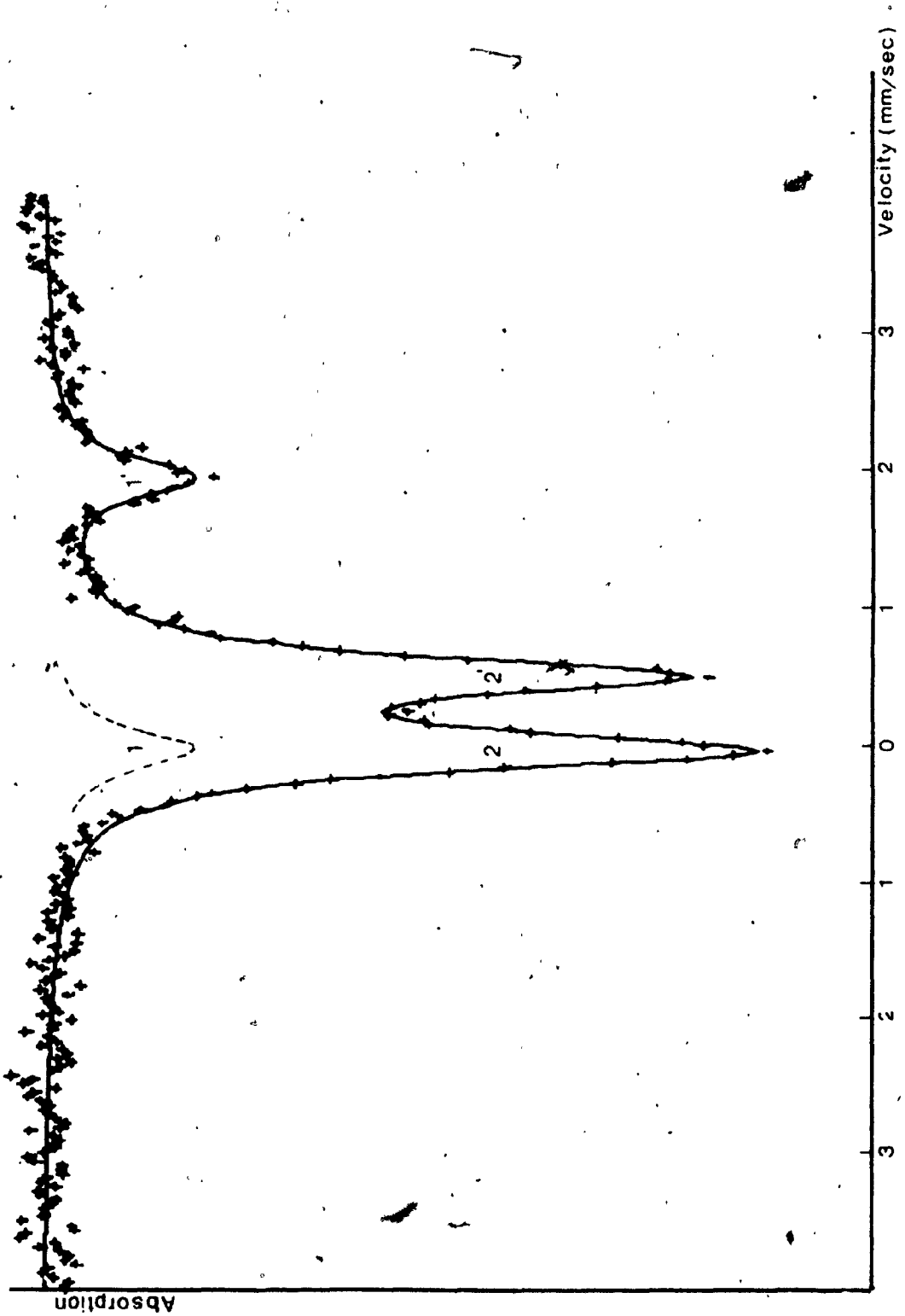


Fig.21. Computer plot of the Mössbauer spectra of sample C(S42-520 Pyroxene and Garnet)

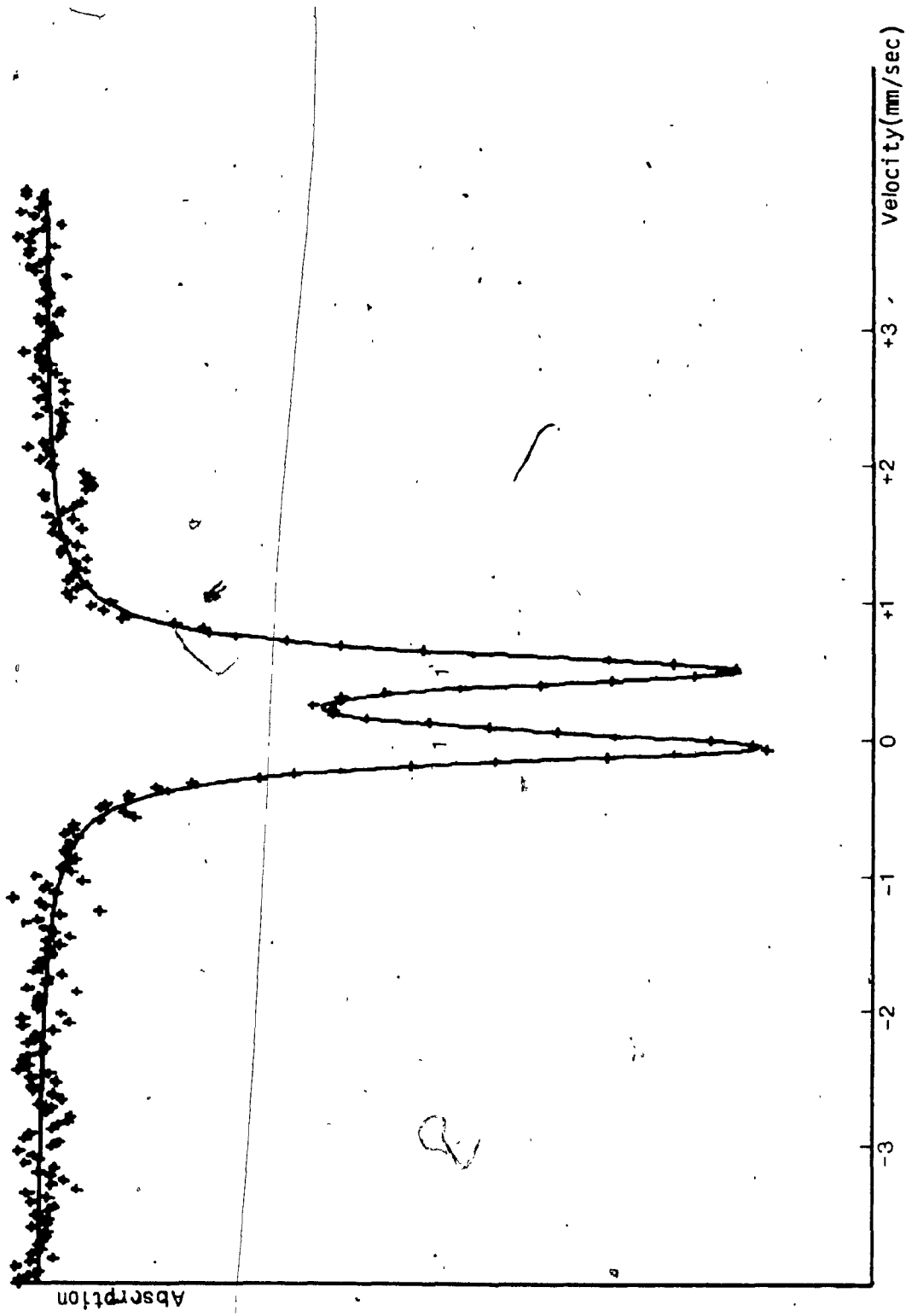


Fig.22 . Computer plot of the Mössbauer spectra of sample C(S42-520 Garnet)

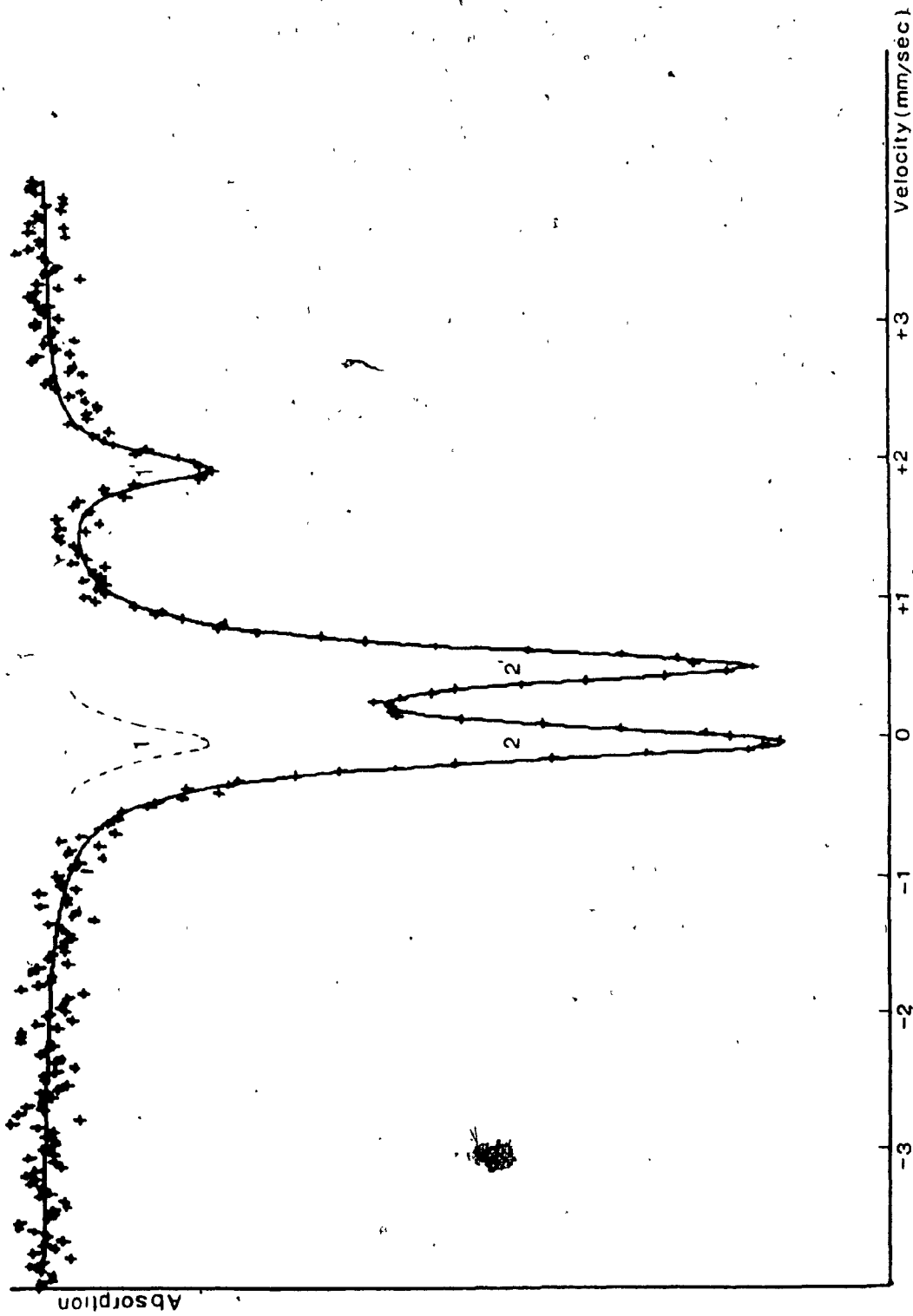


Fig. 23. Computer plot of the Mossbauer spectra of sample D(S42-534 Pyroxene and Garnet)

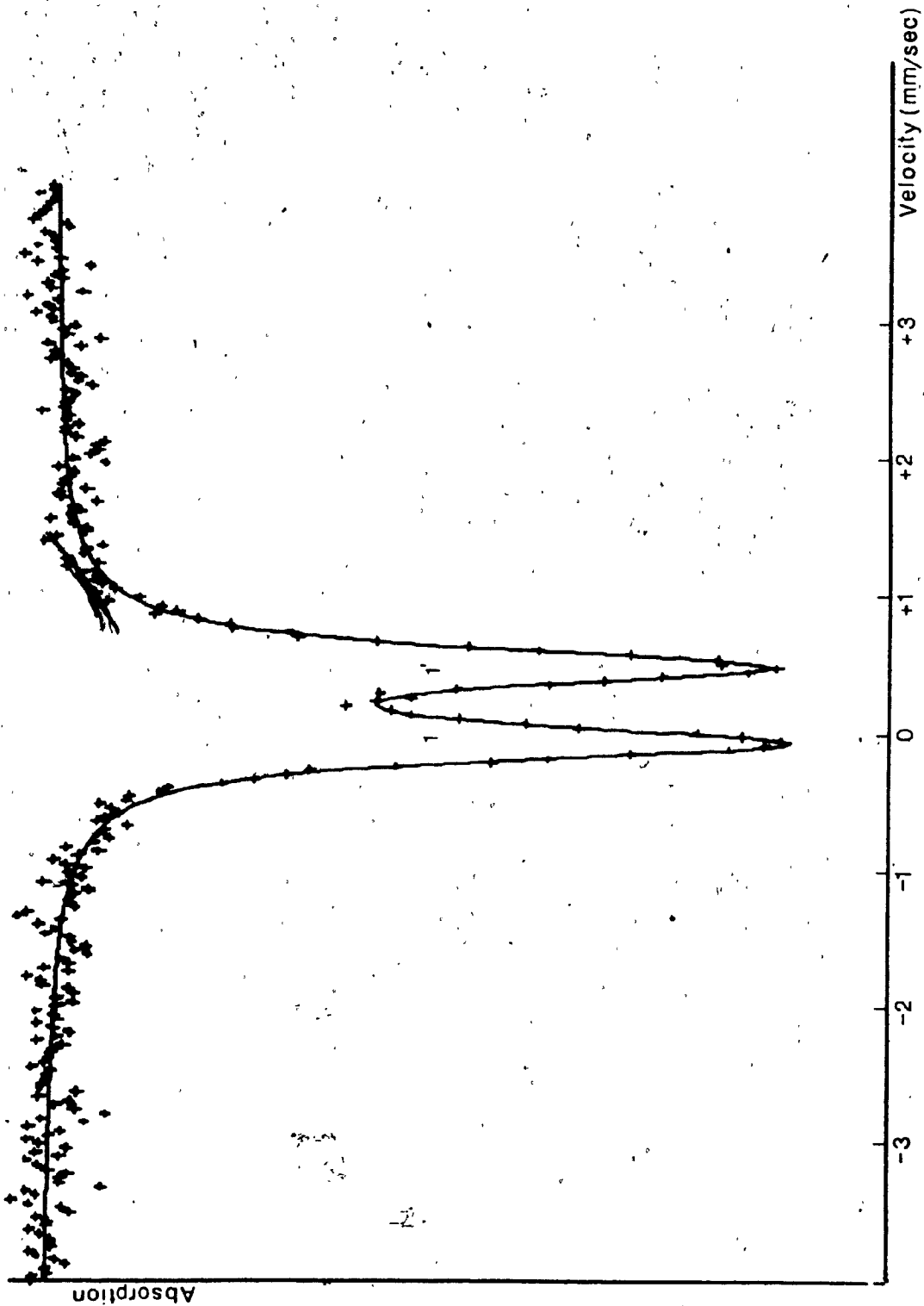


Fig. 24. Computer plot of the Mössbauer spectra of sample D(S42-534 Garnet)

S

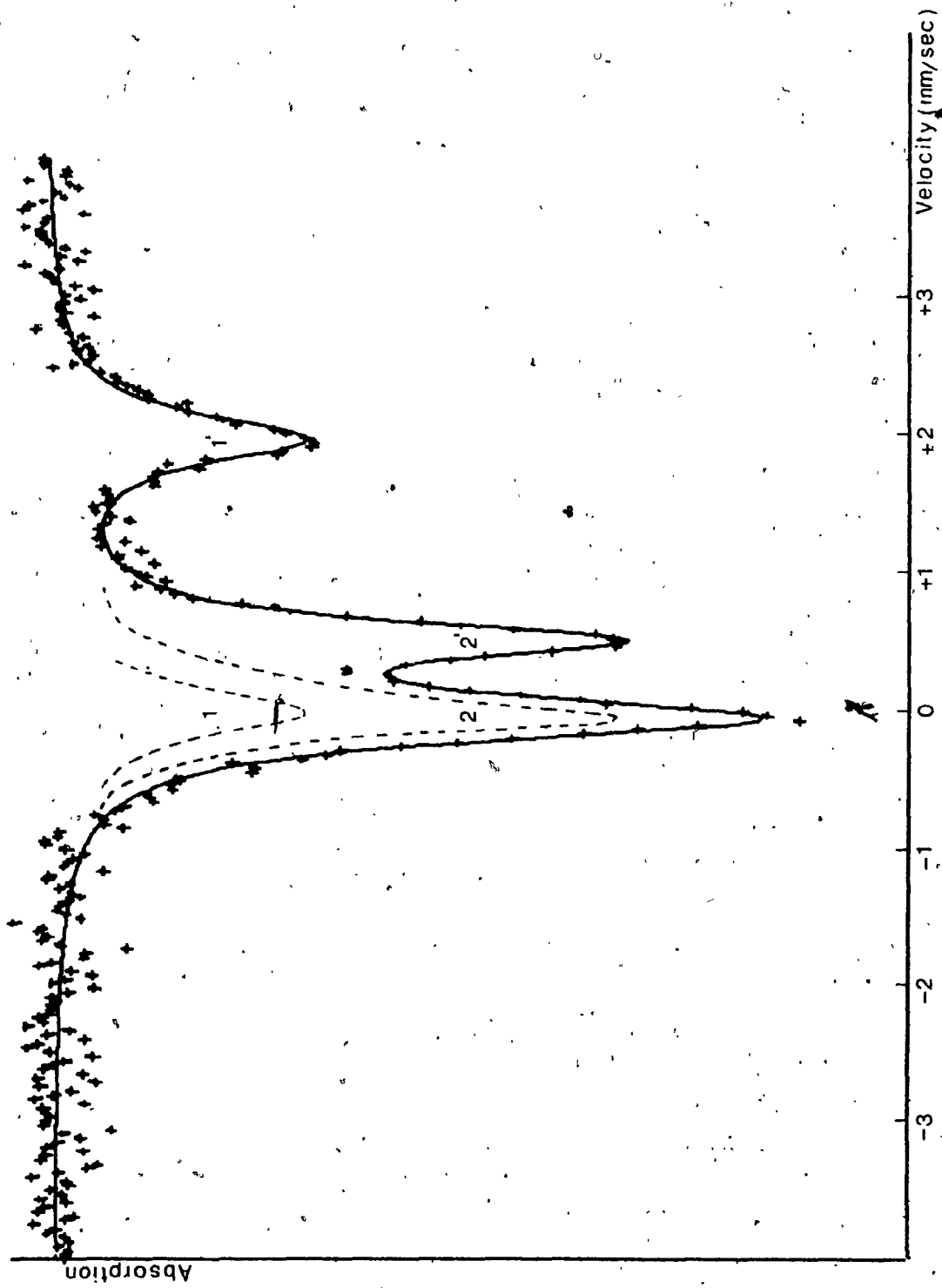


Fig. 25. Computer plot of the Mössbauer spectra of Sample E(P31-455 Pyroxene and Garnet)

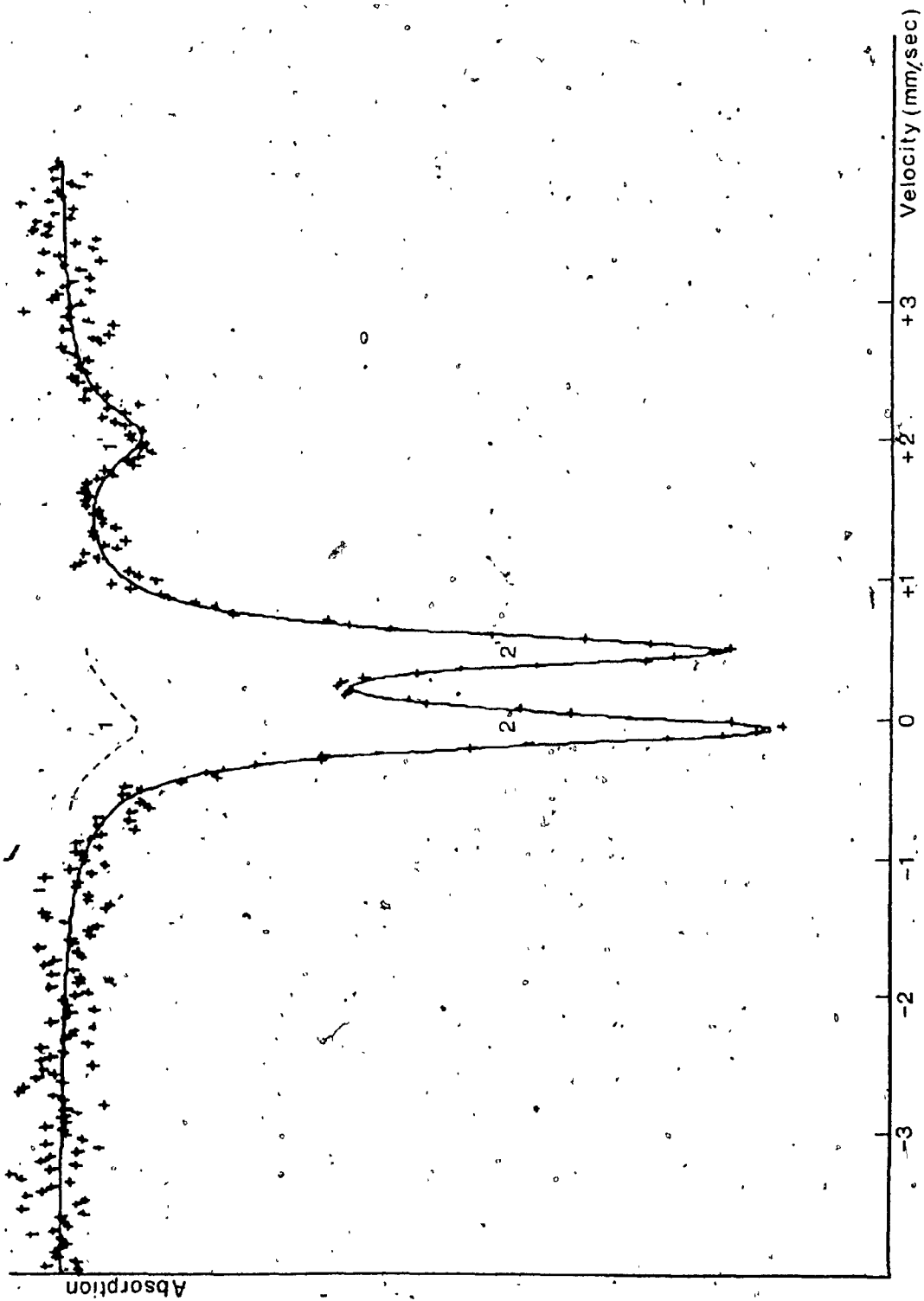


Fig.26. Computer plot of the Mössbauer spectra of sample E (P31-455 Garnet)

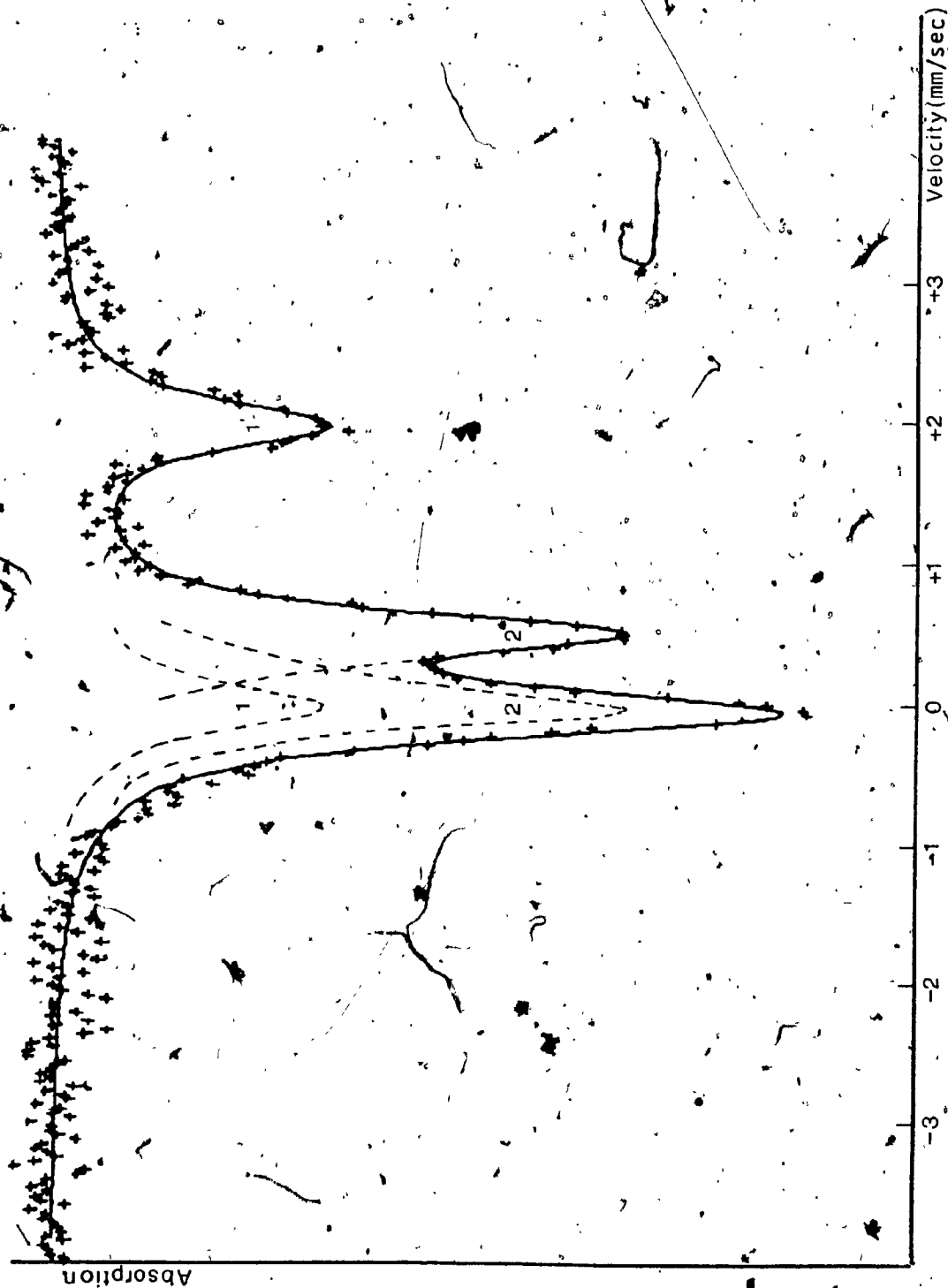


Fig. 29. Computer plot of the Mössbauer spectra of sample F(P72-254 Pyroxene and Garnet)

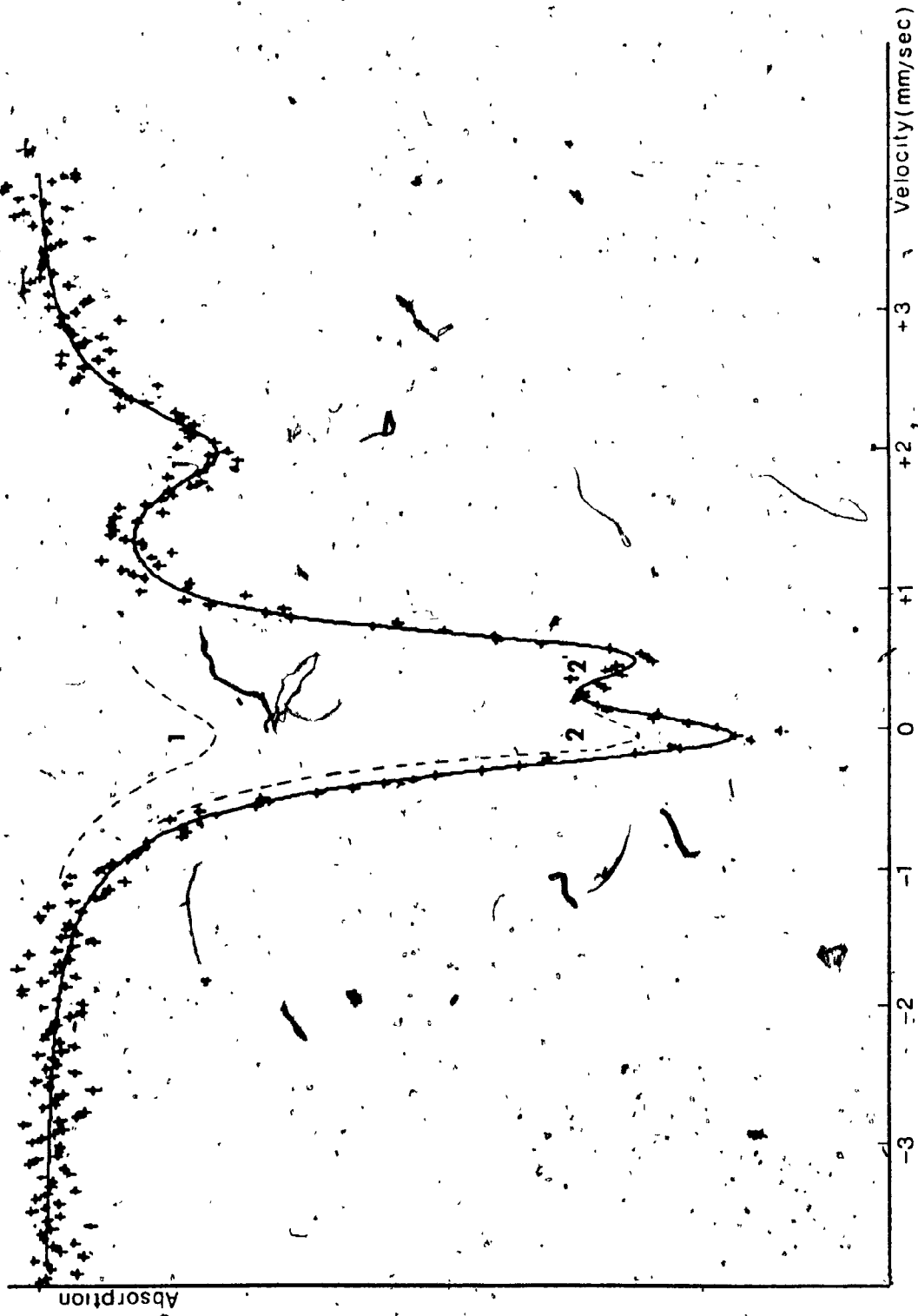


Fig. 28. Computer plot of the Mössbauer spectra of sample F(P72-254 Garnet)

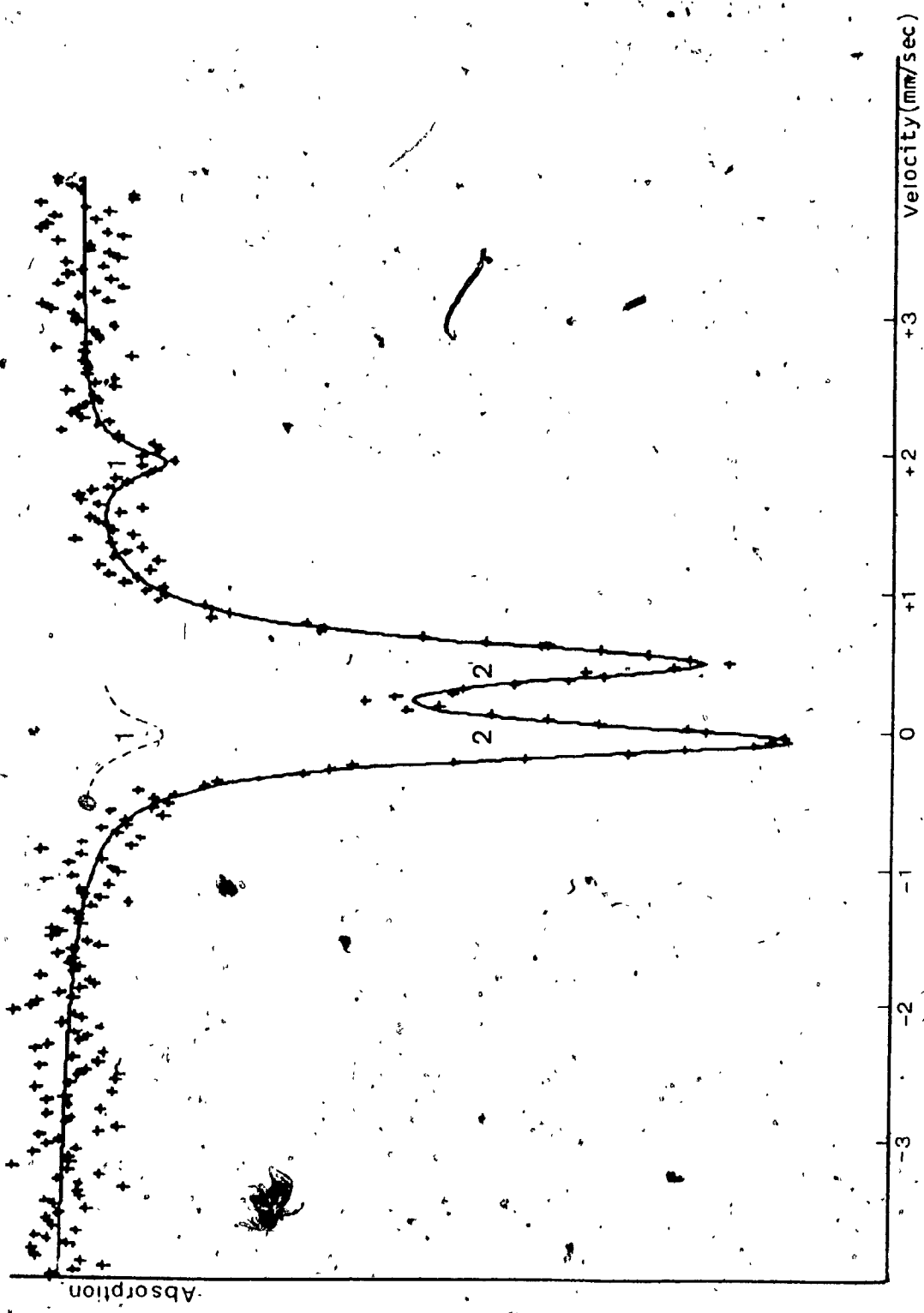


Fig. 29. Computer plot of the Mössbauer spectra of sample G(S38-251) Pyroxene and Garnet

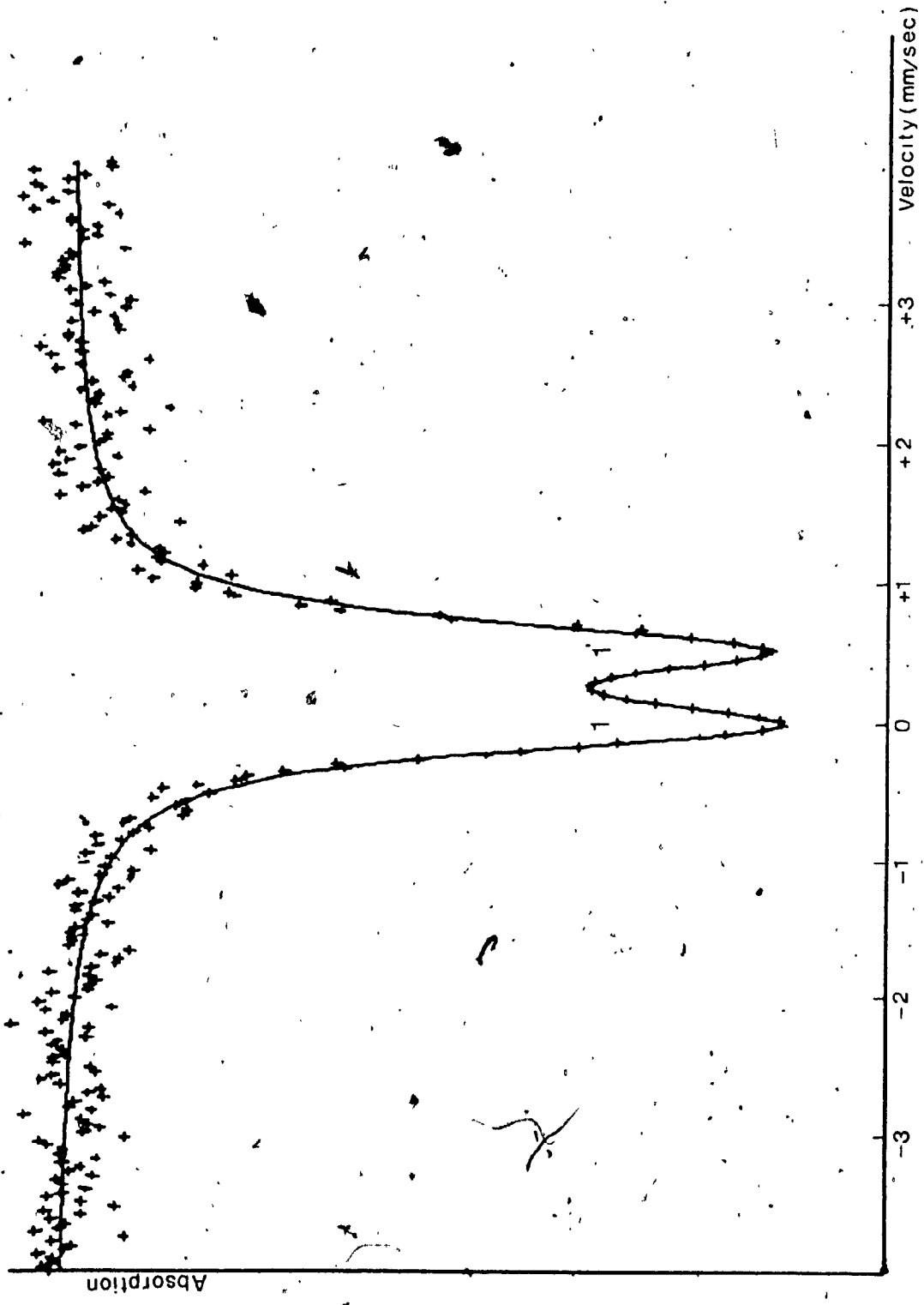


Fig. 30. Computer plot of the Mössbauer spectra of sample G(S38-251 Garnet)

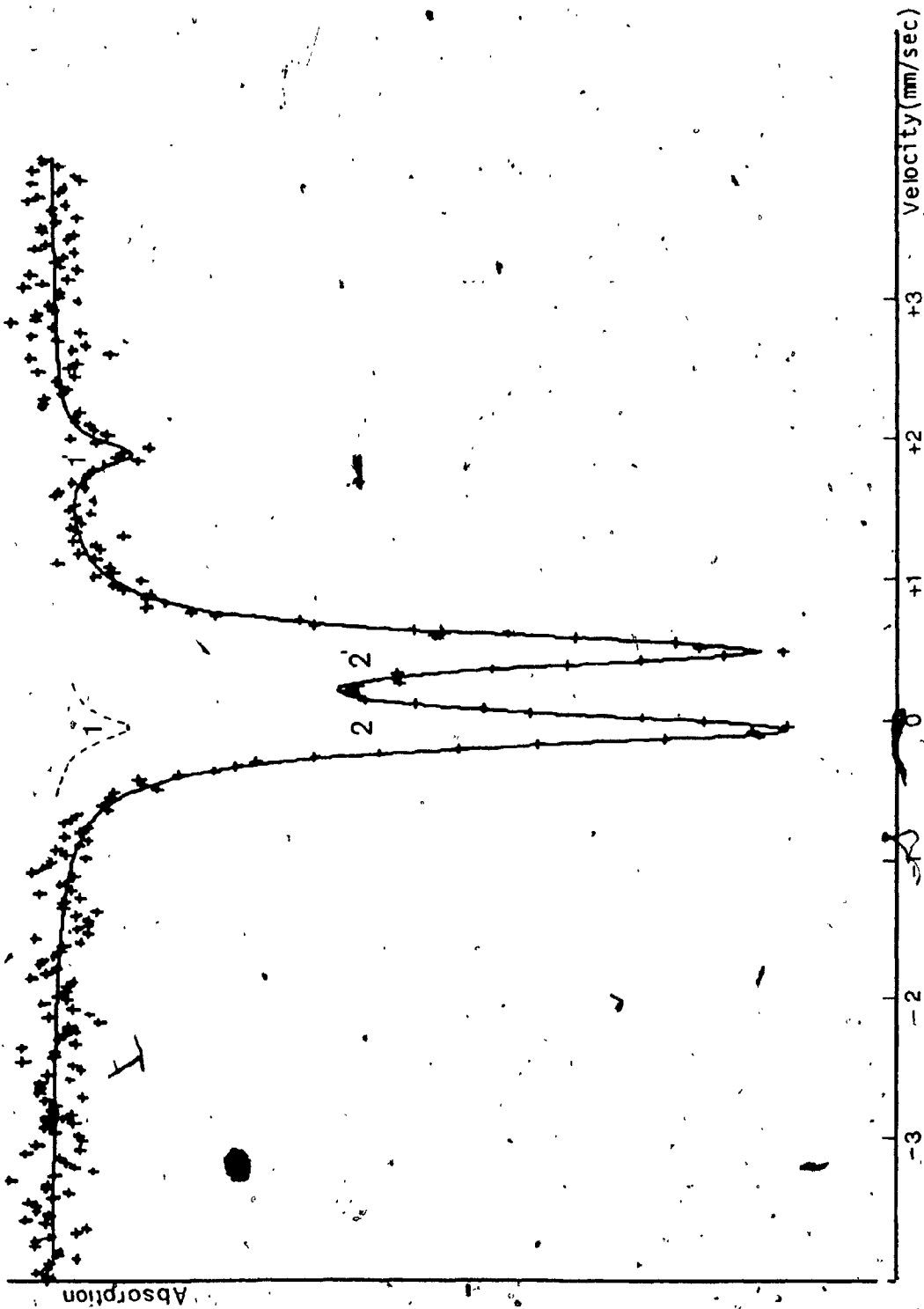


Fig. 31. Computer plot of the Mössbauer spectra of sample H(SH14 Pyroxene and Garnet)

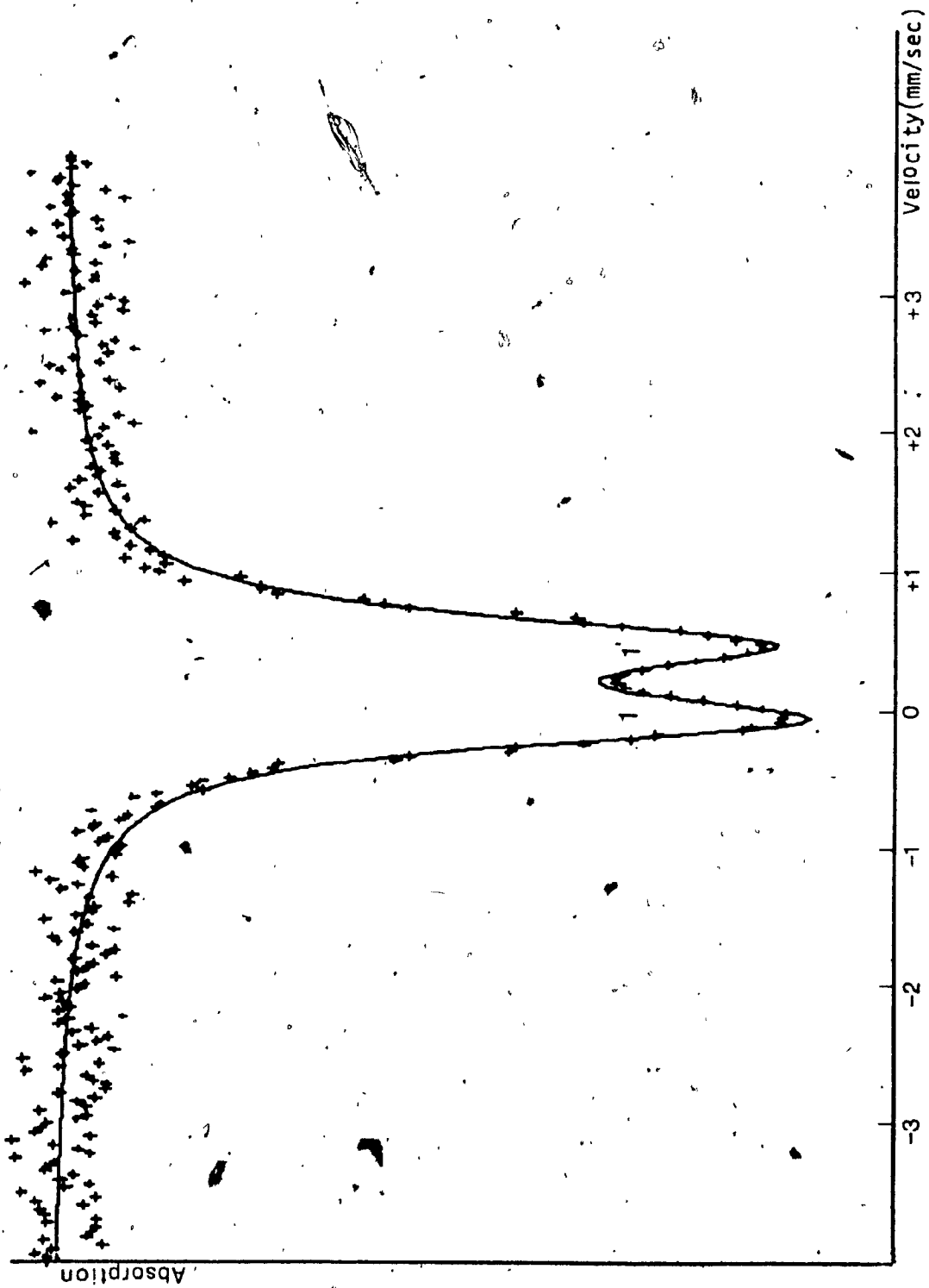


Fig. 32. Computer plot of the Mössbauer spectra of sample H(SH14) Garnet)

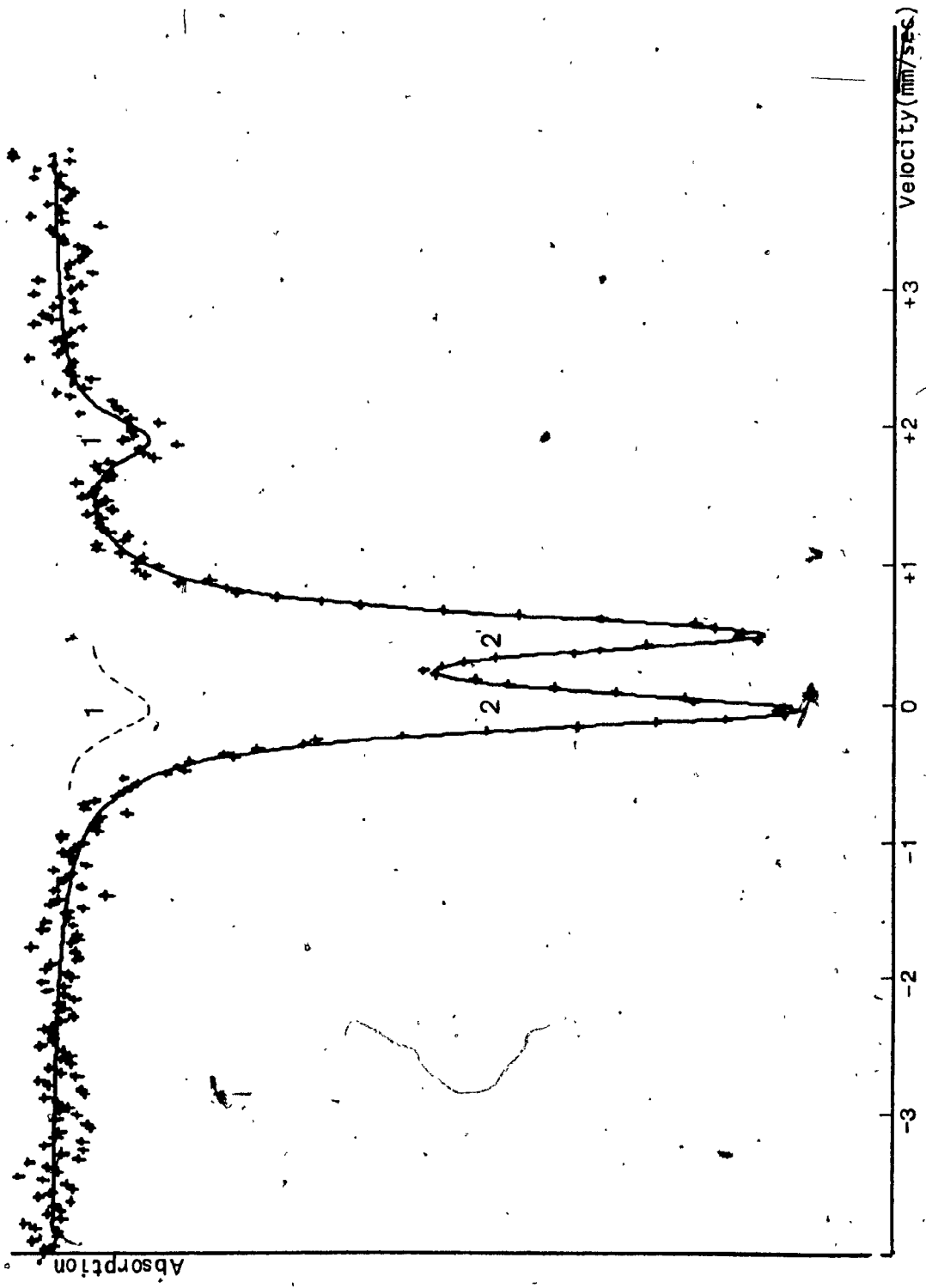


Fig. 33. Computer plot of the Mössbauer spectra of sample I (S104-200 Pyroxene and Garnet)

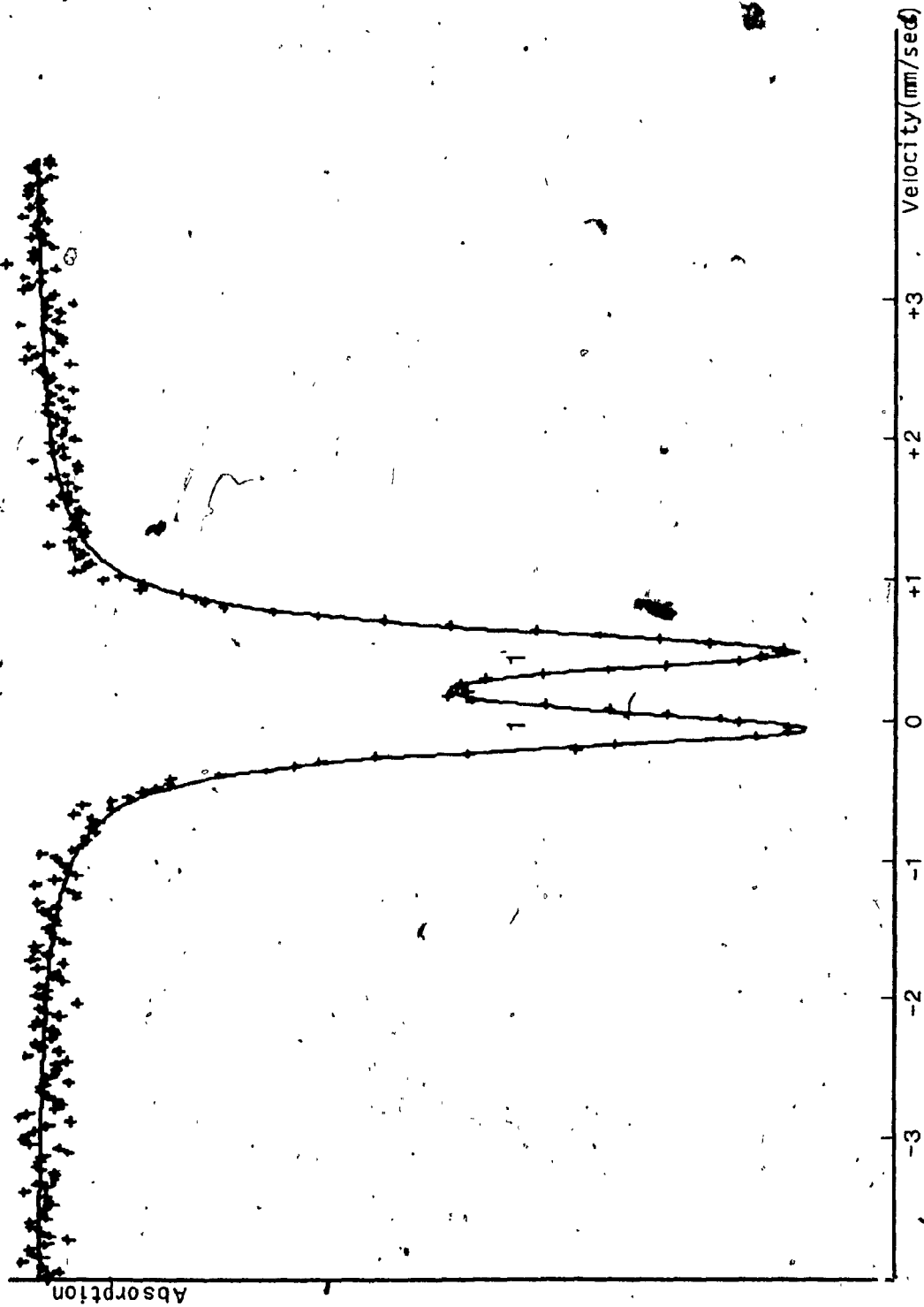


Fig. 34. Computer plot of the Mössbauer spectra of sample I (SiO₄-200 Garnet)

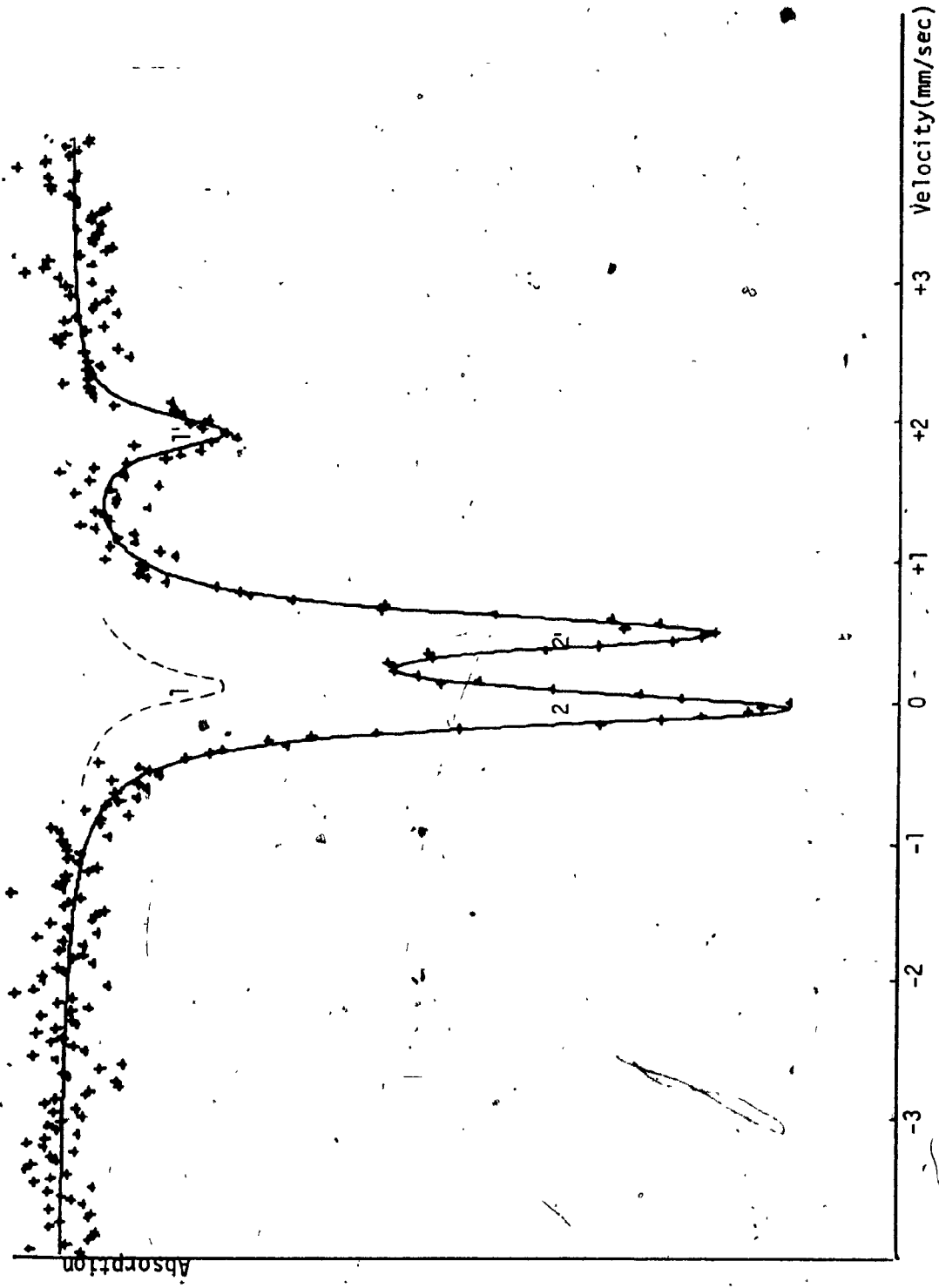


Fig. 35. Computer plot of the Mössbauer spectra of sample J(T16 Pyroxene and Garnet)

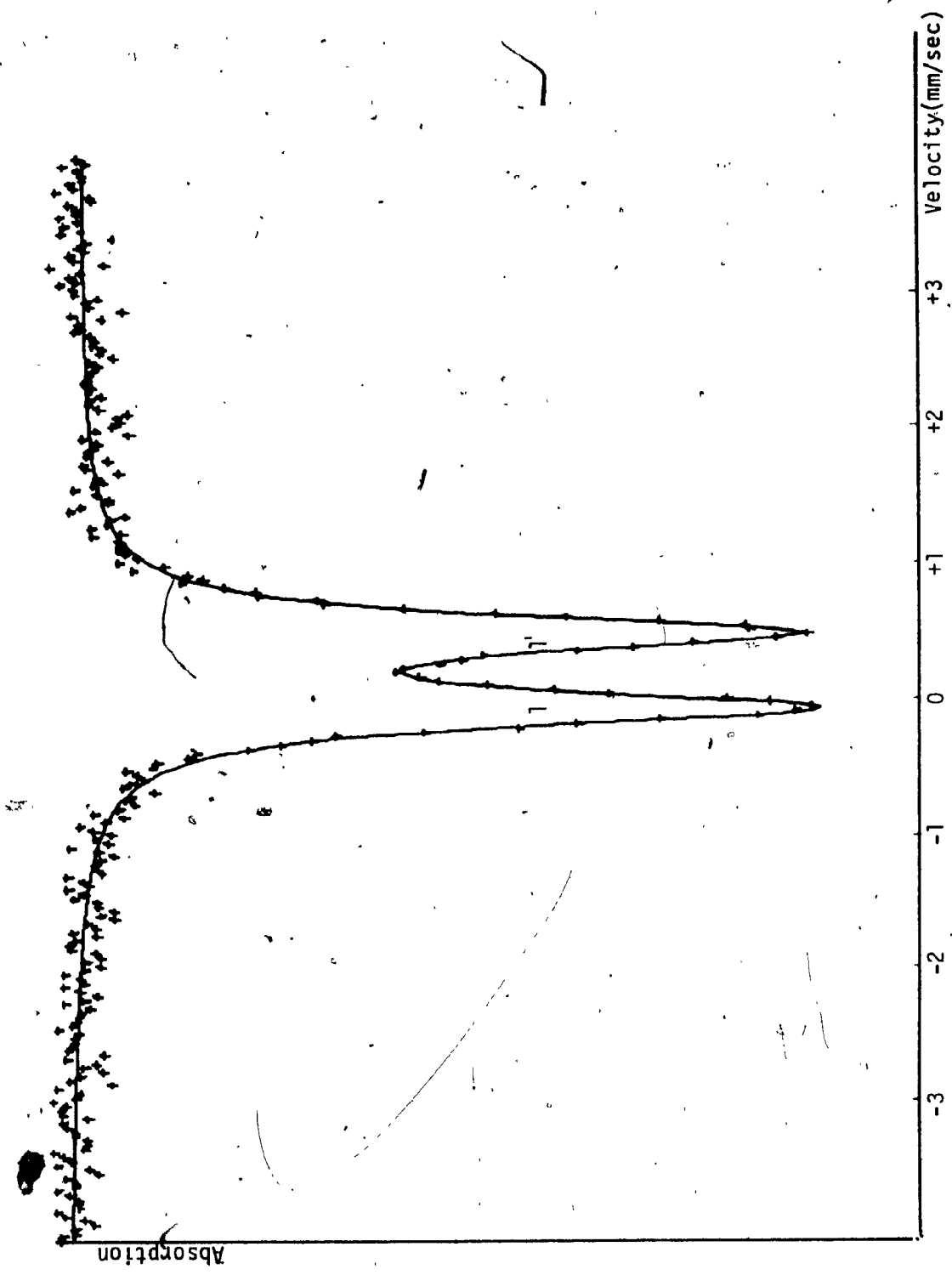


Fig. 36. Computer plot of the Mössbauer spectra of sample J(T16 Garnet)

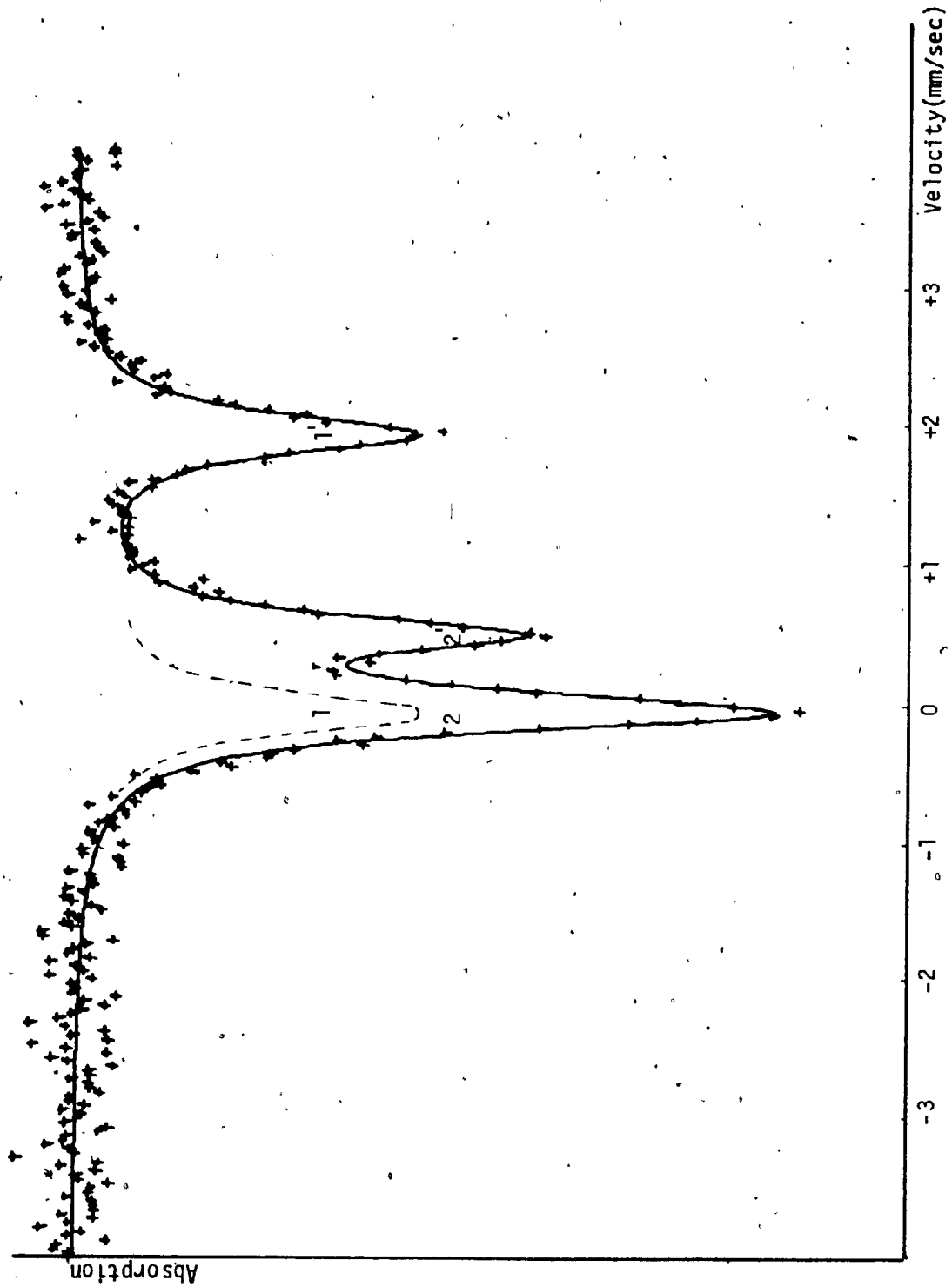


Fig.37. Computer plot of the Mössbauer spectra of sample K(T24 Pyroxene and Garnet)

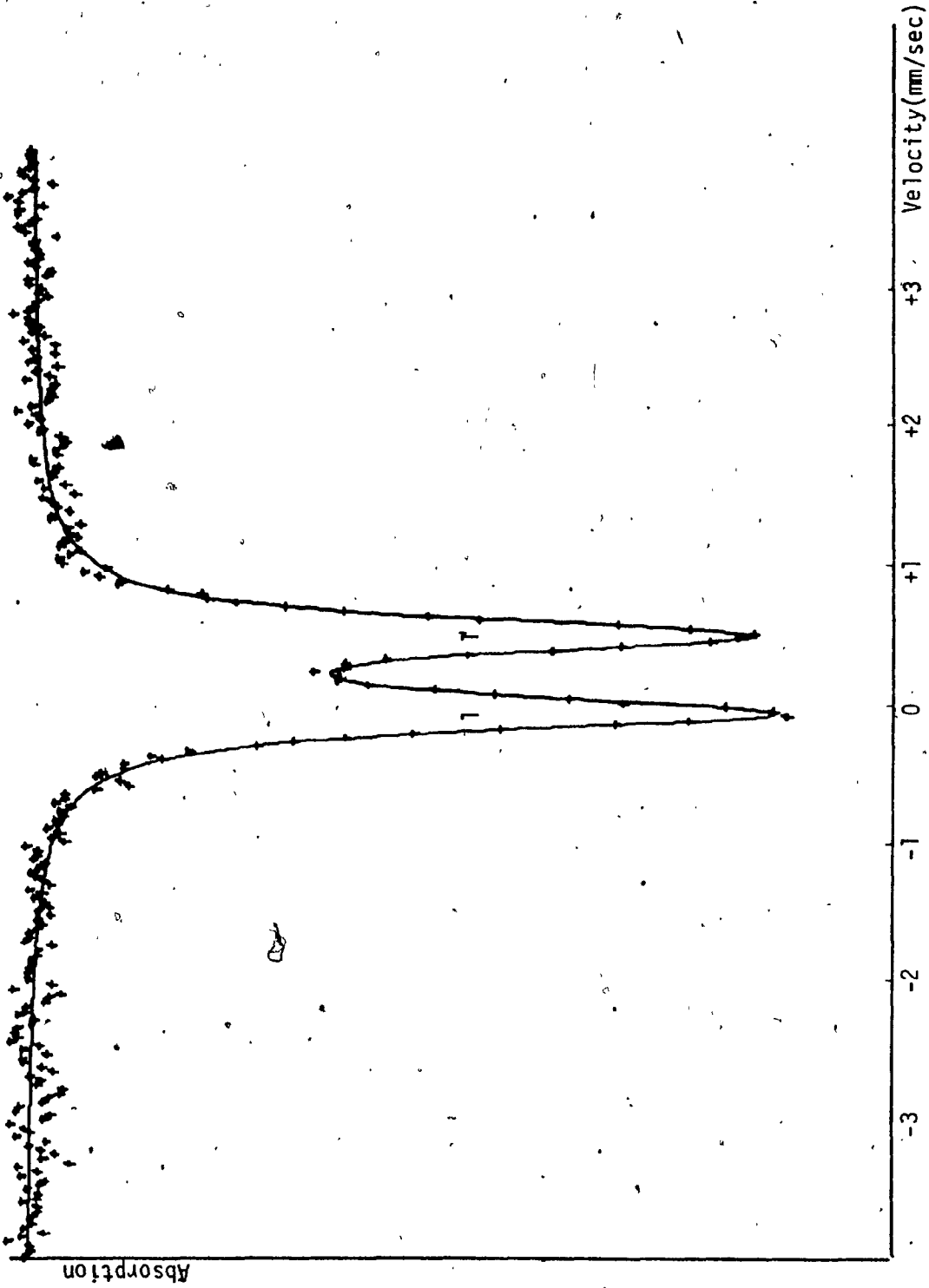


Fig. 38. Computer plot of the Mössbauer spectra of sample K(T24 Garnet)

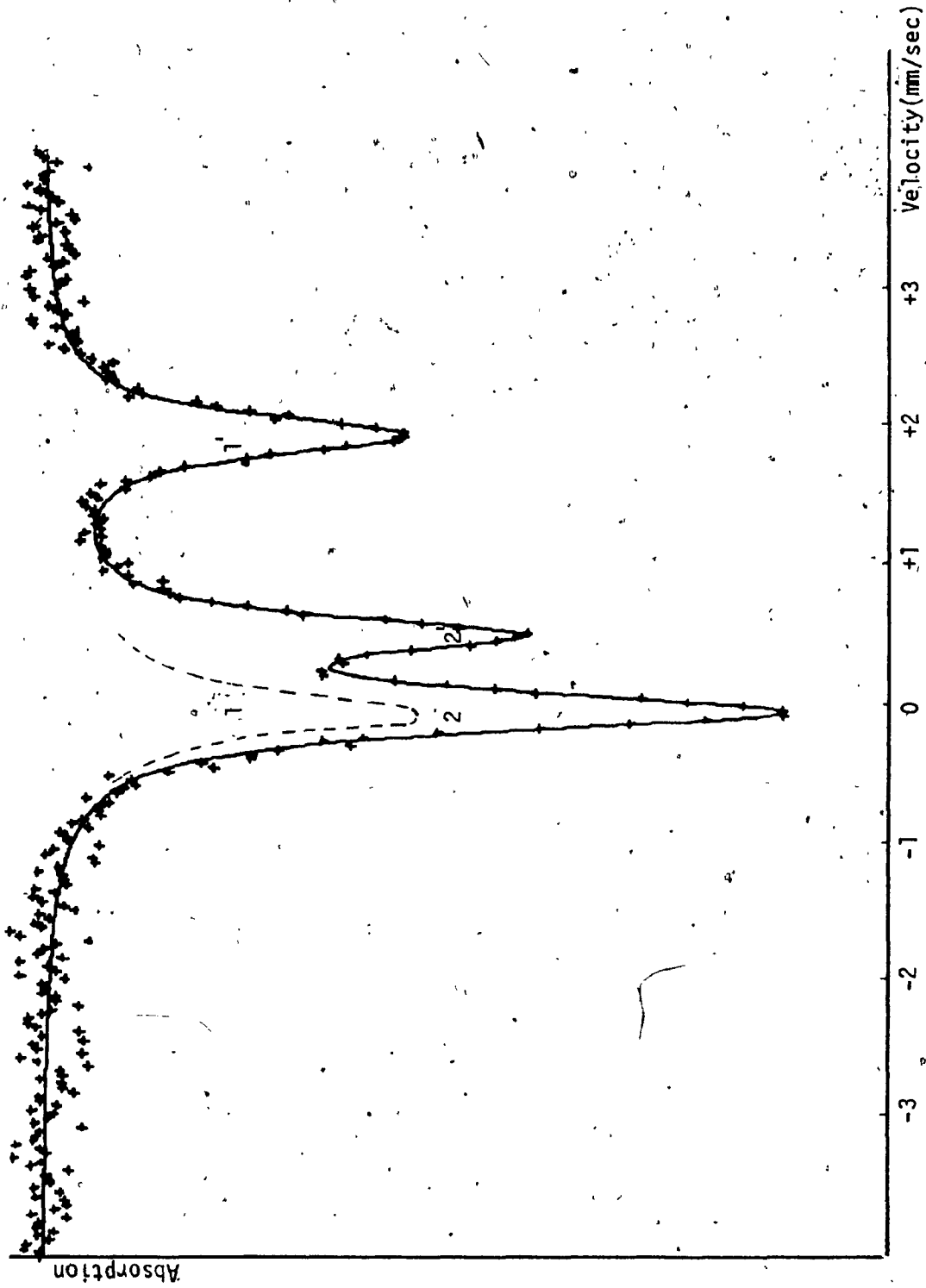


Fig. 39. Computer plot of the Mössbauer spectra of sample 4 (T45 Pyroxene and Garnet)



Fig. 40. Computer plot of the Mössbauer spectra of sample L(T45 Garnet)

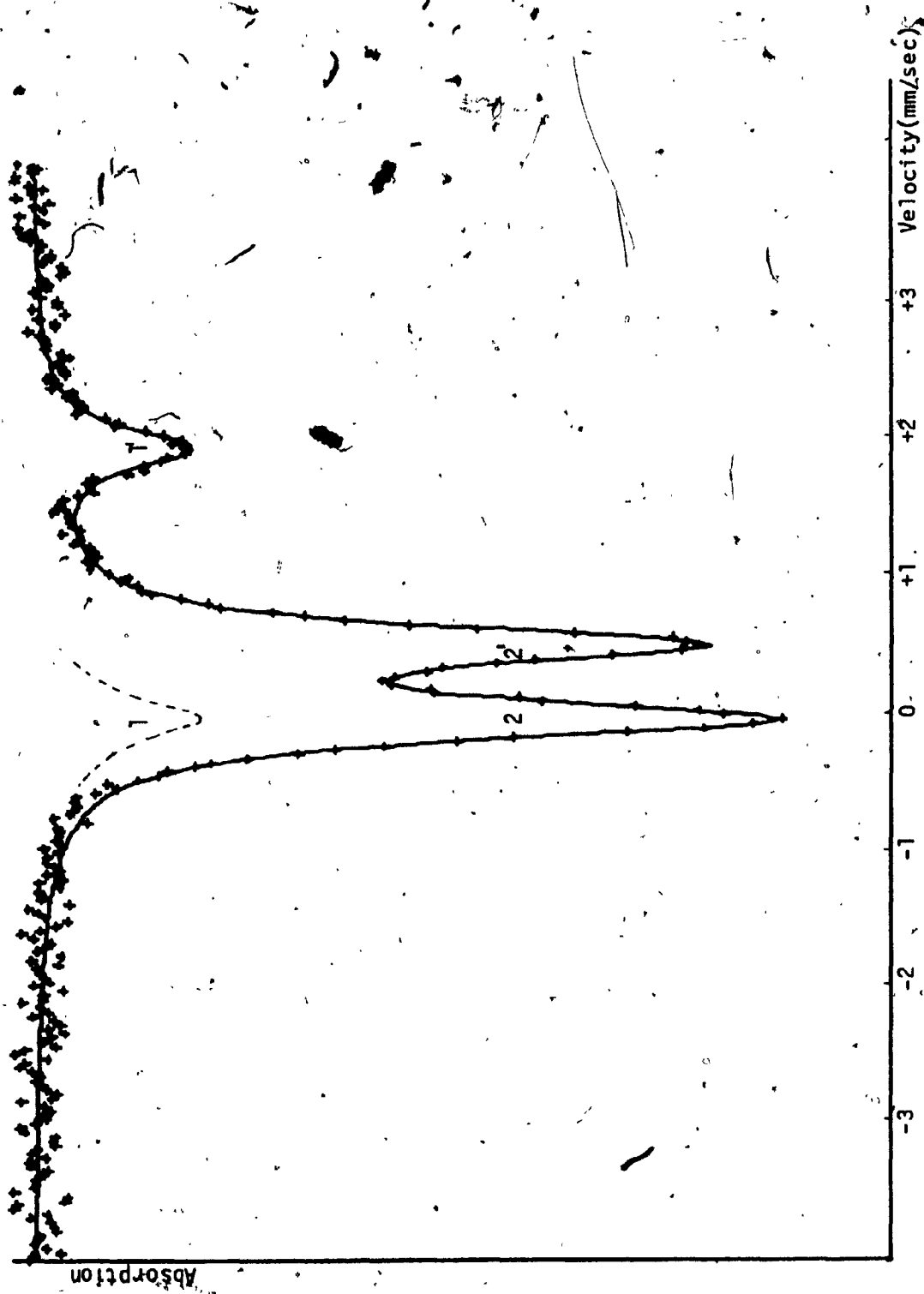


Fig. 41. Computer plot of the Mössbauer spectra of sample M(T50 Pyroxene and Garnet)

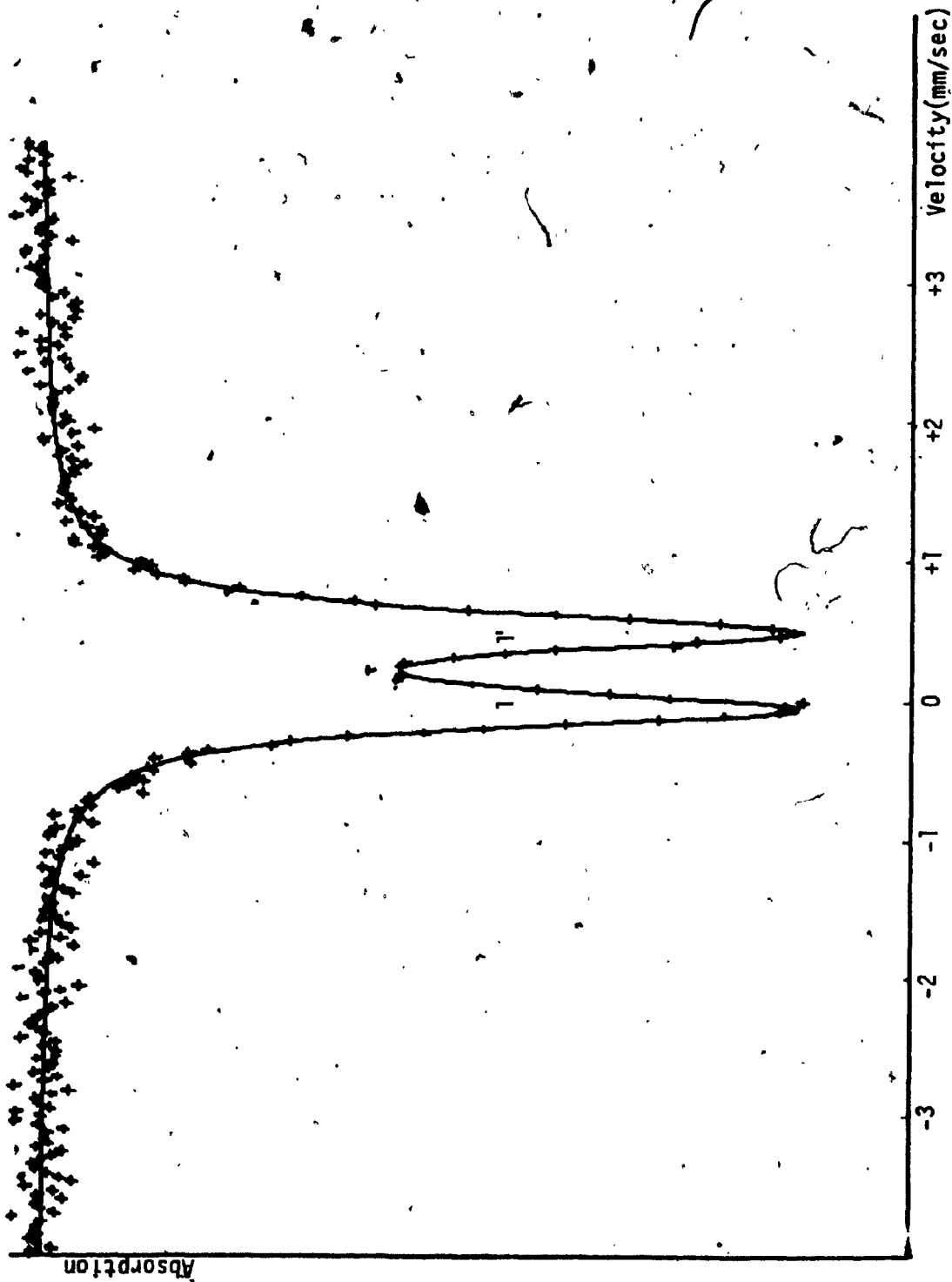


Fig.42. Computer plot of the Mössbauer spectra of sample M(T50 Garnet)

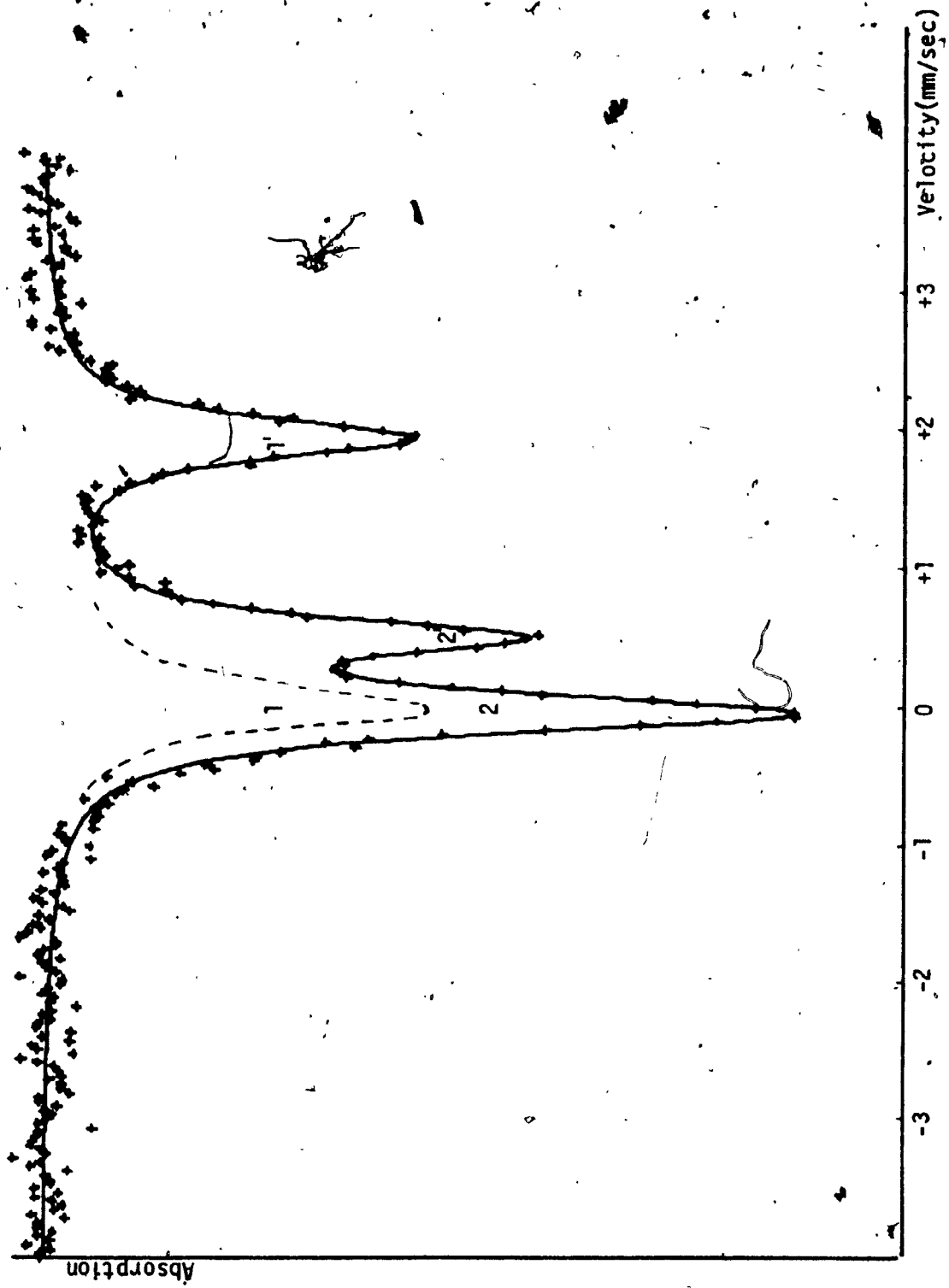


Fig. 43. Computer plot of the Mössbauer spectra of sample N(T62 Pyroxene and Garnet)

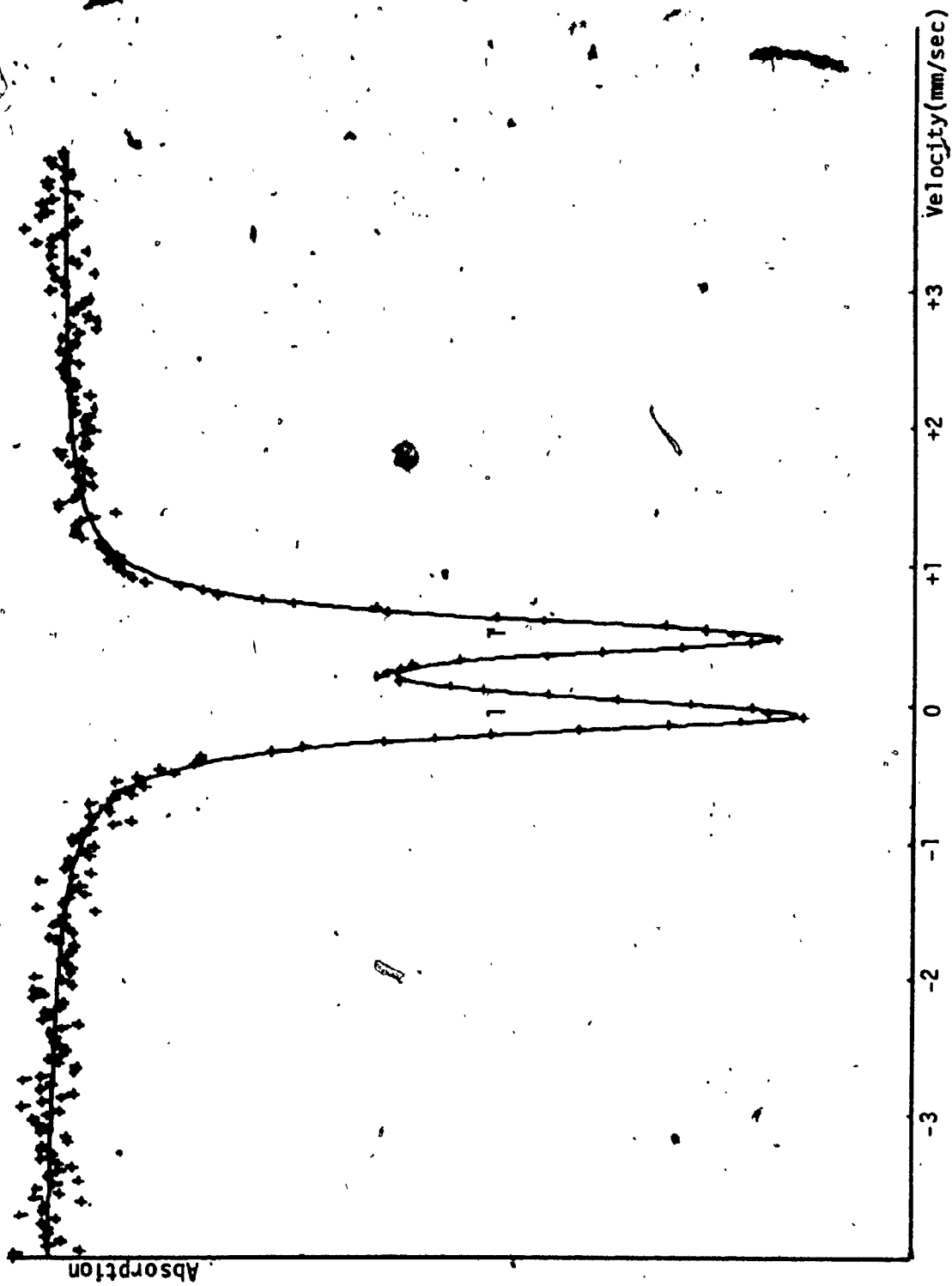


Fig. 44. Computer plot of the Mössbauer spectra of sample N(T62 Garnet)

Table 7. Calculated parameters of the samples (garnet/pyroxene, garnet) from Sullipek deposit Gaspé, Quebec. Included are the initial percentage of pyroxene and garnet in the mixed absorbers.

Samp.	Abs.	X ²	0.3(11'')	0.3(22'')	1.3(11'')	1.3(22'')	T _{1,1'}	T _{2,2'}	Fe ²⁺ /Fe ³⁺	Fe ³⁺ /Fe ²⁺	Initials Pyr.	Ger.
A	Mix.	280	1.97	.56	1.38	.63	.24	.28	12.4	87.6	60	40
	Ger.	237	.57	---	.64	---	.30	---	---	100		
B	Mix.	237	1.96	.56	1.34	.64	.26	.30	23	77	85	15
	Ger.	295	.57	---	.63	---	.35	---	---	100		
C	Mix.	270	1.98	.55	1.34	.64	.34	.32	20	80	78	22
	Ger.	292	.56	---	.64	---	.28	---	---	100		
D	Mix.	249	1.98	.55	1.36	.64	.28	.32	18	82	75	25
	Ger.	285	.56	---	.64	---	.30	---	---	100		
E	Mix.	250	2.0	.57	1.36	.64	.42	.31	40	60	60	40
	Ger.	240	2.0	.56	1.40	.64	.51	.29	18	82		
F	Mix.	265	2.0	.57	1.37	.64	.42	.33	40	60	85	15
	Ger.	298	2.1	.58	1.4	.65	.54	.44	28	72		
G	Mix.	231	1.99	.57	1.34	.63	.27	.37	9.0	91	80	20
	Ger.	242	.55	---	.64	---	.47	---	---	100		
H	Mix.	224	1.95	.56	1.33	.63	.23	.29	8.0	92	75	25
	Ger.	272	.55	---	.63	---	.47	---	---	100		
I	Mix.	255	1.95	.55	1.35	.65	.39	.37	12	88	65	35
	Ger.	295	.56	---	.63	---	.36	---	---	100		
J	Mix.	283	1.95	.54	1.34	.63	.32	.31	20	80	45	55
	Ger.	257	.56	---	.63	---	.29	---	---	100		
K	Mix.	312	1.98	.56	1.36	.64	.34	.30	50	50	75	25
	Ger.	283	.56	---	.64	---	.29	---	---	100		
L	Mix.	272	1.97	.55	1.36	.64	.32	.31	49	51	73	27
	Ger.	285	.56	---	.64	---	.30	---	---	100		
M	Mix.	295	1.95	.55	1.36	.64	.33	.30	18	82	43	57
	Ger.	273	.55	---	.63	---	.31	---	---	100		
N	Mix.	243	1.92	.55	1.35	.64	.34	.32	49	51	70	30
	Ger.	295	.56	---	.64	---	.31	---	---	100		

Table 8. Numerical designations of iron content (Fe^{2+} and Fe^{3+}), in the mixed spectra.

Samp.	I A11'/B.G	II A22'/B.G	III(Fe^{2+}) (A11'/B.G)(50%/Init.%)	IV(Fe^{3+}) (A22'/B.G)(50%/Init.%)
A	.41(2)	2.89(1)	.34(2)	3.61(3)
B	.69(1)	1.69(1)	.40(2)	5.63(3)
C	.75(2)	2.48(2)	.48(1)	5.64(2)
D	.68(2)	2.63(1)	.45(3)	5.26(3)
G	.18(2)	1.88(2)	.11(3)	4.71(4)
H	.16(2)	1.80(2)	.10(5)	3.57(2)
I	.41(3)	2.91(3)	.32(2)	4.16(1)
J	.47(1)	3.02(3)	.52(4)	2.74(3)
K	1.10(2)	1.10(1)	.73(2)	2.20(1)
L	.89(2)	.90(3)	.61(1)	1.67(2)
M	.70(2)	3.03(2)	.80(1)	2.63(1)
N	.88(3)	.76(3)	.63(3)	1.28(2)

A11' is the area under the doublet 11'

A22' is the area under the doublet 22'

B.G = background

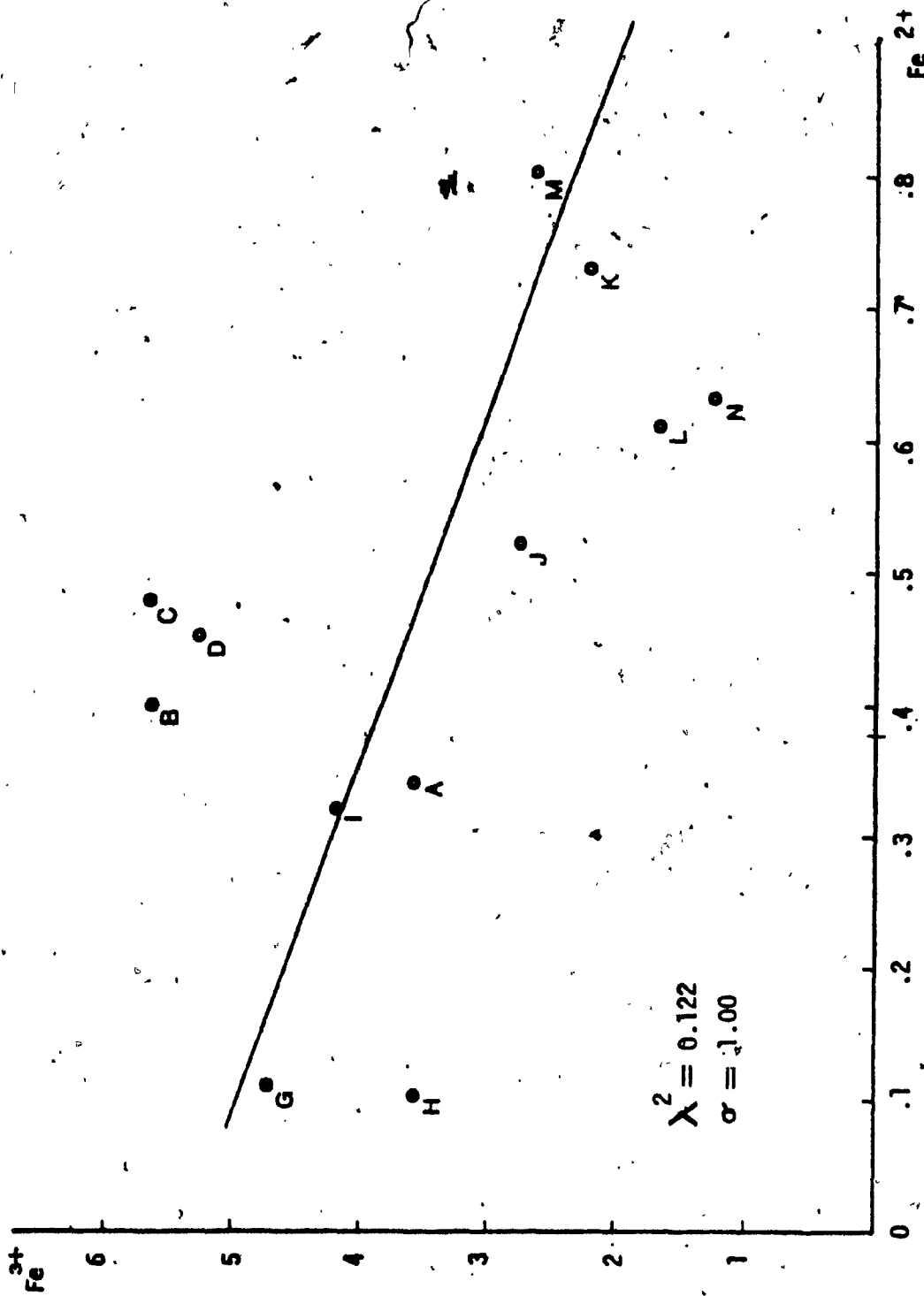


Fig. 45. Numerical designations of iron content of Fe³⁺ and Fe²⁺ in the mixed spectra are plotted versus each other.

The problem of obtaining pure separates pyroxene was discussed in chapter 7. However, because the spectra of garnet-pyroxene mixtures are resolvable into separate Fe peaks arising from the two minerals, the use of pure pyroxene absorbers was not considered essential in this study.

Numerical designation of the Fe contents of the two minerals were obtained from the areas under the peaks 22' for Fe^{3+} and 11' for Fe^{2+} in the mixed spectra. Table 7 shows the various parameters of the spectra of all absorbers analysed together with their Fe^{2+}/Fe and Fe^{3+}/Fe percentages and their percentage contents of garnet and pyroxene as determined by grain counting under the microscope.

The numerical designations of Fe contents shown in table 7, can not in themselves be used to test the proposed antipathetic relation. They have to be normalized:

i- To minimise the effects of variable background levels upon which the various spectral peaks are superimposed and
ii- To minimise the effects introduced by variable proportions of garnet and pyroxenes in the mixed absorbers. The first normalization was achieved by using ratios of areas under spectral peaks to background level, as numerical designations of Fe contents, and by recalculating the background-normalized numerical designations on the basis that garnet and pyroxene in the mixed absorbers were present

in equal amounts. The normalized values thus obtained are given in Table 8.

Considering that all the determinable Fe in garnet is in the form of Fe^{3+} and all that determinable Fe in pyroxene is in the form of Fe^{2+} , plots of numerical designations of Fe contents in garnet (column IV of table 8) versus numerical designations of Fe contents in pyroxene (column III of table 8) are shown in Figure 45. The line which has been drawn by least square fitting shows the trend defined by the data. This trend is ~~ob~~arsely consistent with antipathetic relation in the Fe contents between the two minerals.

Although a negative correlation of Fe contents of the two minerals is indicated by the data they do show a considerable degree of scatter. This may reflect the cumulative effect of the variability of the oxidation state of Fe in the skarn forming solutions which arrived at a particular sampling site. The scatter also may be, to some extent, an artifact produced by errors introduced in arriving at the numerical designations of Fe contents. The principal sources of error are as follows:

- 1- Sensitivity of the Mössbauer method as a technique for the determination of Fe in minerals.
- 2- Sampling errors in the field as well as in the laboratory (preparation of absorbers)
- 3- Errors in the grain counting technique in yielding the

proportions of the two minerals in the mixed absorbers.

4- Differences in the size of the grains.

5- Errors in calculating of areas under spectral peaks.

6- Presence of Fe bearing impurities in the samples.

7- Presence of minor (below resolvable limits) of Fe²⁺ in garnet, and Fe³⁺ in pyroxene.

8.1. COLOUR DEPENDENCE TO THE IRON CONTENT

The existence of antipathetic relation between garnet and pyroxene in terms of iron content was suggested by Wares and Williams-Jones.³⁴ The idea was based on colour variation of the pyroxenes and garnets with respect to each other, such that the lighter the garnet, darker the pyroxene, and vice versa. Darker colour correspond to the samples with more iron content, and lighter colour to the samples with less iron content. In this section we investigate the dependence of the colour to the iron content and its correlation to the antipathetic relation.

In order to specify the colour of each sample, the rock colour chart by Geological Society of America was used. This chart is designed primarily for field use, but nevertheless it indicates the range of rock colours for all purposes. The form and arrangement of the chart are based on the Munsell system. This system is based on a colour solid or approximately a colour sphere, which has a neutral gray axis grading from white at the top to black at the bottom

(Fig.46). This property is called "value". Around the circumference or equator of the solid are the 10 major hues shown in Fig. 48, each of which is divided into 10 numbered divisions, so that 5 marks the middle of a hue and 10 marks the boundary between one hue and the next. Thus any particular hue can be designated by a number and a letter such as 5R or 10YR. Any single vertical section through the neutral gray axis and a particular hue constitutes a colour chart on which the colour grade in value from light at the top to the dark at the bottom and in chroma (degree of saturation) from gray at the left to the most vivid colours at the right. Both value and chroma are numbered so any particular colour can be given a numerical designation representing hue, value, and chroma such as 5R 6/4 and 10YR 8/2. In table 9 the colour of pyroxene and garnet in each sample are shown, along with the numerical designation of each colour. This table is constructed such that the colour of the pyroxenes starts from the lightest colour (first row) to the darkest colour (last row). Included in this table are the numerical designation of iron content in each sample, taken from table 8. The colour names are taken from the Inter-Society Colour Council-National Bureau of Standards, sometimes modified by the rock-colour chart committee.

Table. 9 . Munsell color and numerical designation of pyroxenes and the garnets, along with numerical designation of iron content taken from table. columns III and IV.

Samp.	Munsell color and numerical designation (Pyroxene)	(III)	Munsell color and numerical designation (Garnet)	(IV)
A	pale greenish yellow 10Y8/2	.34	dark reddish brown 10R3/4	3.61
G	yellowish gray 5Y7/2	.11	grayish red 5R4/2	4.71
N	pale green 10G7/4	.63	moderate reddish brown 10R4/6	1.28
H	pale olive 10Y6/2	.10	blackish red 5R2/2	3.57
M	moderate greenish yellow 10Y8/2	.80	very dark red 5R2/6	2.63
I	light olive 10Y4/2	.32	dusky red 5R5/4	4.16
J	light olive gray 5Y5/2	.52	blackish red 5R2/2	2.74
B	grayish green 10GY5/2	.40	pale yellowish brown 10YR6/2	5.63
D	grayish green 10GY5/2	.45	dusky red 5R5/4	5.26
C	grayish olive 10Y4/2	.48	dusky red 5R5/4	5.64
K	grayish olive 10Y4/2	.73	moderate reddish brown 10R4/6	2.20
L	grayish olive 10Y4/2	.61	pale reddish brown 10R5/4	1.67

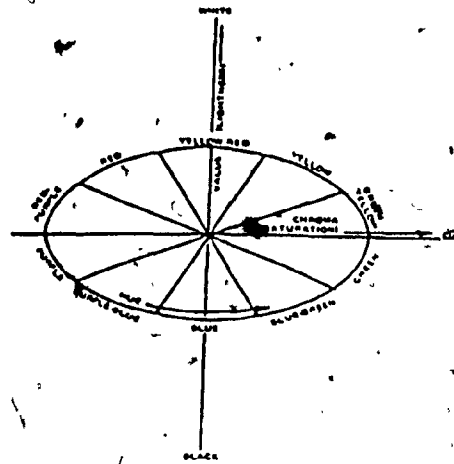


Fig.46. Dimensions of the colour solid.

The results given in table 9 are obviously not in favour to the main idea, that the darkness increases with increase in iron content. The numerical designation of iron content in table 8 column 3 show that, for instance sample C (pyroxene) with very darker colour than sample M, has less amount of iron compare to sample M (0.48 to 0.80). This is also true for some other samples. In case of the garnets, also sample J with dark red colour shows very lower amount of iron than the sample B with the pale yellowish brown colour.

8.2. Other contributory factors to colouring

One of the aspects which contributes to the colour of the minerals containing transition metals is known as "charge transfer" phenomena. This phenomenon is due to the electron migration between atoms or ions. The charge transfer transitions may take place from metal to ligand, ligand to metal, or metal to metal and resulting intense colour of the mineral.

Charge transfer transitions are favoured when neighbouring ions in a structure are in different oxidation states, e.g. Fe^{2+} and Fe^{3+} , and/or when there is a local misbalance due, for example, to substitution of a divalent ion for a trivalent ion or vice versa. Vivianite, $\text{Fe}_3(\text{PO}_4)_2 \cdot 8\text{H}_2\text{O}$ presents a dramatic example of the development of a deep colour on attainment of mixed valence. The pure mineral containing only Fe^{2+} is colourless until exposed to air whereupon a small amount of Fe^{3+} is produced and the mineral becomes an intense blue colour, which is attributed to the charge transfer transitions.

Another well-known factor that affects the colour of the minerals is the presence of impurities. Microprobe analysis of garnets and pyroxenes from the Sullipek deposit show that they contain impurities in the form of Ti^{4+} and Mn^{2+} (Wares, personal communication 1984). The presence of these elements in the minerals should be considered when correlating the Fe contents with the colour of the minerals.

8.3. SUMMARY AND CONCLUSIONS

The idea of an antipathetic relation in the iron contents of garnets and pyroxenes of the Sullipek deposit was originally proposed on the basis of the colour relationship between the two minerals. The results obtained from this study show that data are consistent with the concept of an antipathetic relationship. However, while a

correlation between the colour of the minerals and their iron content may be present in a very general way, such a correlation can not be established from the limited amount of data obtained through this study. Also, in addition to the iron content, other factors such as charge transfer phenomena and the presence of impurities contribute to the colour of minerals.

CHAPTER IX

Mössbauer Spectra of Fe^{3+} in GASH Guanidinium Aluminum Sulfate Hexahydrate $\text{C}(\text{NH}_2)_3 \text{Al}(\text{SO}_4)_2 \cdot 6\text{H}_2\text{O}$

The crystals were grown by slow evaporation of an aqueous solution containing calculated stoichiometric amounts of guanidinium sulfate $[\text{HNC}(\text{NH}_2)_2]_2 \cdot \text{H}_2\text{SO}_4$, aluminum sulfate $\text{Al}_2(\text{SO}_4)_3$ and ferric sulfate $\text{Fe}_2(\text{SO}_4)_3$. $\text{Fe}_2(\text{SO}_4)_3$ was prepared by dissolving ^{57}Fe metal (enriched to 90%) in a sufficient amount of dilute sulfuric acid and then adding hydrogen peroxide to convert all ferrous (Fe^{2+}) ions to ferric (Fe^{3+}) ions. The solution was made slightly acidic with sulfuric acid to prevent hydrolysis of the ferric ions. The amount of $\text{Fe}_2(\text{SO}_4)_3$ used was such that there was one Fe^{3+} ion for every five Al^{3+} ions in the solution. At first, small crystals formed on the surface of the solution, later they sank to the bottom. One of them used as a seed crystal to grow a bigger crystal appropriate to Mössbauer measurements. This required periodic removal of the seed crystal and dissolving the other small crystals by adding controlled amounts of distilled water. The crystals grew as hexagonal plates with normals parallel to the c-axis, Fig 47.

Crystal Structure

The crystal structure of GASH has been determined by Geller and Booth. The unit-cell parameters are: $a=11.745 \text{ \AA}$ and $c=8.592 \text{ \AA}$. The point group symmetry of this trigonal crystal

is C_{3v} and the space group is $P31m$ with three molecules per unit cell as shown in Fig 48. The Al^{3+} ions (replaced by Fe^{3+}) are on a threefold axis and are surrounded by a somewhat distorted octahedra of water molecules. The Guanidinium ions lie above and below the octahedra and are loosely bound. Two of the three Al^{3+} (Fe^{3+}) ions per unit cell are equivalent to each other and belong to site II, while the other belongs to site I. In the Mössbauer spectra this is equivalent to having two doublets, corresponding to Fe^{3+} occupying sites I and II.

MOTIVATION AND RESULTS

The object of the present investigation is to measure the quadrupole coupling constant $(e^2qQ)/\hbar$ for Fe^{3+} occupying the two different sites of GASH (I and II), then by using these measurements to examine the suggested linear relationship between $(e^2qQ)/\hbar$ and the axial crystalline field amplitude $|(A-B)/A|$, as derived by Schlaak in context with Mn^{2+} -doped crystals. The analysis of Schlaak predicts a linear dependence of $|(A-B)/A|$ on Q ($=1/2e^2qQ/\hbar$) the coefficient of the term $[L_z^2 - I(I+1)/3]$ in the spin Hamiltonian.

Relatively few ENDOR measurements have been reported to date on Fe^{3+} -doped single crystals. These are for example, those performed in the host lattices of Si^{30} , CaO^{31} , MgO^{32} , SnO^{33} , and $RbAl$ and $RbGa$ sulfate alums. The crystalline

electric field at the Fe^{3+} site in MgO and CaO is of octahedral symmetry, while in SnO it is strongly rhombic. On the other hand, it is of trigonal symmetry in RbAl and RbGa sulfate alums, as well as in GASH. However, in GASH the trigonal distortion is much larger than that in sulfate alums. ENDOR measurements of the values of A and B for Fe^{3+} in GASH have been recently measured rather accurately by Misra and Ormond.²⁹

The crystal of GASH has hexagonal cross section, the GASH absorber had the area $\sim 2 \text{ cm}^2$ and thickness $\sim 2.2 \text{ mm}$. The spectra were obtained in the 2 mm/sec velocity range, using 256 channels of the multi-channel analyzer (Figure 49). This velocity was chosen since we expect to see the Fe^{3+} peaks in this region. The direction of the gamma rays were parallel to the c-axis of the crystal.

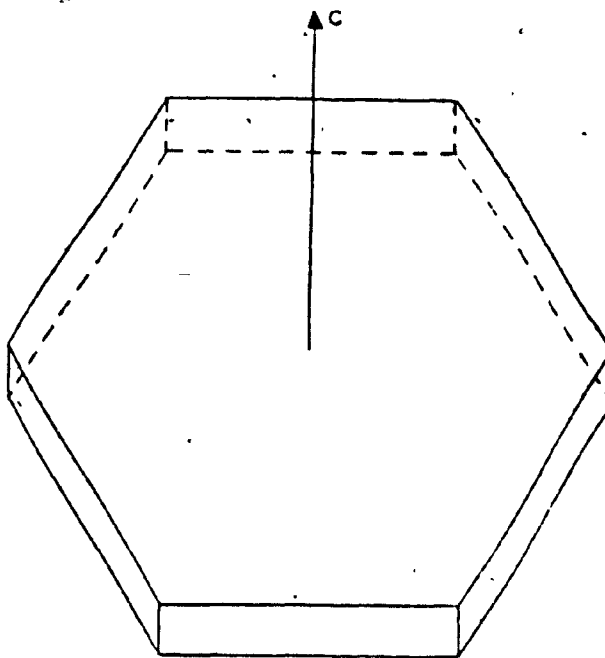


Fig.47. Crystal growing habit of GASH

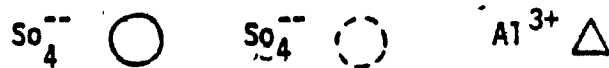
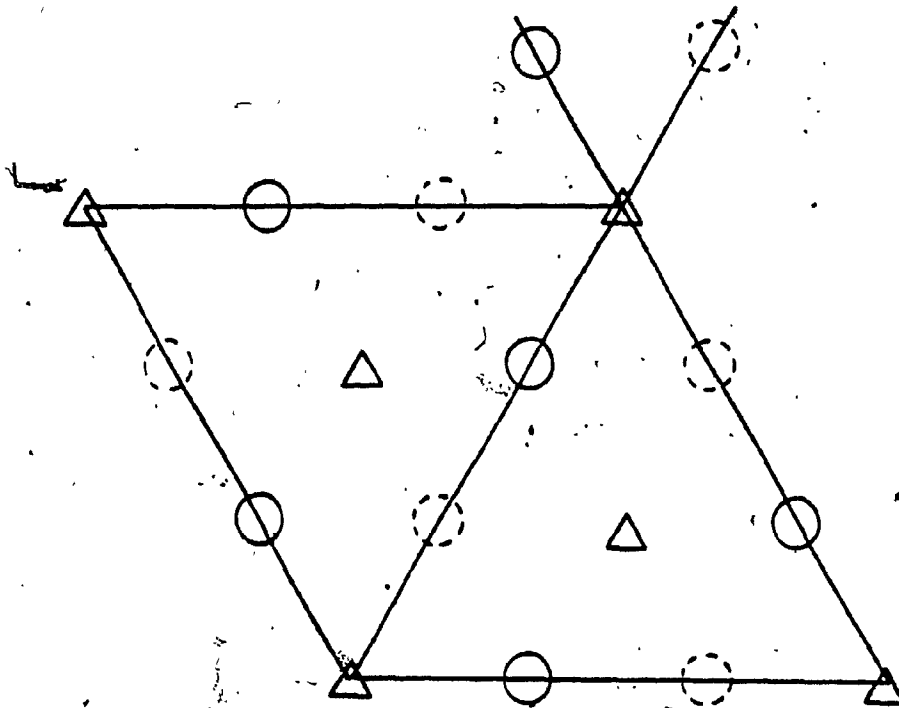


Fig.48: A schematic of a unit cell of GASH looking down the c-axis. The triangles represent threefold axis with Al^{3+} ions in the plane of the paper and a guanidinium ion above and below. Each Al^{3+} ion is octahedrally surrounded by six waters. The circles represent SO_4^{--} groups above the plane and the dotted ones below.

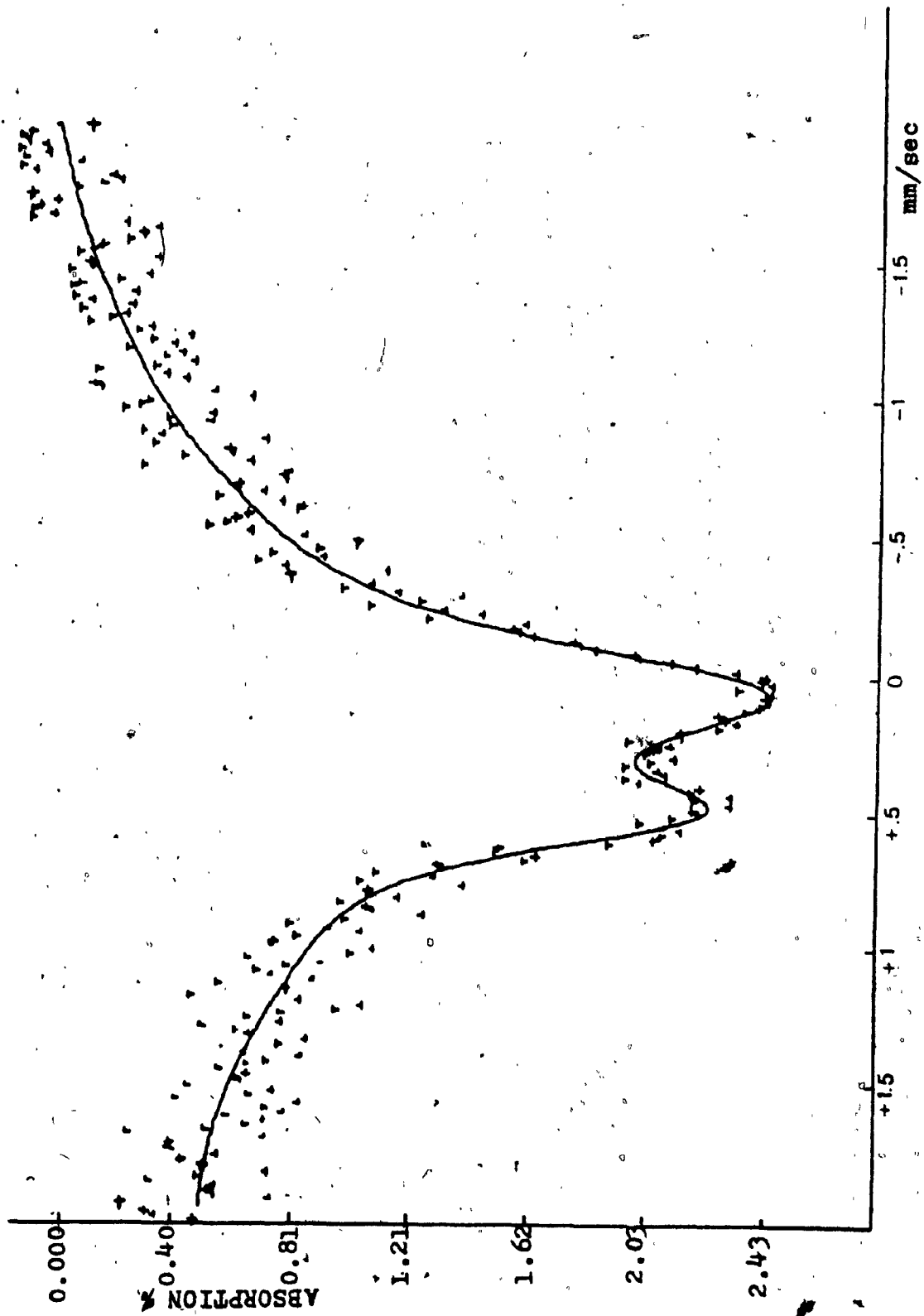


Fig. 49. Computer plot of the Mössbauer spectra of GASH (Background Count = 942000).

The spectra were computer fitted to two and four Laurentzian line shape peaks. The two-peak fit (one doublet) was characterized by a $\chi^2 = 252$, yielding the parameter values to be $Q.S = 0.499 \pm 0.003$ mm/sec and $I.S = 0.66 \pm 0.004$ mm/sec. These are close to the expected values for Fe^{3+} occupying an octahedral site. The four-peak fit (two doublets) was characterized by a χ^2 value of 266, the Q.S values were 0.51 and 0.33, while the corresponding I.S values were 0.66 and 0.71. These are obviously quite different from each other, apart from having a larger χ^2 value from that for the two peak-fit. Therefore, it is clear that the two doublets corresponding to the sites I and II can not be reasonably well resolved by Mössbauer spectroscopy. We have therefore estimated the average Q.S and I.S, for the two sites from the two-peak fit. Using the value of Q.S, the quadrupole coupling constant ($e^2 qQ / \hbar$) is calculated to be 11.58 ± 1 MHz. The values of $|A-B|/A$ as determined from the ENDOR studies on GASH by Misra and Ormondt were used. These values are 3.223×10^{-2} and 3.949×10^{-2} for sites I and II, respectively. Thus, the ratio $|A-B|/A / (e^2 qQ / \hbar)$ for GASH corresponding to the sites I and II are found to be 0.0028 and 0.0034 MHz respectively, as calculated using the value of 11.54 MHz (for both the sites) for $e^2 qQ / \hbar$ as determined from our Mössbauer experiment. There are only two hosts for which the experimental values of A, B, and $e^2 qQ / \hbar$ (obtained by Mössbauer spectroscopy in the same way as that for the

present case) are available. The only ones for which they are available are octaethylhemine and rutile (TiO_2). These are, for TiO_2 , $A_x = -28.8$ MHz, $A_y = -27.6$ MHz, $A_z = -28.2$ MHz, and $e^2 qQ / \hbar = 6.9$ MHz, and for octaethylhemine, $A = 16.24$ MHz, $B = 15.08$ MHz, and $e^2 qQ / \hbar = 21.58$ MHz. Using these values it is found that the ratio $|(A-B)/A| / (e^2 qQ / \hbar)$ are 0.003 and 0.0033 for TiO_2 and octaethylhemine hosts, respectively, which is in agreement, within experimental error, to that found for GASH. This lends support to the existence of linear relationship between $|(A-B)/A|$ and $e^2 qQ / \hbar$ as discussed by Schlaak²⁸.

CONCLUSIONS

1. In studying the garnets from the Sullipek deposit, their spectra and the parameters derived from computer analysis, indicate that the mineral is andradite with no detectable Fe^{2+} in their structure, except samples E and F in which a proportion of Ca^{2+} had been replaced by Fe^{2+} and resulted in additional peaks on their Mössbauer spectra.
2. The analytical results are broadly consistent with the concept of an antipathetic relationship in iron contents between garnets and pyroxenes from the Sullipek deposit.
3. The colours of the minerals do not merely depend on the iron content. The colour also is dependent on charge transfer phenomena and on the presence of impurities.
4. No direct relation was found to hold between the colour of these minerals and the antipathetic relation.
5. The importance of the use of the Mössbauer technique, in conjunction with other type of spectroscopies, is demonstrated by the experiment on GASH. The measurements of quadrupole coupling constant (e^2qQ/h), by the Mössbauer technique and that of the hyperfine parameters A and B by

ENDOR measurement, enabled us to confirm the linear relationship between $e^2 qQ/\hbar$ and $|(A-B)/A|$ for Fe^{3+} , as predicted by Schlaak for Mn^{2+} -doped crystals.

REFERENCES

1. G.M.Bancroft, Mössbauer Spectroscopy , an Intoduction For Inorganic Chemists and Geochemists, Mc Graw Hill, London. (1973).
2. G.K.Wertheim, Mössbauer Effect, Principles and Applications , Academic Press, New York, (1964).
3. A.Vertes, L.Korecz, and K.Burger, Mössbauer Spectroscopy Elsevier Scientific Publishing Co. Budapest Hungary, (1979).
4. G.K.Shenoy and F.E.Wagner, Mössbauer Isomer Shifts , North Holland Publishing Co., Amesterdam, (1978).
5. O.C.Kistner and A.W.Sunyar, Phys.Rev.Letters, 4 412(1960).
6. U.Gonser, Mössbauer Spectroscopy , Topics in Applied Physics, V.5, Springer-Verlag (1975).
7. R.P.Wares, Geological Re-Interpretation of The Sullipek/Pekan Deposit , Unpublished, (1982).
8. G.M.Bancroft, R.G.Burns, and R.A.Howie, Nature, 31,1223 (1967)
9. G.M.Bancroft, A.G.Maddock and R.G.Burns, Geochim. et Cosmochim. Acta, 31,2219 (1967).
10. G.M.Bancroft, P.G.L.Williams, and R.G.Burns, Am. Mineralogist 56,1617 (1971).
11. G.M.Bancroft, P.G.L.Williams and E.J.Essene, Mineral. Soc. Am. Spec. Pap. 2,59 (1969).
12. R.L.Mössbauer, Z.Physik, 151,124 (1958).
13. W.A.Deer, R.A.Howie and J.Zussman, Rock Forming Minerals V2, Longmans, London (1967).
14. S.P.Ekimov et.al., Geochem, Inter. 10,579 (1974).
15. P.G.L.Williams, et.al., Nature, Phy,. Science, 230,149 (1971).
16. J.B.Allcock, Gaspe Copper: A Devonian Porphyry Copper/Skarn Complex, Ph.D Thesis , Yale University (1978).
17. I.Y.Eladas, Investigation of Certain Iron Bearing Minerals and Rocks MSc. Thesis (unpublished), Concordia University, 1981
18. V.I.Goldanskii, and R.H.Herber, Chemical Applications of Mössbauer Spectroscopy , Academic Press, New York, (1968).
19. S.Geller and D.P.Booth, Z.Krist., 117,3 (1958).

20. E.G.Brock, D.Stripe, and I.Hormats, *J.Chem. Phys.*, 37,2735 (1962).
21. J.G.Stevens, and V.EStevens, Mössbauer Effect Data Index, IFI/Plenum, New York-Washington, (1972).
22. D.Virgo and S.S.Hafner, *Am. Mineralogist*, 55,201 (1970).
23. D.Virgo and S.S.Hafner, *Mineral. Soc. Amer. Spec. Pap.*, 2, 67 (1969).
24. I.S.Lyubutin, L.M.Belyaeva, R.Grzhikhova and I.Lipka *Soviet Physics, Crys.* 17,116 (1972).
25. G.A.Novak and G.V.Gibbs, *Am. Mineralogist*, 56,791 (1971).
26. W.J.Nicholson and G.Burns, *Phys. Rev.*, 129, 2490 (1963).
27. R.G.Burns, Mineralogical Applications of Crystal Field Theory, Cambridge University Press (1970).
28. M.Schlaak, *Ber. Bunsenges. Phys. Chem.* 79,1016 (1975).
29. S.K.Misra and D.V.Ormond, *Phys. Rev. B* 30,6327(1984).
30. G. W. Ludwig and H. H. Woodbury, *Phys. Rev.* 117, 1286 (1960)
31. R. Cavlo, M. C. G. Passegi, and R. A. Issacson, *Phys. Lett.* 31A, 407. (1970)
32. P. R. Locher and S. Gechwind, *Phys. Rev.* 139, A991 (1965).
33. W. Rhein, *Z. Naturforsch.* A27, 741 (1972).
34. R.P.Wares and A.E.Williams-Jones, *The Sullipek Cu-Mo Skarns Gaspe, Quebec: Geochemistry and Petrology of a Porphyry-Associated ore deposit*, Geological Association of Canada, Annual Meeting Abstracts (1982)

APPENDIX A

LEAST-SQUARES CURVE FITTING

The best least squares fitting occurs when there exist parameters p which can minimize the function defined by:

$$\chi^2 = \sum_{i=1}^N \left(\frac{\theta_i^{\text{exp}} - \theta_i(\vec{p})}{\Delta\theta_i^{\text{exp}}} \right)^2 \quad (1)$$

where θ_i^{exp} = measured number of counts in the i th channel, and $\theta_i(\vec{p})$ = corresponding number of counts calculated from an approximate knowledge of the parameters and model.

$\Delta\theta_i^{\text{exp}}$ = experimental error on θ_i^{exp} .

For a Lorentzian line shape :

$$\theta_i(\vec{p}) = \theta_i(A_j, x_j, C_j) = B - \sum_{j=1}^M \frac{A_j}{1 + \left(\frac{x_i - x_j}{C_j} \right)^2} \quad (2)$$

where B is the background, M the number of Lorentzian lines, A_j the line amplitude, C_j the half width at half maximum and x_i and x_j are the channel numbers.

The necessary condition for minimization of χ^2 is:

$$\vec{\nabla} \chi^2 = 0 \text{ or } \frac{\partial \chi^2}{\partial p_j} = 0 \text{ with } j=1, \dots, 3M \quad (3)$$

It is sufficient if all the eigenvalues of the second derivative matrix are positive. Actually, condition (3) is only satisfied to a certain degree i.e.,

$$\Delta \chi^2 = \epsilon \quad (4)$$

where ϵ is a small number depending on the precision of the fitting.

One can then expand $\theta_i(\vec{p})$ to the first order

$$\theta_i(\vec{p}) = \theta_i(\vec{p}_0) + \vec{\nabla}\theta_i \cdot \Delta\vec{p} \Big|_{\vec{p}=\vec{p}_0} \quad (5)$$

with $\Delta\vec{p} = \vec{p} - \vec{p}_0$. Equation (1) then becomes

$$\chi^2 = \sum_{i=1}^N \left(\frac{\theta_i^{\text{exp}} - \theta_i(\vec{p}_0) - \vec{\nabla}\theta_i \cdot \Delta\vec{p} \Big|_{\vec{p}=\vec{p}_0}}{\Delta\theta_i^{\text{exp}}} \right)^2 \quad (6)$$

the solution $\Delta\vec{p}$ which minimizes χ^2 is given by:

$$\Delta\vec{p} = -\alpha^{-1} \vec{\nabla}\chi \quad (7)$$

where α is the second derivative matrix (or error matrix).

The search for χ^2 minimum is thus carried out in the $-\vec{\nabla}\chi^2$ direction by replacing \vec{p}_i by $\vec{p}_i + \Delta\vec{p}$ for each step in the iteration procedure. The minimum is achieved with $\Delta\vec{p} \rightarrow 0$. The errors of the parameters involved in such calculations are the square roots of the diagonal elements of the second derivative inverse matrix α^{-1} :

$$\delta p_i = \alpha_{ii}^{-1/2} \quad (8)$$

The results of each iteration, especially χ^2 and $|\vec{\nabla}\chi^2|^2$ are given and their convergence will show whether the input parameters and the line shape are of proper choice.

Mössbauer Memory

The parameters involved are the line positions, line heights and line widths.

Equation (2) is computed by the subroutine FUNC which calculates also its first and second derivatives. The iterations are performed through the subroutine CURFIT. The two subroutines EXAM and JACOBI are used to compute equation (7), and equation (8) is obtained by the subroutine MATINV.

PROGRAM MÖSSBR (INPUT,OUTPUT,TAPE5=INPUT,TAPE6=OUTPUT,TAPE80)

C
C
C CURVE FITTING LINE + LORENTZIANS
C M =NUMBER OF PARAMETERS
C KG =NUMBER OF LORENTZIANS UP TO SIX
C L4 =NUMBER OF ITERATIONS ALLOWED
C NO =INITIAL CHANNEL OF THE GROUP
C N =NUMBER OF CHANNELS IN THE GROUP
C B(3*KG+2)=SLOPE
C B(3*KG+1)=BACKGROUND
C B(3*J) =CHANNEL NUMBER OF PEAK
C B(3*J-1) =HALF WIDTH AT HALF MAXIMUM
C B(3*J-2) =HEIGHT OF THE PEAK
C RUNNO=PROVIDES 18 SPACES FOR SPECIFYING THE DATE OF
C EXPERIMENT
C SAMPLE=PROVIDES 72 SPACES FOR SPECIFYING THE SAMPLE
C TIME=PROVIDES 12 SPACES FOR SPECIFYING THE DURATION OF
C EXPERIMENT
C ***ALL INPUT DATA IS READ IN SUBROUTINE MDATA ****

C
C DIMENSION Z(256),FM(256),FC(256),DF(256),ERR(256),
1B(20),B1(20),B2(20,20),DC(2800),S(6),DAT(256),RUNNO(5),
2S1(6),P(6),PE(6),PH(6),PHE(6),
3PW(6),PWE(6),A(6),AE(6),SAMPLE(5),ABC(2),Y(4),TIME(5),
3DATA(256),YFIT(256),FDATA(512),IDATA(512)
COMMON/DATA/ABC,Y
COMMON DC
EQUIVALENCE (Z,DC),(FM,DC(257)),(FC,DC(513)),(DF,DC(769)),
1(ERR,DC(1025)),(B1,DC(1281)),(B2,DC(1301)),(N,DC(1701)),
2(L4,DC(1703)),(Q1,DC(1704)),(Q2,DC(1705)),(M,DC(1706)),
3(B,DC(1719)),(I,DC(2180)),(L,DC(2179)),(KG,DC(2182)),
4(IDATA,DC(2200)),
5(NO,DC(2720)),(JO,DC(2721)),(SAMPLE,DC(2722)),
6(TIME,DC(2727)),(RUNNO,DC(2732))
DATA(ABC=2HNO,3HYES),(Y=1H,1HC,1H*,1HM)

C
C READ IN SPECTRUM
C DATA= MÖSSBAUER DATA CORRECTED LATER FOR CURFIT
C Q1 AND Q2 ARE THE PRECISIONS OF THE CURVE FITTING
C

WRITE(6,188)
CALL MDATA
7 FORMAT(2F5.2)
WRITE(6,8) Q1,Q2
8 FORMAT(1X,4HQ1 = ,F5.2,5X,4HQ2 = ,F5.2)
DO 301 IA=1,512
301 FDATA(IA)=FLOAT(IDATA(IA))
WRITE(6,56)
56 FORMAT(10X,*INITIAL DATA*,//)
55 FORMAT(10X,10F9.0)
FDATA(1)=FDATA(2)
FDATA(512)=FDATA(511)
FDATA(256)=FDATA(255)

```

          FDATA(257)=FDATA(258)
C      THE FOLLOWING FOR REMOVING ANY DATA POINT SCATTERED TOO FAR
      DO 50 J=3,512
      D1=FDATA(J-1)*0.5
      D2=FDATA(J-1)*1.5
54     CONTINUE
      IF (FDATA(J).GT.D1.AND.FDATA(J).LT.D2) GO TO 51
      FDATA(J)=(FDATA(J-1)+FDATA(J-1))/2.
53     FORMAT(5X,*ERRATIC CHANNEL CORRECTED AGAIN*)
      GO TO 54
51     CONTINUE
50     CONTINUE
52     FORMAT(5X,*ERRATIC CHANNEL NUMBER=*,I4)

C
C
32     FORMAT (12X,10F6.0)
      PRINT 100
100    FORMAT (1H1)
      4     FORMAT(10X,10F9.0)
      WRITE (6,188)
C      SS=0. ONLY ANALYSE CHANNEL 1 TO 256
C      SS=1. OVERLAP CHANNELS 257 - 512 ON CHANNELS 1- 256
      SS=0.
      IF(SS) 58,58,59
59     CONTINUE
      DO 66 J=1,256
      DATA(J)=(FDATA(J)+FDATA(513-J))/2
66     CONTINUE
      GOTO71
58     CONTINUE
      DO70J=1,256
70     DATA(J)=FDATA(J)
71     CONTINUE
88     FORMAT(10X,10F9.0)
188    FORMAT (1H1)
      WRITE (6,188)
      1     FORMAT(18A1)
      WRITE(6,2)RUNNO
      2     FORMAT (1X,14H RUN NUMBER=      ,5A10/)
220    FORMAT (5A10)
      WRITE (6,222) SAMPLE
222    FORMAT(1X,14H SAMPLE      =      ,5A10/)
150    FORMAT (2A6)
      WRITE(6,151) TIME
151    FORMAT(1X,14H TIME      =      ,5A10/)
939    FORMAT (4I3)
      WRITE(6,10)NO,N,KG
10     FORMAT(1X20H*INITIAL CHANNEL=      I3,25H      *NUMBER OF CHANNE
113,29H      NUMBER OF LORENTZIAN=      I2/)
      DO 111 J=1,256
      DAT(J)=DATA(J)
111    CONTINUE
      M=3*KG+2
      NN=N

```

```

DO 115 J=1,NN
KNO=J+N0
Z(J)=(KNO-1)
FM(J)=DAT(KNO-1)
115 ERR(J)=SQRT(FM(J))
89 FORMAT (1F8.0)
WRITE(6,11)B(3*KG+1)
11 FORMAT (1X14H BACKGROUND= F8.0/)
B(3*KG+2)=0.0
122 FORMAT(6F3.0)
5 FORMAT(6F8.0)
WRITE(6,13) (B(3*J-2),J=1,KG)
13 FORMAT(1X,16H PEAK HEIGHTS= 6F15.0/)
12 FORMAT(1X,18H PEAK POSITIONS= 6(F15.0)/)
WRITE(6,12) (B(3*J),J=1,KG)
120 FORMAT(6F5.3)
WRITE(6,14) (B(3*J-1),J=1,KG)
14 FORMAT(1X,9H SIGMA= 6F15.3///)
KG1=KG
DO 21 J=1,KG1
21 B(3*J-2)=B(3*J-2)*B(3*J-1)**2/10000.0
B(3*KG+1)=B(3*KG+1)/10000.0
DO 22 J=1,NN
FM(J)=FM(J)/10000.0
22 ERR(J) = ERR(J)/10000.
WRITE (6,1881)
1881 FORMAT (39H0 CURVE FITTING LINE+LORENTZIANS //)
CALL CURFIT
WRITE(6,188)
WRITE (6,135)
135 FORMAT(1X,11H PARAMETERS//3X,1HJ,10X,4HB(J),27X,6HERRORES//)
WRITE (6,140) (J,B(J),B1(J),J=1,M)
140 FORMAT(3X,I2,5X,E16.6,15X,E16.6 /)
DO 200 J=1,KG
P(J)=B(3*J)
PE(J)=B1(3*J)
PH(J)=10000.0*B(3*J-2)/B(3*J-1)**2
T=2.0*(B1(3*J-1)/B(3*J-1))**2
W=(B1(3*J-2)/B(3*J-2))**2
PHE(J)=PH(J)*SQRT(T+W)
PW(J)=2.0*B(3*J-1)
PWE(J)=2.0*B1(3*J-1)
A(J)=31415.9265*B(3*J-2)/B(3*J-1)
TT=(B1(3*J-1)/B(3*J-1))**2
WW=(B1(3*J-2)/B(3*J-2))**2
AE(J)=A(J)*SQRT(TT+WW)
200 CONTINUE
WRITE(6,188)
WRITE (6,201)
201 FORMAT (1X,15H LINE POSITIONS,6X,7H ERRORS/)
WRITE (6,202) (P(J);PE(J),J=1,KG)
202 FORMAT (3X,1F10.5,6X,1E11.4/)
WRITE (6,203)
203 FORMAT (/ ,1X,13H LINE HEIGHTS,8X,7H ERRORS/)

```

```

WRITE (6,204) (PH(J),PHE(J),J=1,KG)
204 FORMAT(2X,F10.3,10X,E10.4/)
WRITE (6,205)
205 FORMAT (/ ,1X,14H FWHM OF LINES,7X,7H ERRORS/)
WRITE (6,206) (PW(II),PWE(II),II=1,KG1)
206 FORMAT (3X,1F10.6,6X,1E11.4/)
WRITE (6,207)
207 FORMAT (/ ,5X,11H LINE AREAS,8X,7H ERRORS/)
WRITE (6,208) (A(J),AE(J),J=1,KG)
208 FORMAT (1X,1F16.6,2X,1E16.6/)
WRITE (6,188)
CALL PLOTB(NO,N,FC,FM)
NN=N
DO 40 KK=1,NN
FC(KK) = FC(KK)*10000
FM(KK) = FM(KK)*10000
40 CONTINUE
WRITE(6,188)
WRITE(6,935) (FM(KJ),KJ=1,NN)
WRITE(80,935) (FM(KJ),KJ=1,NN)
WRITE(6,935) (FC(KJ),KJ=1,NN)
WRITE(80,935) (FC(KJ),KJ=1,NN)
935 FORMAT(5X,10F7.0)
9481 FORMAT (5H""N=,I5,5H/"NO=,I5,2H//)
16 FORMAT (I1)
STOP
END
SUBROUTINE MDATA
DIMENSION IDATA(512),DC(2800),IIDATA(512),B(20),C(20),
LSAMPLE(5),TIME(5),RUNNO(5),SAM(5),TIM(5),RUN(5)
COMMON DC
EQUIVALENCE (IDATA,DC(2200)),(Q1,DC(1704)),(Q2,DC(1705)),
1(N,DC(1701)),(KG,DC(2182)),(L4,DC(1703)),(B,DC(1719)),
2(NO,DC(2720)),(JO,DC(2721)),(SAMPLE,DC(2722)),
3(TIME,DC(2727)),(RUNNO,DC(2732))
READ(5,1150) (IIDATA(I),I=1,512)
DO 145 K3=1,512
IIDATA(K3)=IIDATA(K3)
145 CONTINUE
1150 FORMAT(I6,9I7)
DATA (RUN(J),J=1,2)/10HSEP.20-OCT,8H.20,1977/
DATA (SAM(J),J=1,2)/10HCO-57SOURC,1HE/
DATA TIM(1)/9HONE MONTH/
DATA (C(I),I=1,20)/
5-2000.,12.,12.,-5000.,12.,104.,-9000.,12.,120.,
6-7000.,12.,143.,-3000.,12.,156.,-6000.,12.,200.,
2946000.,0.0001/
DO 100 IA=1,512
100 IDATA(IA)=IIDATA(IA)
DO 200 J=1,20
200 B(J)=C(J)
DO 300 J=1,20
RUNNO(J)=RUN(J)
SAMPLE(J)=SAM(J)

```

```

300 TIME(J)=TIM(J)
    NO=1
    N=256
    KG=6
    L4=18
    Q1=0.
    Q2=.01
    JO=1
    RETURN
    END

```

```

SUBROUTINE CURFIT
C   F O R T R A N 4
    DIMENSION Z(256),FM(256),FC(256),DF(256),ERR(256),X(256),
    1B(20),B1(20),B2(20,20),GRAD(20),D1(20),D2(20,20),DC(2800),
    2B3(20,20),AA(20),BB(20),W1(20),W2(20),ABC(2),B8(20,20),
    3Y(4)
    COMMON/DATA/ABC,Y
    COMMON DC
    EQUIVALENCE (Z,DC), (FM,DC(257)), (FC,DC(513)), (DF,DC(769)),
    1(ERR,DC(1025)), (B1,DC(1281)), (B2,DC(1301)), (N,DC(1701)),
    2(L4,DC(1703)), (Q1,DC(1704)), (Q2,DC(1705)), (M,DC(1706)),
    3(B,DC(1719)), (GRAD,DC(1739)), (D1,DC(1759)), (D2,DC(1779)),
    4(I,DC(2180)), (L,DC(2179))
    DATA(ABC=2HNO,3HYES), (Y=1H ,1HC,1H*,1HM)
    L1 = 0
    SA = 0.0
    DO 1000 J=1,20
    B1(J)=0.0
    DO 1000 K=1,20
1000 B2(J,K)=0.0
    NN=N
    MM=M
    DO 100 K = 1, NN
    X(K) = ERR(K)**2
    L=1
    I=K
    CALL FUNC(2)
    DF(K) =FM(K) - FC(K)
    DO 101 J=1,MM
    B1(J)=B1(J)-(2.0*DF(K)*D1(J))/X(K)
    DO 101 KK=1,MM
101 B2(J,KK)=B2(J,KK)-(2.0*(DF(K)*D2(J,KK)-D1(J)*D1(KK)))/X(K)
100 SA = SA + DF(K)**2/X(K)
    GMOD=0.0
    DO 102 J=1,M
102 GMOD=GMOD+B1(J)**2
    WRITE(6,243)SA,GMOD
    243 FORMAT (1X,26H*INITIAL VALUE SUM OF SQ.=E13.5,20X,17H*SQ
MOD OF GR
    1AD =E13.5)
    WRITE(6,1751)
1751 FORMAT(14H0 DERIVATIVES-)
    WRITE(6,240)(B1(J),J=1,M)

```

```

240 FORMAT (15X,5(E13.5,8X)/)
   IF (SA - Q1) 110, 110, 200
110 LE = 1
   GO TO 600
200 S = 0.0
   GMOD = 0.0
   BMOD = 0.0
   PROD = 0.0
   A2=ABC(1)
   DO 210 J = 1, MM
   B1(J) = 0.0
   DO 210 K = 1, MM
210 B2(J,K) = 0.0
   DO 220 JJ = 1, NN
   L=1
   I=JJ
   CALL FUNC(2)
   DF(JJ) = FM(JJ) - FC(JJ)
   DO 220 J = 1, MM
   B1(J) = B1(J) - (2.0*DF(JJ)*D1(J))/X(JJ)
   DO 220 K = 1, MM
220 B2(J,K) = B2(J,K) - (2.0*(DF(JJ)*D2(J,K) - D1(J)*D1(K)))/
   LX(JJ)
   DO 230 J = 1, MM
230 GRAD(J) = B1(J)
   L1 = L1 + 1
   CALL EXAM (B2,B1,M,LF)
   IF (LF) 250, 250, 305
250 DO 231 II=1,M
   DO 231 JJ=1,M
231 B3(II,JJ)=B2(II,JJ)
   CALL JACOBI (M,B3,1,NR,B2)
   MM=M
   DO 235 JJ=1,MM
235 B1(JJ)=B3(JJ,JJ)
   A2=ABC(2)
   DO 260 J = 1, MM
260 D1(J) = 0.0
   DO 270 J = 1, MM
   DO 270 K = 1, MM
270 D1(K) = D1(K) + B2(J,K) *GRAD(J)
   DO 275 J = 1, MM
   IF (B1(J)) 280, 290, 285
280 B1(J) = - B1(J)
285 D1(J) = D1(J)/B1(J)
   GO TO 275
290 D1(J) = 0.0
275 CONTINUE
   DO 295 J = 1, MM
295 B1(J) = 0.0
   DO 300 J = 1, MM
   DO 300 K = 1, MM
300 B1(J) = B1(J) + B2(J,K)*D1(K)
305 DO 310 J=1,M

```



```

      GMOD = GMOD + GRAD(J)**2
      BMOD = BMOD + B1(J)**2
310  PROD = PROD + GRAD(J)*B1(J)
      IF (GMOD - Q2) 315, 315, 320
315  LE = 2
      GO TO 600
320  C=PROD/SQRT(BMOD*GMOD)
      IF (C) 335, 335, 400
335  LE = 4
      GO TO 600
400  LD = 0
      L3 = 0
      DO 410 J = 1, MM
410  GRAD(J) = B(J) - B1(J)
450  DO 420 II = 1, NN
      L=2
      I=II
      CALL FUNC (I)
      DF(II) = FM(II) - FC(II)
420  S = S + DF(II)**2/X(II)
      IF (SA - S) 435, 500, 500
435  LD = LD + 1
430  DO 440 J = 1, MM
      B1(J) = B1(J)/2.0
440  GRAD(J) = B(J) - B1(J)
      S = 0.0
      L3 = L3 + 1
      IF (L3 - 256) 450, 460, 460
460  LE = 5
      GO TO 600
500  IF (LD) 505, 505, 506
506  LD = 0
      GO TO 430
505  DO 510 J = 1, MM
510  B(J) = GRAD(J)
      SA = S
      IF (SA - Q1) 507, 507, 530
507  LE = 1
      GO TO 600
530  IF (L4) 200, 200, 900
900  WRITE(6,920)L1,A2,L3,S,GMOD,(B(J),J=1,M)
920  FORMAT(//,15H ITERATION NO.=I5,10X,43H TRANSFORMATION,
      1MADE TO PRINCIPAL AXES=A4,10X, 18H BINARY CHOP USED
      2=I3,6H TIMES/LX,27H WEIGHTED SUM OF SQUARES=E14.7,25
      3X,32H SQUARE MODULUS OF GRADIENT=E14.7/20H PARAMETERS //)
      4B(J)-/(6E17.8)H/)
      IF (L1 - L4) 200, 910, 910
910  LE = 6
      GO TO 600
600  DO 710 J=1,MM
      B1(J) = 0.0
      DO 710 K=1,MM
710  B2(J,K) = 0.0
      L=1

```

```

DO 720 JJ = 1, NN
CALL FUNC(2)
DF(JJ) = FM(JJ) - FC(JJ)
DO 720 J = 1, MM
B1(J) = B1(J) - (2.0*DF(JJ)*D1(J))/X(JJ)
DO 720 K = 1, MM
720 B2(J,K) = B2(J,K) - (2.0*(DF(JJ)*D2(J,K)
1-D1(J)*D1(K)))/X(JJ)
CALL MATINV(B2,M,B1,1,DETERM)
DO 730 J=1,MM
IF (B2(J,J)) 2001,2001,2002
2001 B1(J) = -SQRT(-B2(J,J))
GO TO 730
2002 B1(J) = SQRT(B2(J,J))
730 CONTINUE
DO 740 J=1,MM
DO 740 K=1,MM
740 B2(J,K)=B2(J,K)/(B1(J)*B1(K))
WRITE(6,551)LE,SA
551 FORMAT(//,13H EXIT NUMBER=I3,20X,25H WEIGHTED SUM OF
1SQUARES=E15.8//)

RETURN
END

```

```

SUBROUTINE FUNC (LX)
C SUBROUTINE FUNC
DIMENSION DC(2183),B(20,2),D1(20),D2(20,20),FC(256),Z(256),
1E(6)
COMMON DC
EQUIVALENCE (Z,DC),(FC,DC(513)),(B,DC(1719)),(D1,DC(1759)),
1(D2,DC(1779)),(M,DC(1706)),(L,DC(2179)),(I,DC(2180)),
2(KG,DC(2182))
MM=M
DO 50 J=1,MM
D1(J)=0.0
DO 50 K=1,MM
50 D2(J,K)=0.0
FC(I)=B(M,L)*Z(I) + B(M-1,L)
KG1=KG
DO 60 J=1,KG1
60 FC(I)=FC(I) + B(3*J-2,L)/((Z(I)-B(3*J,L))**2 + B(3*J-1,L
1)**2)
IF(LX-1)110,110,120
120 D1(M-1)=1.0
D1(M)=Z(I)
DO 70 J=1,KG1
XI=(Z(I)-B(3*J,L))**2
ETA=B(3*J-1,L)**2
DEN=XI+ETA
D1(3*J-2)=1.0/DEN
D1(3*J-1)=-2.0*B(3*J-1,L)*B(3*J-2,L)/DEN**2
D1(3*J)=2.0*(Z(I)-B(3*J,L))*B(3*J-2,L)/DEN**2
D2(3*J-1,3*J-2)=-2.0*B(3*J-1,L)/DEN**2

```

```

D2 (3*J-2,3*J-1) = D2 (3*J-1,3*J-2)
D2 (3*J,3*J-2) = 2.0 * (Z(I) - B(3*J,L)) / DEN**2
D2 (3*J-2,3*J) = D2 (3*J,3*J-2)
D2 (3*J-1,3*J-1) = -2.0 * B(3*J-2,L) * (XI - 3.0 * ETA) / DEN**3
D2 (3*J-1,3*J) = -8.0 * B(3*J-2,L) * B(3*J-1,L) * (Z(I) - B(3*J,L))
1/DEN**3
D2 (3*J,3*J-1) = D2 (3*J-1,3*J)
70 D2 (3*J,3*J) = 2.0 * B(3*J-2,L) * (3.0 * XI - ETA) / DEN**3
110 CONTINUE
RETURN
END

```

```

SUBROUTINE EXAM(A,B,M,LF)
C SUBROUTINE EXAM
C   F O R T R A N 4
DIMENSION A(20,20),B(20),C(20)
DO 80 J=1,M
80 C(J)=A(J,J)
IF (A(1,1)) 60,200,70
60 A(1,1) = -SQRT(-A(1,1))
GO TO 300
70 A(1,1) = SQRT(A(1,1))
GO TO 100
100 IF (M-1) 400,400,110
110 DO 115 K=2,M
115 A(1,K) = A(1,K) / (A(1,1))
DO 120 J=2,M
J1=J-1
S=A(J,J)
DO 125 L=1,J1
125 S=S-A(L,J)**2
IF (S) 50,200,40
50 A(J,J) = -SQRT(-S)
GO TO 300
40 A(J,J) = SQRT(S)
GO TO 130
130 IF (J-M) 135,400,400
135 J2=J+1
DO 120 K=J2,M
S=A(J,K)
DO 145 L=1,J1
145 S=S-A(L,J)*A(L,K)
120 A(J,K) = S/A(J,J)
400 A(1) = B(1)/A(1,1)
IF (M-1) 420,420,405
405 DO 410 J=2,M
S=B(J)
J1=J-1
DO 415 L=1,J1
415 S=S-A(L,J)*B(L)
410 B(J) = S/A(J,J)
420 B(M) = B(M)/A(M,M)
J=M-1
435 IF (J) 450,450,425

```

```

425 S=B(J)
    J2=J+1
    DO 430 L=J2,M
430 S=S-A(J,L)*B(L)
    B(J)=S/A(J,J)
    J=J-1
    GO TO 435
450 LF=1
    GO TO 460
200 LF=0
    GO TO 460
300 LF=-1
460 DO 465 J=1,M
    A(J,J)=C(J)
    IF (J-M) 470,475,475
470 J2=J+1
    DO 465 K=J2,M
465 A(J,K)=A(K,J)
475 RETURN
    END

```

```

SUBROUTINE MATINV(A,N,B,M,DETERM)
C SUBROUTINE MATINV
C   F O R T R A N   4
C MATRIX INVERSION WITH ACCOMPANYING SOLUTION OF LINEAR
C EQUATIONS
DIMENSION IPIVOT(20),A(20,20),B(20,1),INDEX(20,2),PIVOT(20)
EQUIVALENCE (IROW,JROW),(ICOLUM,JCOLUM),(AMAX,T,SWAP)
DETERM=1.0
DO 20 J=1,N
20 IPIVOT(J)=0
DO 550 I=1,N
  AMAX=0.0
  DO 105 J=1,N
    IF (IPIVOT(J)-1) 60,105,60
60 DO 100 K=1,N
    IF (IPIVOT(K)-1) 80,100,740
80 IF (ABS(AMAX)-ABS(A(J,K))) 85,100,100
85 IROW=J
    ICOLUM=K
    AMAX=A(J,K)
100 CONTINUE
105 CONTINUE
    IPIVOT(ICOLUM)=IPIVOT(ICOLUM)+1
    IF (IROW-ICOLUM) 140,260,140
140 DETERM=-DETERM
    DO 200 L=1,N
      SWAP=A(IROW,L)
      A(IROW,L)=A(ICOLUM,L)
200 A(ICOLUM,L)=SWAP
      IF (M) 260,260,210
210 DO 250 L=1,M
      SWAP=B(IROW,L)
      B(IROW,L)=B(ICOLUM,L)

```

```

250 B(ICOLUM,L)=SWAP
260 INDEX(I,1)=IROW
    INDEX(I,2)=ICOLUM
    PIVOT(I)=A(ICOLUM,ICOLUM)
    DETERM=DETERM*PIVOT(I)
    A(ICOLUM,ICOLUM)=1.0
    DO 350 L=1,N
350 A(ICOLUM,L)=A(ICOLUM,L)/PIVOT(I)
    IF(M)380,380,360
360 DO 370 L=1,M
370 B(ICOLUM,L)=B(ICOLUM,L)/PIVOT(I)
380 DO 550 L1=1,N
    IF(L1-ICOLUM)400,550,400
400 T=A(L1,ICOLUM)
    A(L1,ICOLUM)=0.0
    DO 450 L=1,N
450 A(L1,L)=A(L1,L)-A(ICOLUM,L)*T
    IF(M)550,550,460
460 DO 500 L=1,M
500 B(L1,L)=B(L1,L)-B(ICOLUM,L)*T
550 CONTINUE
    DO 710 I=1,N
        L=N+1-I
        IF(INDEX(L,1)-INDEX(L,2))630,710,630
630 JROW=INDEX(L,1)
        JCOLUM=INDEX(L,2)
        DO 705 K=1,N
            SWAP=A(K,JROW)
            A(K,JROW)=A(K,JCOLUM)
            A(K,JCOLUM)=SWAP
705 CONTINUE
710 CONTINUE
740 RETURN
    END

```

```

SUBROUTINE PLOTB (NO,N,AA,BB)
C SUBROUTINE PLOT B
C A= LARGEST OF FC AND FM, B= SMALLEST
DIMENSION X(116),AA(512),BB(512),Y(4),ABC(2)
COMMON/DATA/ABC,Y
DATA(ABC=2HNO,3HYES),(Y=1H,1H*,1H.,1H
A=AA(1)
B=A
DO 900 I=1,N
IF(AA(I)-A)905,905,910
910 A=AA(I)
905 IF(BB(I)-A)915,915,920
920 A=BB(I)
915 IF(AA(I)-B)930,925,925
930 B=AA(I)
925 IF(BB(I)-B)935,900,900
935 B=BB(I)
900 CONTINUE
FACTOR = 1.0

```

```

520 IF (A-B-1000.0) 500, 510, 510
500 A = 2.0*A
      B = 2.0*B
      FACTOR = 2.0*FACTOR
      GO TO 520
510 KD = (A-B)/112.0 + 1.0
      KS = IFIX(B) - 2*KD
      WRITE (6,1)
      1  FORMAT(119H0...0.....1.....2.....3.....4
1.....5.....6.....7.....8.....9.....
210.....11....)
      DO 100 I=1,N
      DO 110 K=1,116
110 X(K)=Y(1)
      K = AA(I)*FACTOR
      K = (K-KS)/KD
      X(K) = Y(2)
      L = BB(I)*FACTOR
      L = (L-KS)/KD
      IF(L-K) 120,130,120
130 X(L)=Y(3)
      GO TO 105
120 X(L)=Y(4)
105 INO=I+NO-1
100 WRITE (6,90) INO,X
      90 FORMAT(1X13,116A1)
      WRITE (6,1)
      RETURN
      END
      SUBROUTINE JACOBI (N,Q,JVEC,M,V)
C      SUBPROGRAM FOR DIAGONALIZATION OF MATRIX Q BY SUCCESSIVE
C      ROTATIONS
      DIMENSION Q(20,20),V(20,20),X(20),IH(20)
C
C      NEXT 8 STATEMENTS FOR SETTING INITIAL VALUES OF MATRIX V
C
      IF(JVEC) 10,15,10
10 DO 14 I=1,N
      DO 14 J=1,N
      IF(I-J) 12,11,12
11 V(I,J)=1.0
      GO TO 14
12 V(I,J)=0.
14 CONTINUE
C
15 M=0
C      NEXT 8 STATEMENTS SCAN FOR LARGEST OFF DIAG. ELEM. IN EACH
C      ROW X(I) CONTAINS LARGEST ELEMENT IN ITH ROW
C      IH(I) HOLDS SECOND SUBSCRIPT DEFINING POSITION OF ELEMENT
C
      MI=N-1
      DO 30 I=1,MI
      X(I)=0.
      MJ=I+1

```

```

DO 30 J=MJ,N
IF (X(I)-ABS (Q(I,J))) 20,20,30
20 X(I)=ABS (Q(I,J))
IH(I)=J
30 CONTINUE
C
C NEXT 7 STATEMENTS FIND FOR MAXIMUM OF X(I)S FOR PIVOT
C ELEMENT
40 DO 70 I=1,MI
IF(I-1) 60,60,45
45 IF (XMAX-X(I)) 60,70,70
60 XMAX=X(I)
IP=I
JP=IH(I)
70 CONTINUE
C
C NEXT 2 STATEMENTS TEST FOR XMAX,IF LESS THAN 10**-8,GO TO
C 1000
C
EPSI=1.E-8
IF (XMAX-EPSI) 1000,1000,148
C
148 M=M+1
C
C NEXT 11 STATEMENTS FOR COMPUTING TANG,SINE,COSN,Q(I,I),
C Q(J,J)
C
IF (Q(IP,IP)-Q(JP,JP)) 150,151,151
150 TANG =-2.*Q(IP,JP)/(ABS(Q(IP,IP))+SQRT((Q(IP,IP)-Q(JP,JP)
1-Q(JP,JP))**2+4.*Q(IP,JP)**2))
GO TO 160
151 TANG =+2.*Q(IP,JP)/(ABS(Q(IP,IP))+SQRT((Q(IP,IP)-Q(JP,JP)
1-Q(JP,JP))**2+4.*Q(IP,JP)**2))
160 COSN=1.0/SQRT(1.0+TANG**2)
SINE=TANG*COSN
QII= Q(IP,IP)
Q(IP,IP)= COSN**2*(QII+TANG*(2.*Q(IP,JP)+TANG*Q(JP,JP)))
Q(JP,JP)= COSN**2*(Q(JP,JP)-TANG*(2.*Q(IP,JP)-TANG*QII))
C
Q(IP,JP)=0.
C
C NEXT 4 STATEMENTS FOR PSEUDO RANK OF THE ELGENVALUES
IF (Q(IP,IP)-Q(JP,JP)) 152,153,153
152 TEMP=Q(IP,IP)
Q(IP,IP)=Q(JP,JP)
Q(JP,JP)=TEMP
C
C NEXT 6 STATEMENTS ADJUST SIN,COS FOR COMPUTATION OF
C Q(I,K),V(I,K)
C
IF(SINE) 154,155,155
154 TEMP=+COSN
GO TO 170
155 TEMP=-COSN

```

```

170 COSN=ABS(SINE)
    SINE=TEMP
C
C   NEXT 10 STATEMENTS FOR INSPECTING THE I'S BETWEEN I+1 AND
C   N-1 TO DETERMINE WHETHER A NEW MAXIMUM VALUE SHOULD BE
C   COMPUTED SINCE THE PRESENT MAXIMUM IS IN THE I OR J ROW
C
153 DO 350 I=1,MI
    IF (I-IP) 210,350,200
200 IF (I-JP) 210,350,210
210 IF (IH(I)-IP) 230,240,230
230 IF (IH(I)-JP) 350,240,350
240 K= IH(I)
    TEMP=Q(I,K)
    Q(I,K)=0.
    MJ=I+1
    X(I)=0.
C
C   NEXT 5 STATEMENTS SEARCH IN DEPLETED ROW FOR NEW MAXIMUM
C
    DO 320 J=MJ,N
    IF (X(I)-ABS(Q(I,J))) 300,300,320
300 X(I)=ABS(Q(I,J))
    IH(I)=J
320 CONTINUE
    Q(I,K)=TEMP
350 CONTINUE
C
    X(IP)=0.
    X(JP)=0.
C
C   NEXT 30 STATEMENTS FOR CHANGING THE OTHER ELEMENTS OF Q
C
    DO 530 I=1,N
C
    IF (I-IP) 370,530,420
370 TEMP=Q(I,IP)
    Q(I,IP)=COSN*TEMP+SINE*Q(I,JP)
    IF (X(I)-ABS(Q(I,IP))) 380,390,390
380 X(I)=ABS(Q(I,IP))
    IH(I)=IP
390 Q(I,JP)=-SINE*TEMP+COSN*Q(I,JP)
    IF (X(I)-ABS(Q(I,JP))) 400,530,530
400 X(I)=ABS(Q(I,JP))
    IH(I)=JP
    GO TO 530
C
420 IF (I-JP) 430,530,480
430 TEMP =Q(IP,I)
    Q(IP,I)=COSN*TEMP+SINE*Q(I,JP)
    IF (X(IP)-ABS(Q(IP,I))) 440,450,450
440 X(IP)=ABS(Q(IP,I))
    IH(IP)=I
450 Q(I,JP)=-SINE*TEMP+COSN*Q(I,JP)

```



```

      IF (X(I)-ABS(Q(I,JP))) 400,530,530
C
480 TEMP=Q(IP,I)
   Q(IP,I)=COSN*TEMP+SINE*Q(JP,I)
   IF(X(IP)-ABS(Q(IP,I))) 490,500,500
490 X(IP)=ABS(Q(IP,I))
   IH(IP)=I
,500 Q(JP,I)=-SINE*TEMP+COSN*Q(JP,I)
   IF(X(JP)-ABS(Q(JP,I))) 510,530,530
510 X(JP)=ABS(Q(JP,I))
   IH(JP)=I
530 CONTINUE
C
C
C
      NEXT 6 STATEMENTS TEST FOR COMPUTATION OF EIGENVECTORS
      IF (JVEC) 540,40,540
540 DO 550 I=1,N
      TEMP=V(I,IP)
      V(I,IP)=COSN*TEMP+SINE*V(I,JP)
550 V(I,JP)=-SINE*TEMP+COSN*V(I,JP)
      GO TO 40
1000 RETURN
      END

```

APPENDIX B

PROGRAM MCAREAD

8E	E030	LDX \$E030	PIA BASE ADDRESS=PIAAD
6F	01	CLR 1,X	ACCESS DDRA
6F	03	CLR 3,X	ACCESS DDRB
10			
8E	F004	LDY \$F004	DDRA,B HAVE UPPER NYBBLE=OUTPUT, LOWERT NYBBLE=INPUT, THEN ACCESS PIAD'S
10			
AF	81	STY ,X++	FO INTO DDRA ,04 INTO CRA
10			
AF	81	STY ,X++	FO INTO DDRB, 04 INTO CRB
A6	83	LDA ,--X.	READ PIABD TO CLEAR INTERRUPTS
A6	83	LDA ,--X	LIKEWISE FOR PIAAD, 'X NOW=\$E030
10			
8E	C400	LDY BEGA	
86	70	LDA \$70	=READY2+SHFT+SP=HI
A7	02	STA 2,X	PIABD
C6	06	LDB 6	B= DIGITS/CHANNEL
34	READ		FIRST READ FOLLOWS REDY2
04		PSHS B	SAVE DIGIT COUNTER
C6	10	LDB \$10	
12		NOP	
5A	DELAY	DECB	WAIT FOR MCA TO PRESENT DATA
26	FD	BNE	DELAY
35		PULS B	RETIEVE DIGIT COUNTER
04			
A6	84	LDA ,X	INPUT DATA VIA PIAAD
84	0F	ANDA \$0F	ONLY LOWER NIBBLE SIGNIFICANT
8A	30	ORA \$30	CONVERT TO ASCII
A7	A0	STA ,Y+	STORE DIGIT Y AND INCREMENT Y BY 1
10			
8C	DC01	CMFY ENDA+2	ENDA=BEGA+6*1024=BEGA+\$1800
27	11	BEQ STOP	(NB READ PAST ENDA TO GENERATE LCHO WHICH RESETS MCA FOR "DISPLAY")
5A		DECB REDY 2	
27	DF	BEQ	CALL OUT NEXT CHANNEL AFTER 6 DIGITS
86	40	LDA \$40	=SP
A7	02	STA 2,X	2,X=PIABD. SHFT LO ,SP HI
6F	02	CLR 2,X	SP LO
A7	02	STA 2,X	SHFT LO ,SP HI
86	60	LDA \$60	=SHFT+SP
A7	02	STA 2,X	SHFT,SP HI
20	D7	BRA READ	READ FOLLOWS NEXT 5 SHIFTS
3F	STOP	SWI	

PROGRAM 6809 READ

This program allows the SWTP 6809 general purpose computer to act as terminal for a host computer. Once terminal mode established, typing control Q will upload the contents of a block of memory located at \$C400 to \$D001 of the SwTP. Upon completion of data transfer, control returns to the terminal emulation program.

```

0000                                ORG    $0000
E004  CONSOLE EQU    $E004
E024  MODEM   EQU    $E024
C400  BEGADR EQU    $C400  BEG#N ADDR. OF DATA TRANSFER
D001  ENDADR  EQU    $D001  END ADDR. OF DATA TRANSFER
000D  CR      EQU    $0D    CARRIAGE RETURN
000A  LF      EQU    $0A    LINE FEED
0020  SP      EQU    $20    SPACE
    
```

```

BE  E024  INIT2B  LDY    MODEM  GET MODEM STATUS
86  03    .        LDA    #03    MASTER RESET ACIA
A7  84    .        STA    0,X
86  11    .        LDA    #%00010001 ACIA OPERATING MODE
    *                                     8BITS, 2STOPS,OPARITY
84    .        STA    0,X
    * KEYBOARD IS SCANNED FOR CHARACTERS
    *
F6  E004  CONFIN  LDB    CONSOLE GET CONSOLE STATUS
57    .        ASRB   ANY CONSOLE INPUT
24  13    .        BCC   MODIN   IF NOT, ANY MODEM INPUT
B6  E005  .        LDA    CONSOLE+1 IF YES, READ DATA
84  7F    .        ANDA  #$7F    STRIP PARITY BIT
81  11    .        CMPA  #$11    IS IT TRANSFER COMMAND Q'
27  1F    .        BEQ   MDOUT2  IF YES, GO TO TFR RTN.
    *
    * DATA IS SENT THROUGH PORT 2B TO MAIN
    *
F6  E024  MODOUT  LDB    MODEM   OTHERWISE, GET MODEM STATUS
57    .        ASRB   .
57    .        ASRB   ANY OUTPUT TO SEND
24  EA    .        BCC   CONFIN  IF NOT CHECK CONSOLE
B7  E025  .        STA    MODEM+1 OTHERWISE, SEND DATA
    *
    *MODEM IS MONITORED FOR INCOMING CHARACTERS.
    *
F6  E024  MODIN  LDB    MODEM
57    .        ASRB   .
24  E1    .        BCC   CONFIN
B7  E025  .        STA    MODEM+1
    *
    *OUTPUT TO SCREEN IS MONITORED HERE
    *
    
```

F6	E004	CONOUT	LDB	CONSOLE	GET CONSOLE STATUS
57			ASRB		
57			ASRB		ANY OUTPUT TO SCREEN
24	F9		BCC	CONOUT	WAIT FOR SOME
B7	E005		STA	COSOLE+1	THEN SEND TO SCREEN
20	C7		BRA	INIT2B	RESUME MONITORING

*
 * ROUTINE TO SEND MULTICHANNEL ANALYZER DATA LOCATED AT
 * \$C400-\$D001 of SWTP TO HOST COMPUTER FOR PROCESSING.
 *

C6	0A	LINE	LDB	#\$oA
36	04	WORD	PSHU	B
86	06		LDA	#06
36	02	DIGIT	PSHU	A
A6	80		LDA	,X+
8C	D001		CMPX	#ENDADR
27	20		BEQ	INITB
8D	20		BSR	SEND
37	02		PULU	A
4A			DECA	
26	F0		BNE	DIGIT
86	20		LDA	#SP
8D	17		BSR	SEND
37	04		PuLU	B
5A			DECB	
26	E3		BNE	WORD
36	04		PSHU	B
86	0D		LDA	#CR
8D	0C		BSR	SEND
86	0A		LDA	#LF
8D	08		BSR	SEND
8D	11		BSR	DELAY
20	D3		BRA	LINE
37	06		PULU	A,B
20	88		BRA	INIT2B
F6	E024		LDB	MODEM
57			ASRB	
57			ASRB	
24	F9		BCC	SEND
B7	E025		STA	MODEM+1
39			RTS	
108E	4000	DELAY	LDY	#\$4000
31	3F		LEAY	-1,Y
108C	0000		CMPY	#0000
26	F4		BNE	DELAY
39			RTS	
			END	INIT2B

Transferring of the data can be done through following commands :

MCA TO SWTP 6809

READ - IN/out switch on MCA must be on PRINTER position

Type: Control P C100

Turn the mode on MCA (master controle) to READ -IN/OUT position, then

Type: G

SWTP 6809 to CYBER

Connect the SWTP to the MODEM, then

Type: Control P C000 G

Teletype is now acting as a terminal of CYBER

Turn on the MODEM and press CR.

Open a new file in your computer account and then

Type: TEXT, wait for the respond

Type: Control Q

Transfer of data is now in process

Wait about 7 minutes, then press CR and

Type: Control C and wait for the respond, and then

Save the file.

APPENDIX C

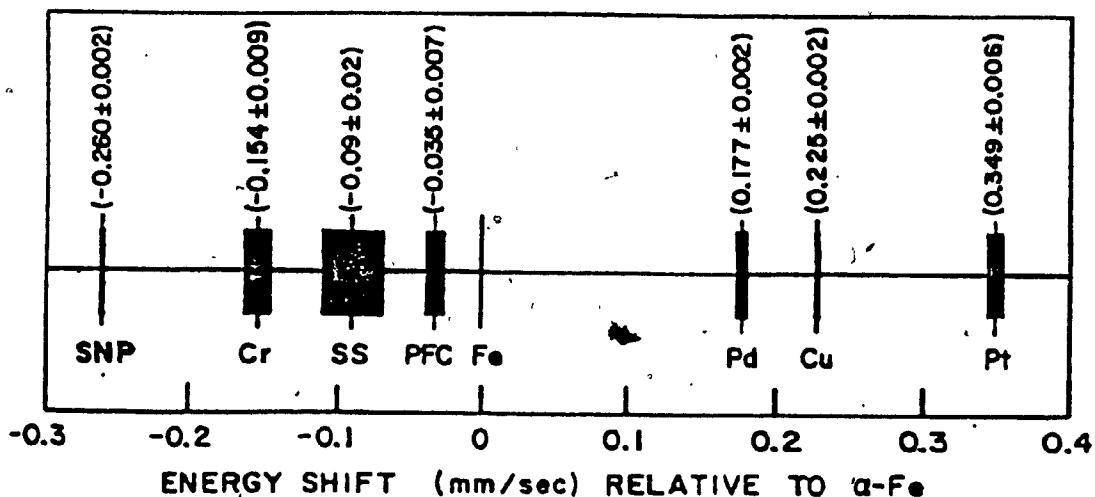
DESCRIPTION OF THE SAMPLES

TABLE	TEXTURE	FORM	SIZE	CONSTITUENT
A (S24-793)	GRANOBLASTIC	EQUIGRANULAR	FINE	GARNET/PYROXENE-OPAQUES-PYRITE
B (S24-558)	PORPHYROBLASTIC	XENOBLASTIC	1-3mm	GARNET/PYROXENE-OPAQUES-CHALCOPYRITE
C (S42-520)	PORPHYROBLASTIC	XENOBLASTIC	1-5mm	GARNET/PYROXENE-OPAQUES
D (S42-534)	PORPHYROBLASTIC	IDIOBLASTIC	1-10mm	GARNET/PYROXENE-CALCITE
E (P31-455)	GRANOBLASTIC	APLITIC	VERY FINE	GARNET/PYROXENE-CALCITE-PYRITE
F (P72-254)	PORPHYROBLASTIC	XENOBLASTIC	-2mm	GARNET/PYROXENE-OPAQUES
G (S38-251)	GRANOBLASTIC	SUBHEDRAL	FINE	GARNET/PYROXENE-CALCITE-MAGNETITE
H (SH-14)	GRANOBLASTIC	EQUIGRANULAR	VERY FINE	GARNET/PYROXENE-PYRITE
I (S104-200)	GRANOBLASTIC	EQUIGRANULAR	VERY FINE	GARNET/PYROXENE-PYRITE-MAGNETITE
J (T-16)	GRANOBLASTIC	EQUIGRANULAR	FINE	GARNET/PYROXENE-OPAQUES-MAGNETITE
K (T-24)	GRANOBLASTIC	EQUIGRANULAR	FINE	GARNET/PYROXENE-CALCITE-MAGNETITE
L (T-45)	PORPHYROBLASTIC	XENOBLASTIC	1-3mm	GARNET/PYROXENE-MAGNETITE
M (T-50)	PORPHYROBLASTIC	XENOBLASTIC	1-3mm	GARNET/PYROXENE-OPAQUES-MAGNETITE
N (T-62)	GRANOBLASTIC	APLITIC	FINE	GARNET/PYROXENE-OPAQUES-MAGNETITE

APPENDIX D

Isomer-Shift Scale for Fe⁵⁷ (14.4 Kev)

Sources and Reference Substances



Notes: Sources and absorbers at room temperature

SNP - sodium nitroprusside ($\text{Na}_2\text{Fe}(\text{CN})_5\text{NO} \cdot 2\text{H}_2\text{O}$)

SS - stainless steel

PFC - potassium ferrocyanide ($\text{K}_4\text{Fe}(\text{CN})_6 \cdot 3\text{H}_2\text{O}$)

α -Fe is the normal form of metallic iron at room temperature.

1mm/sec = 11.62478 ± 0.00004 MHz

The following example illustrates the use of this figure.

According to the figure, the excitation energy from the ground state than the first excited state of Fe⁵⁷ is less when the Fe⁵⁷ is in stainless steel than when it is in copper. In velocity units this energy difference is $0.225 + 0.09 = 0.315$ mm/sec. Thus the isomer shift of Fe⁵⁷ in stainless steel relative to Fe⁵⁷ in copper is -0.315 mm/sec, or, conversely, the isomer shift of Fe⁵⁷ in copper relative to Fe⁵⁷ in stainless steel is $+0.315$ mm/sec.